MOLECULAR BEAM EPITAXY SYNTHESIS AND INVESTIGATION OF IRON-BASED QUANTUM MATERIALS

A DISSERTATION SUBMITTED TO

THE DEPARTMENT OF PHYSICS

IN PARTIAL FULFILLMENT OF THE REQUIREMENTS

FOR THE DEGREE OF

DOCTOR OF PHILOSIPHY

IN PHYSICS

BY

ZHENG REN

BOSTON COLLEGE

MORRISSEY COLLEGE OF ARTS AND SCIENCES

GRADUATE SCHOOL

CHESTNUT HILL, MASSACHUSETTS

MAY, 2022

Molecular Beam Epitaxy Synthesis and Investigation of Iron-based Quantum Materials

Zheng Ren

Thesis Advisor: Ilija Zeljkovic

The splendid world of quantum materials is being unveiled in modern condensed matter physics, thanks to the advanced material synthesis methods, refined experimental probing techniques and deeper theoretical understanding. Unconventional superconductivity and topological phenomena are two of the main themes in this realm. Many outstanding problems are waiting to be solved and there is also a great potential in future technological applications. Among many routes of studying the quantum materials, creating thin film structures provides a special opportunity to learn the physical properties in low dimensions, to explore the effect of substrate and strain and to make novel electronic devices.

In this thesis, I will present successful molecular beam epitaxy thin film synthesis of: (1) unconventional superconductor FeSe, (2) topological insulator Bi_2Se_3 doped with magnetic Fe atoms and (3) kagome structure magnets FeSn and Fe_3Sn_2. For (1), I will describe the finding of a dislocation network, its impact on the spatially-modulated strain field and its interesting interplay with the spontaneous symmetry-broken nematic phase. This is a new finding in the FeSe/$SrTiO_3$ heterostructure and also provides fresh insights in the understandings of nematicity. For (2), I will show how we cross-check the doping ratio using different characterization techniques. Our observation indicates the possible formation of Fe clusters or impurity phases and sets the foundation for future synthesis of similar structures. For (3), I will demonstrate the novel selective synthesis of Fe_xSn_y thin films. A plethora of spectral features were found in Fe_3Sn_2, implying a link with the Weyl physics. The Fe_xSn_y thin films can potentially be a platform for the exploration of correlated, topological quantum phases in low dimensions.

Table of Contents

List of Figures

List of Tables

Acknowledgments

First and foremost, I would like to express my gratitude to my PhD advisor Prof. Ilija Zeljkovic for his full support and guidance throughout the past six-ish years. As one of the first batch of his students, I was lucky enough to grow together with the lab and to enjoy his tremendous help in every aspect of my research. I am grateful that he pointed out some of the most interesting topics in condensed matter physics and gave me the experimental resources to study them. There were times when the instrument did not perform properly, some of which inevitable and some others due to my silly mistakes, but he was always patient and optimistic, and forgiving, for which I am really thankful to him. When exciting new phenomena showed up, he was always able to provide extremely helpful advices with his wisdom and experience, from which I learned a lot. He also worked so hard, and I am really grateful when I received his timely replies to my emails at late nights and on Weekends so that things went on efficiently. I wish I can be like him if one day I am able to be a PI.

I am also grateful for having the best colleagues and labmates: Bryan Rachmilowitz, Hong Li, He Zhao, Shang Gao, Alex LaFleur, Shrinkhala Sharma, Wilber Alfaro Castro, Siyu Cheng, Muxian Xu. I really enjoyed the time we spent together in Zeljkovic Lab and our collaborations on research. I would also like to say thank you to my important research collaborators: Prof. Ziqiang Wang, Dr. Shiang Fang, Prof. Madhav Ghimire, Faranak Bahrami, Prof. Fazel Tafti and more.

I am also thankful for going to some of the best graduate physics courses. Prof. Ying Ran's Solid State Physics II and Statistical Physics I are my favorites, although they are challenging. I actually still look at his SS2 lecture notes every now and then since they are too insightful. Prof. Fazel Tafti's From Bonds to Bands and Magnetic Materials are really useful courses for an experimental condensed matter physicist.

I want to thank every one in the Boston College Physics Department. I am lucky enough to have made friends with many grad students here. Thank you the department people

Nancy, Jane, Scott and more. Thank you Chair Prof. Michael Graf for forgiving me for breaking the quartz rod and holder of the MPMS a few times.

I would also like to thank my thesis committee: Prof. Ziqiang Wang, Prof. Fazel Tafti and Prof. Qiong Ma.

Last but not the least, I would like to deeply thank my parents for their unconditional love and support. I cannot thank them enough. I also want to thank my girlfriend Xinyue for everything.

Chapter 1

An overview of quantum materials

"Quantum materials" is a term frequently seen in the context of condensed matter physics nowadays, and this chapter serves as a very brief overview of such subject and an introduction of this thesis. However, a proper definition of quantum materials should be given first. Fortunately, there are two relevant Wikipedia pages "Quantum Materials" [1] and "Macroscopic Quantum Phenomena" [2] that do this job very well. Briefly speaking, quantum materials refer to those physical properties of a material that do not exist in a classical world, such as the superconductivity or the topological phenomena. This is in contrast to some other properties that can be modeled, sometimes incredibly well, using a semiclassical approach. One example is using the Drude model to calculate the resistivity of a ordinary metal [3] assuming the electron are ballistic and can move freely within a mean free time before colliding with the immobile ions. Although a full description of the resistivity would need a quantum mechanical solid state band theory, the drude model provides a good explanation. However, this is not the case for superconductivity - ballistic electrons are never going to yield zero resistivity in a matrix of ions, but only a wave-like description can explain the zero resistivity. Superconductivity is really one of the best examples of the tremendous success in the discoveries of quantum materials/phenomena and the exciting ongoing research along this route. In the late 20th century, discovery of the quantum Hall state greatly enriched the family of quantum materials. It is the cornerstone of all the topological materials that are being intensely studied today.

In this chapter, I will give a short introduction to superconductivity first, including the conventional superconductivity and the unconventional copper and iron-based superconductors. Then I will briefly introduce the topological phenomena. These two broad subjects are related to chapter 3 and chapter 4/5, respectively.

1.1 Superconductivity

Condensed matter physics has the largest number of publications in the broad field of physics [4]. Among all the subjects of condensed matter physics, superconductivity might be one of the most popular. Superconductivity was discovered by Heike Kamerlingh Onnes in 1911 when he cooled solid mercury down to liquid helium temperature at 4.2 K and observed a vanished resistance. Since then, important events in the history of supercoductivity are listed in Table 1.1.

Year	Event
1911	discovery of superconductivity
1933	discovery of Meissner effect
1935	London equation
1950	Ginzburg-Landau theory
1957	BCS theory
1962	Josephson effect
1986	discovery of cuprates
2008	discovery of Fe-based superconductors

Table 1.1: History of superconductivity.

Superconductivity can be classified as the conventional superconductivity and the unconventional superconductivity based on whether it can be explained by the BCS theory or not. In general, the conventional superconductors have lower critical temperature (T_c) [5], while T_c of the unconventional ones such as the cuprates can reach as high as 130 K [6]. A more elaborated introduction is given as follows.

1.1.1 Conventional superconductivity

The conventional superconductivity is explained by the Bardeen-Cooper-Schrieffer (BCS) theory in their ground-breaking paper in 1957 [7, 8]. The theory was established after two key experimental findings on superconductivity since Onnes' discovery, i.e. the energy spectrum of a superconductor is gapped suggested by the specific heat experiment and the isotope effect meaning that superconductivity has something to do with the phonon.

Cooper [9] proposed that with an attractive interaction between a pair of electrons $\langle \mathbf{k}|H_1|\mathbf{k}'\rangle = -|F|$ within a energy shell near the Fermi surface ($\epsilon_{\mathbf{k}}, \epsilon'_{\mathbf{k}} < \hbar\omega_D$), which is due to electron-phonon coupling justified by Bardeen and Pines [10] and Fröhlich [11], the pair of electrons can form a bound state that has a lower energy than $2\epsilon_F$. The bound state exists no matter how small the attractive potential is, therefore this is an instability of the Fermi surface.

The many-body theory of conventional superconductivity was established by BCS [7, 8] using a mean-field approach. Consider such an interacting Hamiltonian

$$H = \sum_{\mathbf{k}\sigma} (\epsilon_{\mathbf{k}} - \mu) c^\dagger_{\mathbf{k}\sigma} c_{\mathbf{k}\sigma} + \frac{1}{N} \sum_{\mathbf{k}\mathbf{k}'} V_{\mathbf{k}\mathbf{k}'} c^\dagger_{\mathbf{k}\uparrow} c^\dagger_{-\mathbf{k}\downarrow} c_{-\mathbf{k}'\downarrow} c_{\mathbf{k}'\uparrow} \tag{1.1}$$

We can perform a mean-field approximation and the resulting Hamiltonian reads

$$H = \sum_{\mathbf{k}\sigma} (\epsilon_{\mathbf{k}} - \mu) c^\dagger_{\mathbf{k}\sigma} c_{\mathbf{k}\sigma} - \sum_{\mathbf{k}} (\Delta_{\mathbf{k}} c^\dagger_{\mathbf{k}\uparrow} c^\dagger_{-\mathbf{k}\downarrow} + \Delta^*_{\mathbf{k}} c_{-\mathbf{k}\downarrow} c_{\mathbf{k}\uparrow}) \tag{1.2}$$

where $\Delta_{\mathbf{k}}$ is the gap function

$$\Delta_{\mathbf{k}} = -\frac{1}{N} \sum_{\mathbf{k}'} V_{\mathbf{k}\mathbf{k}'} \langle c_{-\mathbf{k}'\downarrow} c_{\mathbf{k}'\uparrow} \rangle \tag{1.3}$$

By doing the Bogoliubov transformation

$$\begin{pmatrix} c_{\mathbf{k}\uparrow} \\ c^{\dagger}_{-\mathbf{k}\downarrow} \end{pmatrix} = \begin{pmatrix} u^*_{\mathbf{k}} & v_{\mathbf{k}} \\ -v^*_{\mathbf{k}} & u_{\mathbf{k}} \end{pmatrix} \begin{pmatrix} \gamma_{\mathbf{k}\uparrow} \\ \gamma^{\dagger}_{-\mathbf{k}\downarrow} \end{pmatrix} \tag{1.4}$$

the Hamiltonian is diagonalized as

$$H = \sum_{\mathbf{k}\sigma} E_{\mathbf{k}} \gamma^{\dagger}_{\mathbf{k}\sigma} \gamma_{\mathbf{k}\sigma} + E_0 \tag{1.5}$$

where the energy spectrum is $E_{\mathbf{k}} = \sqrt{(\epsilon_{\mathbf{k}} - \mu)^2 + |\Delta_{\mathbf{k}}|^2}$, so it is gapped. In STM dI/dV spectrum, this would result in a gap at Fermi level of $2|\Delta_{\mathbf{k}}|$.

The Bogoliubov quasiparticle $\gamma_{\mathbf{k}}$ is a mixture of electron and hole. The parameters $u_{\mathbf{k}}$ and $v_{\mathbf{k}}$ are

$$|u_{\mathbf{k}}|^2, |v_{\mathbf{k}}|^2 = \frac{1}{2}(1 \pm \frac{\epsilon_{\mathbf{k}} - \mu}{\sqrt{(\epsilon_{\mathbf{k}} - \mu)^2 + |\Delta_{\mathbf{k}}|^2}}) \tag{1.6}$$

Therefore in the superconducting state with a finite $|\Delta_{\mathbf{k}}|$, near the Fermi level $\epsilon_{\mathbf{k}} - \mu \sim 0$, we have $|u_{\mathbf{k}}|^2 = |v_{\mathbf{k}}|^2 = 1/2$. This indicates a particle-hole symmetry, which is reflected in the superconducting gap that is symmetric with respect to Fermi level in the STM dI/dV spectra.

The ground state of the BCS mean-field Hamiltonian is the vacuum of the Bogoliubov quasiparticles, and it can also be written in this form:

$$|\Psi_{BCS}\rangle = \prod_{\mathbf{k}} (u_{\mathbf{k}} + v_{\mathbf{k}} c^{\dagger}_{\mathbf{k}\uparrow} c^{\dagger}_{-\mathbf{k}\downarrow})|0\rangle \tag{1.7}$$

where $|0\rangle$ is the vacuum of the electrons, therefore the BCS ground state is an ensemble of cooper pairs.

An important result of the BCS theory is the gap equation which is a result of the

self-consistency of the mean-field Hamiltonian. This famous equation is

$$\frac{\Delta_0}{k_B T_c} \approx 1.76 \tag{1.8}$$

which relates the superconducting critical temperature and the gap size. This is consistent with the experimental results of many conventional superconductors. Other successes of BCS include its prediction of the specific heat jump ΔC at the superconducting transition temperature and its consistency with experiments, and also that it captures the Meissner effect namely the perfect diamagnetism of superconductors.

1.1.2 Unconventional superconductors

The BCS theory is a remarkable milestone in the history of superconductivity, but it would be a shame if this is the end of the story. Fortunately, many other types of superconductors, in the class of unconventional superconductivity, have been discovered (Fig. 1.1.1). Remarkably, the pairing mechanism of the unconventional superconductivity still remains an outstanding problem.

The members of the unconventional superconductors include the copper-based superconductors (cuprates) [12, 13], heavy fermion superconductors [14], iron-based superconductors [15], nickel-based superconductors [16], possible spin-triplet Ruthenates [17] and the magic-angle twisted bilayer graphene [18, 19]. Most relevant to this thesis, an overview on the cuprates [20, 21] and Fe-based superconductors [22, 23] is given below.

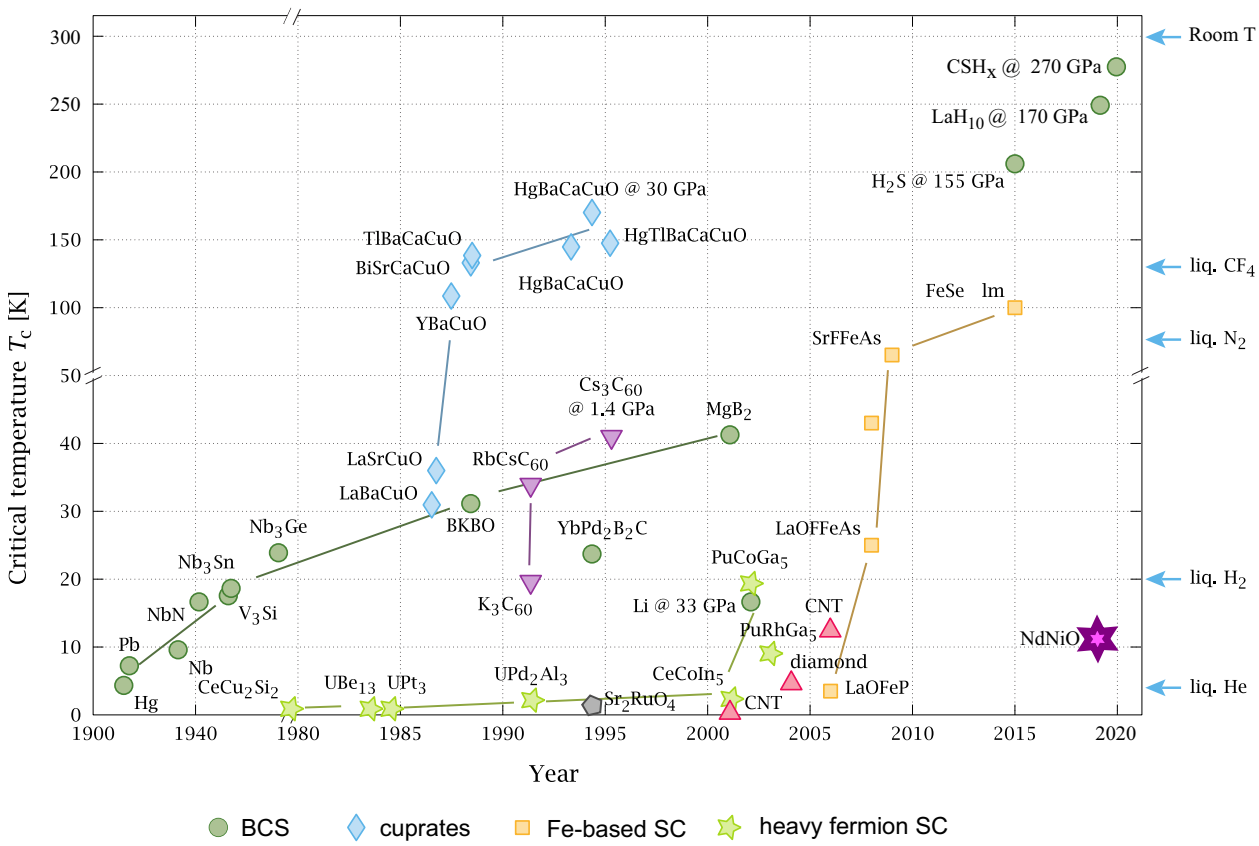

Figure 1.1.1: Timeline of the discoveries of superconductors, adapted from Ref. [24] and [25] under CC-BY-SA-4.0.

The cuprates include a class of materials that all have the characteristic CuO_2 planes that superconduct upon receiving carrier doping from the spacer layers that are different from one compound to another. Taking the $Bi_2Sr_2CaCu_2O_{8+x}$ (Bi-2212) compound as an example [20], it has the crystal structure shown in Fig. 1.1.2(a). Bi-2212 has 2 CuO_2 planes in a unit cell, while there are other type of cuprates that has 1, 2, 3 or even more CuO_2 planes in a unit cell.

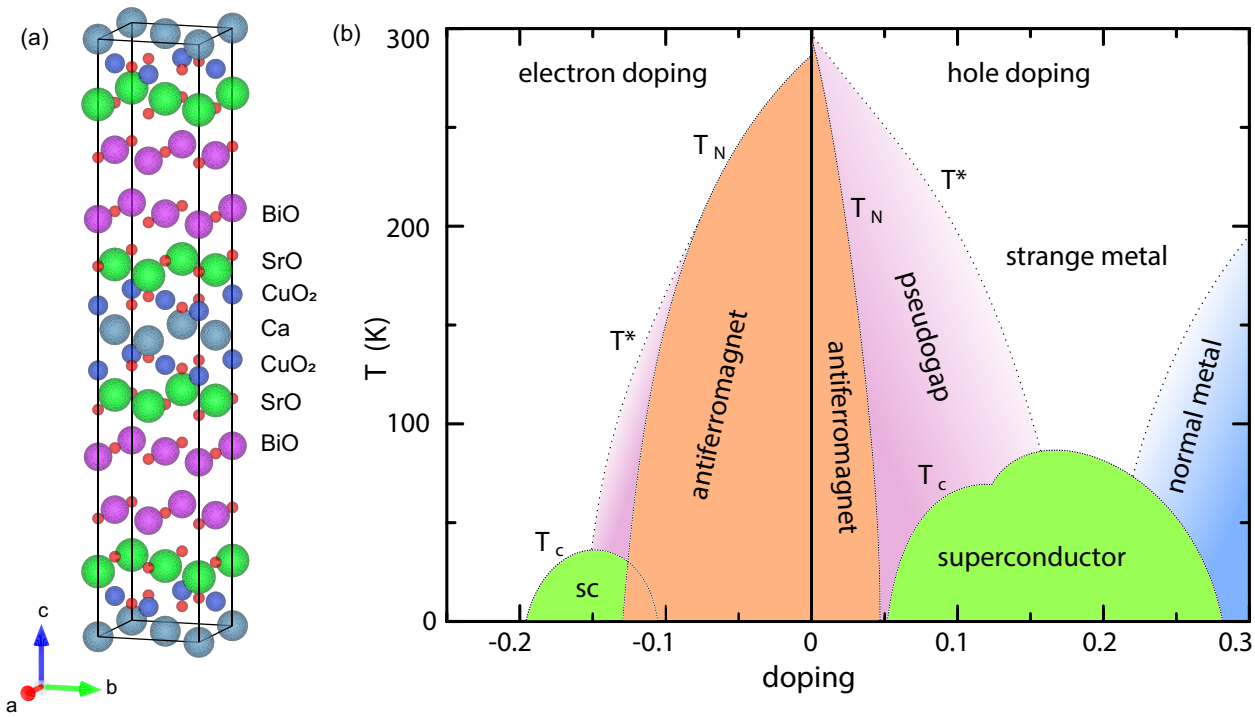

Figure 1.1.2: (a) Crystal structure of Bi-2212. (b) Generic phase diagram of cuprates, adapted from Ref. [26] under CC-BY-SA-3.0.

Unlike the conventional superconductors, cuprates superconduct when off-stoichiometric doping a parent compound. The parent compound is an antiferromagnetic Mott insulator [12]. Upon electron or hole doping, the Mott phase is suppressed and superconductivity emerges. There is a pseudogap phase above the superconducting dome in the underdoped regime, whose origin is still uncovered. The normal state right above the superconducting phase of cuprates is also not a Fermi liquid, but a "strange metal", exhibiting a linear ρ-T relationship. Fig. 1.1.2(b) displays a generic phase diagram of cuprates.

A close cousin of the cuprates is the family of Fe-based superconductors, which are further divided into the iron pnictides and iron chalcogenides. A lot of similarities are shared between cuprates and Fe-based superconductors. The supercoducting constituent in the pnictides are the As-Fe-As trilayer structure, which is sandwiched in spacer layers that varies between different types of pnictides. The different spacer layer structure determines

which family of “1111”, “122”, “111”, and more, that the pnictide compound belongs to. Fig. 1.1.3(a) illustrates the “122” parent compound $BaFe_2As_2$, where doping all three sites - Ba, Fe or As - can lead to superconductivity.

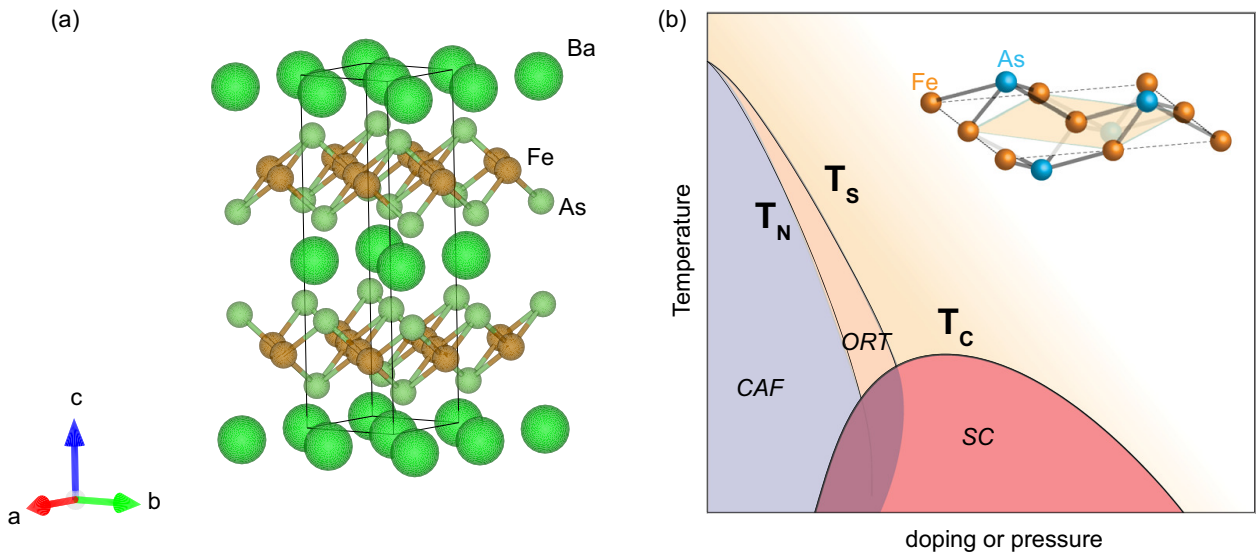

Figure 1.1.3: (a) Crystal structure of $BaFe_2As_2$. (b) A typical phase diagram of Fe pnictides, adapted from Ref. [27] under CC-BY-4.0.

The phase diagram of pnictides (Fig. 1.1.3(b)) also looks very much similar to that of the cuprates, where there is a parent phase that is not superconducting without carrier doping, and a superconducting dome emerges upon doping or applying pressure which essentially changes the lattice constant. However, important distinctions between the pnictides and the cuprates are worth noting. The biggest difference is probably on the parent phase of the pnictides, which is metallic with antiferromagnetic ordering. This is in contrast to the “doping a Mott insulator” picture that works for cuprates. Orbital-dependent Mottness has been proposed in the underdoped regime for pnictides. Since the electron configuration of Fe^{3+} is $3d^5$ in contrast to $3d^9$ for Cu^{2+}, all five d-orbitals are active in Fe-base superconductors while there is only one half-filled d-orbital near Fermi level in cuprates. The electron correlation in pnictides are also much weaker than cuprates as demonstrated in the bandwidth

renormalization factor by ARPES [27].

Another important ingredient in Fe-based superconductors is the nematicity, defined as the in-plane spontaneous rotational symmetry breaking, both structurally and electronically. It is a vertile phase in all Fe-based superconductors and has a intimate relationship with the magnetic ordering and superconductivity. In pnictides, the nematic phase appears upon cooling and is soon followed by the antiferromagntic phase (Fig. 1.1.3(b)), therefore it has been argued to be spin driven [28–30]. A nematic quantum criticality has also been proposed to enhance superconductivity [31–34].

Iron chalcogenide is another species in Fe-based superconductors and structurally simpler than the pnictides (Fig. 1.1.4) [35–37]. The chalcogenides denote the compounds centering around FeSe, including $FeTe_{1-x}Se_x$, $FeSe_{1-x}S_x$, intercalated FeSe, $FeTe_{1-x}Se_x$ thin films deposited on $SrTiO_3$. In contrast to pnictides, FeSe superconducts without doping. The key differences of chalcogenides from pnictides include the nematic phase in absence of a magnetic order in FeSe. This drives the theoretical efforts searching for the origin of nematicity other than spin [38, 39].

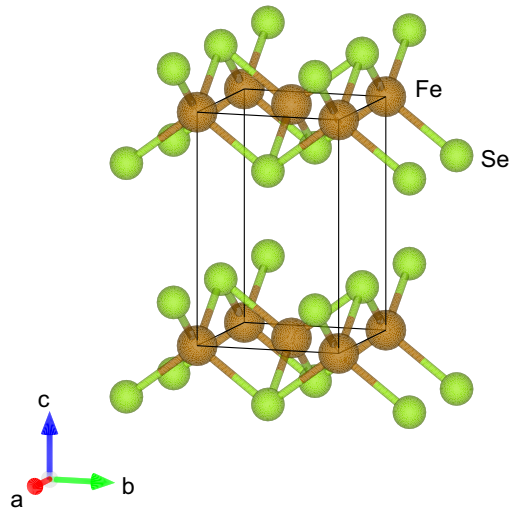

Figure 1.1.4: Crystal structure of FeSe.

Studies on substituting Se in FeSe with Te or S therefore tuning the chemical pressure, or

applying a physical pressure, help build a phase diagram of chalcogenides and bring insights to understanding the underlying mechanism of nematicity and superconductivity [40–43]. One particularly intriguing aspect of $FeTe_{1-x}Se_x$ is its band topology and possible existence of topological superconductivity and Majorana zero mode at superconducting vortex cores [44, 45].

A particularly worth noting aspect of FeSe is the suprising boost of the superconducting T_c when a monolayer of FeSe is deposited on the $SrTiO_3$ substrate which was discovered in 2012 [46]. Tremendous effort has been put into exploring the mechanism underlying the T_c increase [47]. Chapter 3 will be discussing it in more detail.

1.2 Topological phenomena

Topology is a mathematical subject that studies the properties of a geometry under continuous deformation, but it is frequently seen in the context of modern condensed matter physics, probably as much as superconductivity if not even more. The term "topological order" denote the phase of matter which cannot be categorized by a broken symmetry therefore cannot be described by the Laudau symmtery-breaking theory [48]. Band topology describes the properties of the electronic band structure or wave function that resemble the concepts in the mathematical branch of topology. For example, there are invariants that can be calculated from the electronic wave function which will only change if there is a fundamental change in the system. In this section, I will briefly introduce some basic concepts regarding the topological phenomena in condensed matter physics, which are relevant for chapter 4 and 5.

1.2.1 Quantum Hall effect and topological insulator

The story started from the discovery of quantized Hall conductance in a silicon-based MOSFET in 1980 by Klitzing [49]. Classically, in a 2D electron gas where a magnetic field is

applied normal to the 2D plane, the Hall resistance ρ_{xy} can be calculated as a result of the Lorentz force, and it is proportional to the field B. However, when the temperature is low enough and the field is high enough, ρ_{xy} can exhibit plataeus and at the same time the longitudinal $\rho_{xx} = 0$ (and $\sigma_{xx} = 0$), namely the system is in an insulating state (Fig. 1.2.1). Modern-day quantum Hall experiments are mostly performed in the extremely clean 2D electron gas in GaAs heterostructures and in graphene where room temperature quantum Hall effect has been realized [50].

The mechanism underlying the quantized Hall conductance is associated with the Landau levels as a result of the quantum mechanical solution of the 2D electron gas in a magnetic field. The energy levels are discrete and have the form $E_n = (n + 1/2)\hbar\omega_c, n = 0, 1, 2, ...$ where $\omega_c = eB/m^*$ is the cyclotron frequency. Therefore when E_F lies in between these discrete levels, the 2D electron gas is in an insulating state, and when E_F hits the small broadening of each of the Landau levels, the system is metallic.

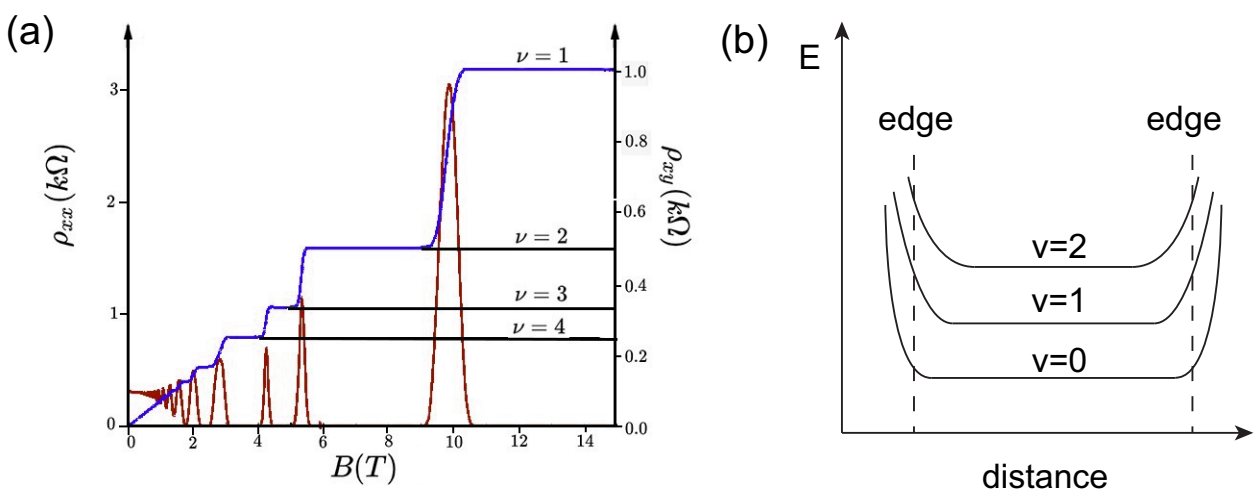

Figure 1.2.1: Quantum Hall effect. (a) Quantized Hall resistance, adapted from Ref. [51] under CC-BY-SA-4.0. (b) Schematic of Landau levels in a sample with boundaries.

The quantized Hall conductance in the insulating states originates from the conductive edge channels as the sample has a finite size, as demonstrated by Laughlin in 1981 [52] and

Halperin in 1982 [53], as shown schematically in Fig. 1.2.1(b). The TKNN paper in 1982 calculated the quantized Hall conductance in a periodic potential using the Kubo formula and found that the quantization corresponds to the integer TKNN number or Chern number [54]. As the magnetic field is increased and E_F crosses each Landau level and enters a new insulating state, the system actually goes through a topological phase transition classified by a different Chern number.

The quantum Hall effect requires an external field thus breaking the time reversal symmetry. In 1988, Haldane proposed a model Hamiltonian on a Honeycomb lattice that does not required a net magnetic flux and would still produce the nonzero Chern number [55], which is the precursor of the quantum anomalous Hall effect heavily explored later. In 2005, Kane and Mele proposed a spin-orbit coupling model that respects the time reversal symmtery and would give rise to a quantum spin Hall state [56], and that initiated the vast research field of topological insulators.

The search for experimental evidence of topological insulator initiated from the proposal of HgTe quantum well [57] and its experimental realization [58] (Fig. 1.2.2(a)). These heavy elements favor a large spin orbit coupling, and when the thickness of the HgTe quantum well exceeds a threshold $d > d_c$, bulk band inversion occurs due to spin-orbit coupling splitting of the p-band which defines a topological insulating phase (Fig. 1.2.2(a)).

3D strong topological insulators which need to be classified by multiple topological indices and are characterized by the insulating bulk state and spin-momentum locked conductive surface states (Fig. 1.2.2(b)) were discovered a few years later, greatly with the help of the angle-resolved photoemission spectroscopy (ARPES) technique. These 3D topological insulators include $Bi_{1\text{-}x}Sb_x$ [59], Bi_2Se_3, Bi_2Te_3 and Sb_2Te_3 [60–63]. An interesting fact is that all the topological materials were precisely predicted first and then experimentally found owing to the accuracy of the single-particle approximation in this context, in contrast to the field of unconventional superconductors.

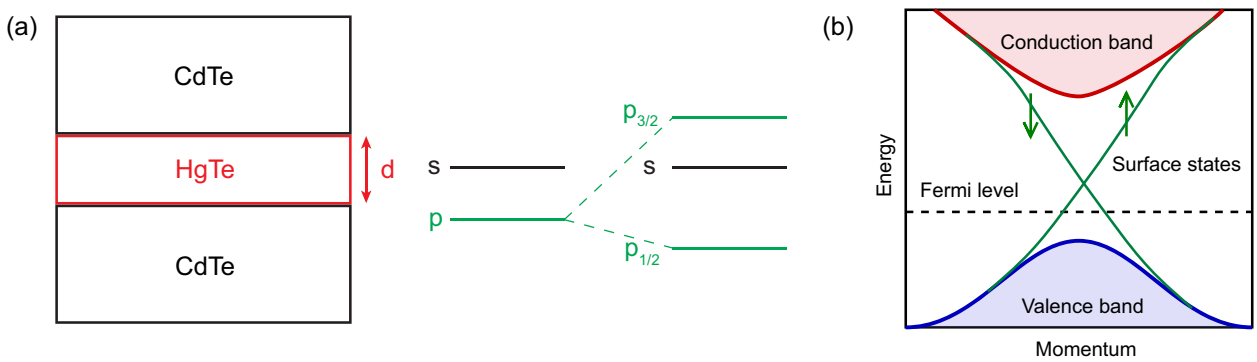

Figure 1.2.2: (a) Left: CdTe/HgTe/CdTe quantum well schematic. d denotes the thickness of the HgTe layer. Right: schematic of the band inversion in HgTe quantum well due to spin-orbit coupling splitting of the p-band. (b) Schematic of the generic band structure of topological insulator, adapted from Ref. [64] under CC-BY-SA-3.0.

In chapter 4, I will discuss our attempt to dope a topological insulator Bi_2Se_3 thin film with magnetic Fe atoms.

1.2.2 Weyl semimetal

One of the most significant equations in physics is the Dirac equation that is the foundation of the relativistic quantum theory [65]:

$$(i\gamma^{\mu}\partial_{\mu} - m)\Psi = 0 \tag{1.9}$$

Weyl further simplied this equation in odd dimensions [66]. Particularly, in 3-dimensions, the massless ($m = 0$) Dirac equation can be simplied as

$$i\partial_t \Psi_{\pm} = (\mp \mathbf{p} \cdot \boldsymbol{\sigma})\Psi_{\pm} \tag{1.10}$$

where $\boldsymbol{\sigma} = (\sigma_x, \sigma_y, \sigma_z)$ denotes the Pauli matrices. The momentum of the Weyl fermions is coupled to the spin and the $+/-$ sign defines the chirality. The Energy dispersion is linear

as a function of the momentum: $E(\mathbf{p}) = \pm|\mathbf{p}|$.

In the context of condensed matter physics where the nonrelativistic quantum mechanics is suitable for the energy scale of interest, the relevance to the Weyl equation appears in the study of the accidental degeneracies in the band structure [67]. Consider the most generic two band Hamiltonian $H(\mathbf{k}) = f_1(\mathbf{k})\sigma_x + f_2(\mathbf{k})\sigma_y + f_3(\mathbf{k})\sigma_z$ (neglecting the identity term), the energy spectrum is $E(\mathbf{k}) = \pm\sqrt{f_1^2(\mathbf{k}) + f_2^2(\mathbf{k}) + f_3^2(\mathbf{k})}$, and the band touching point $E = 0$ occurs only when $f_i(\mathbf{k}) = 0, i = 1, 2, 3$. We shall see that this can generically occur in three dimensions, since $f_i(\mathbf{k}) = 0$ defines a surface and the three surfaces would intersect at a single point ($\mathbf{k} \equiv \mathbf{k}_0$). Therefore, without any symmetry (especially not simultaneously time reversal symmetry and inversion symmetry which lead to doubly degenerate bands [68]), such band touching exist naturally. In the vicinity of $\mathbf{k}_0$, if we assume the band velocity along x, y and z are identical, first order expansion of the two band Hamiltonian has exactly the form of the Weyl equation [68]. Furthermore, such generic band touching cannot be removed by a small perturbation but can only annihilate with another Weyl node.

To find Weyl nodes in real materials, one should look for those that breaks the time reversal symmetry $\mathcal{T}$ or the inversion symmetry $\mathcal{P}$. The latter was experimentally discovered first in a series of transition metal monopnictides [69–71] and transition metal dichalcogenides [72–74]. The former was discovered more recently in magnetic systems [75–79]. One of the key differences between these two classes is that in $\mathcal{T}$-broken, $\mathcal{P}$-preserved system, the minimal number of Weyl points is 2, while in $\mathcal{P}$-broken, $\mathcal{T}$-preserved system, the minimal number is 4.

Notably, there are a few characteristics of the Weyl fermions in a solid in contrast to the Weyl particles in much higher energy scale. First, the Lorentz invariance is allowed to break, enabling the discovery of type-II Weyl semimetals. Moreover, because Weyl points are the sink or source of Berry curvature and due to a net zero Berry curvature in the crystal, Weyl points have to come in pairs of the opposite chiralities, and Fermi arc states

exist at the surface. Finally, the chiral anomaly can be readily observed as the negative magnetoresistance in transport experiments if the energy of Weyl nodes is near the Fermi level.

In chapter 5, evidence for plethora of tunable Weyl points in a magnetic kagome thin film Fe_3Sn_2 synthesized by MBE will be discussed [80].

1.2.3 Topological superconductor and proximity effect

In the paper by Fu and Kane [81], a proximity effect at the interface of a superconductor and a topological insulator was theoretically proposed. By incorporating a Cooper pair term in the Hamiltonian of a time-reversal invariant topological surface state, the low-energy spectrum of the surface state was found to be a spinless $p_x + ip_y$ superconductor and to host Majorana bound state in its vortices.

Experimentally, tremendous efforts were put into realizing such proximity effect by overlaying a topological insulator with a superconductor, conventional or unconventional, or the other way [82–92].

I have also contributed to two MBE/STM works in this topic, Bi_2Te_3/Fe(Te,Se) [23] and Bi_2Te_3/Bi-2212 [21], which will not be discussed in this thesis.

Chapter 2

Experimental Techniques

2.1 Molecular Beam Epitaxy (MBE)

Molecular beam epitaxy is a versatile technique to synthesize crystalline thin films on a substrate [93–97]. The idea of MBE was first conceived by Günther [98], and the modern MBE instrumentation was pioneered by Alfred Y. Cho [93]. As indicated by the name, the synthesis is achieved by shooting a "molecular beam", i.e. the constituent atoms or molecules of the desired thin film, onto a single crystal substrate and forming an epitaxial layer whose crystal orientation is determined by the underlying substrate. While MBE is originally widely used in the semiconductor device manufacturing research and industry, due to its unprecedented precision of the atomic layer-by-layer growth, MBE thin film growth method is also extremely useful in the modern condensed matter physics research, especially now that the low-dimensional physics is of great interest and importance. The important experimental findings that is associated with MBE include the fractional quantum Hall effect discovered in (doped) GaAs/GaAs heterostructures [99], the first experimental realization of a topological insulator in HgTe quantum well [58], the quantum anomalous Hall effect discovered in magnetically doped topological insulator thin films [100] and the surprising boost of superconducting critical temperature in monolayer FeSe/$SrTiO_3$ [101].

Fig. 2.1.1 is a schematic of a typical MBE system. The systhesis occurs in an ultra-high vacuum (UHV) chamber. The substrate is mounted on a manipulator with a heater so that a desired temperature can be reached during growth. "Molecular beam" comes out of the effusion cells at a high temperature and deposits on the substrate. The beam flux rate can be calibrated using a quantz crystal microbalance (QCM) (not shown in the schematic). Reflection high-energy electron diffraction (RHEED) is employed to provide *in-situ* real-time characterization of the surface morphology and crystallinity of the thin film.

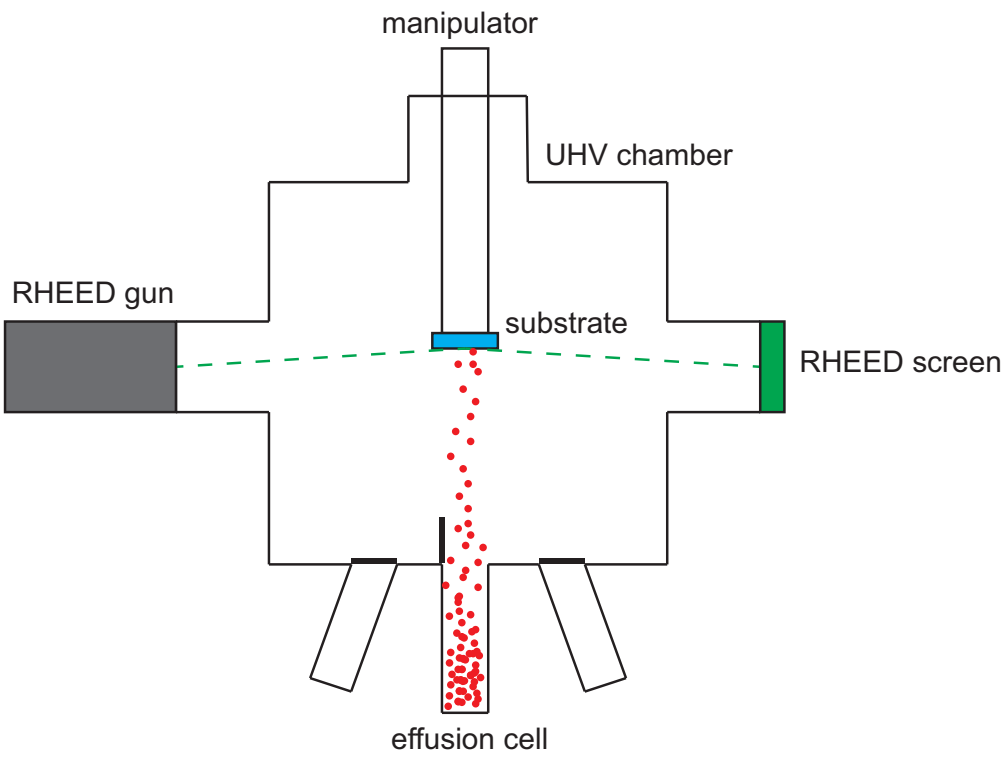

Figure 2.1.1: Schematic of an MBE system.

Fig. 2.1.2 shows the dual MBE system in Zeljkovic Lab at Boston College. It consists of a quick access load lock, an oxide MBE chamber for the growth of oxides and a chalcogenide MBE chamber for the growth of Fe(Te,Se) and Fe_xSn_y. Both MBEs are equipped with Staib RHEED system and Inficon QCM. Manipulators, effusion cells and the integration of the whole system are provided by Fermion Instruments. The base pressure of the oxide MBE can reach 1×10^{-10} Torr after a full bakeout, and 5×10^{-10} Torr for the chalcogenide MBE. The main pump for the oxide MBE is an Edwards STP1003 turbomolecular pump, and for the chalcogenide MBE is a Pfeiffer HiPace300 turbomolecular pump. A programed shuttered growth mode is possible in the oxide MBE. For the oxygen source, ozone, molecular oxygen and oxygen plasma are available in the oxide MBE.

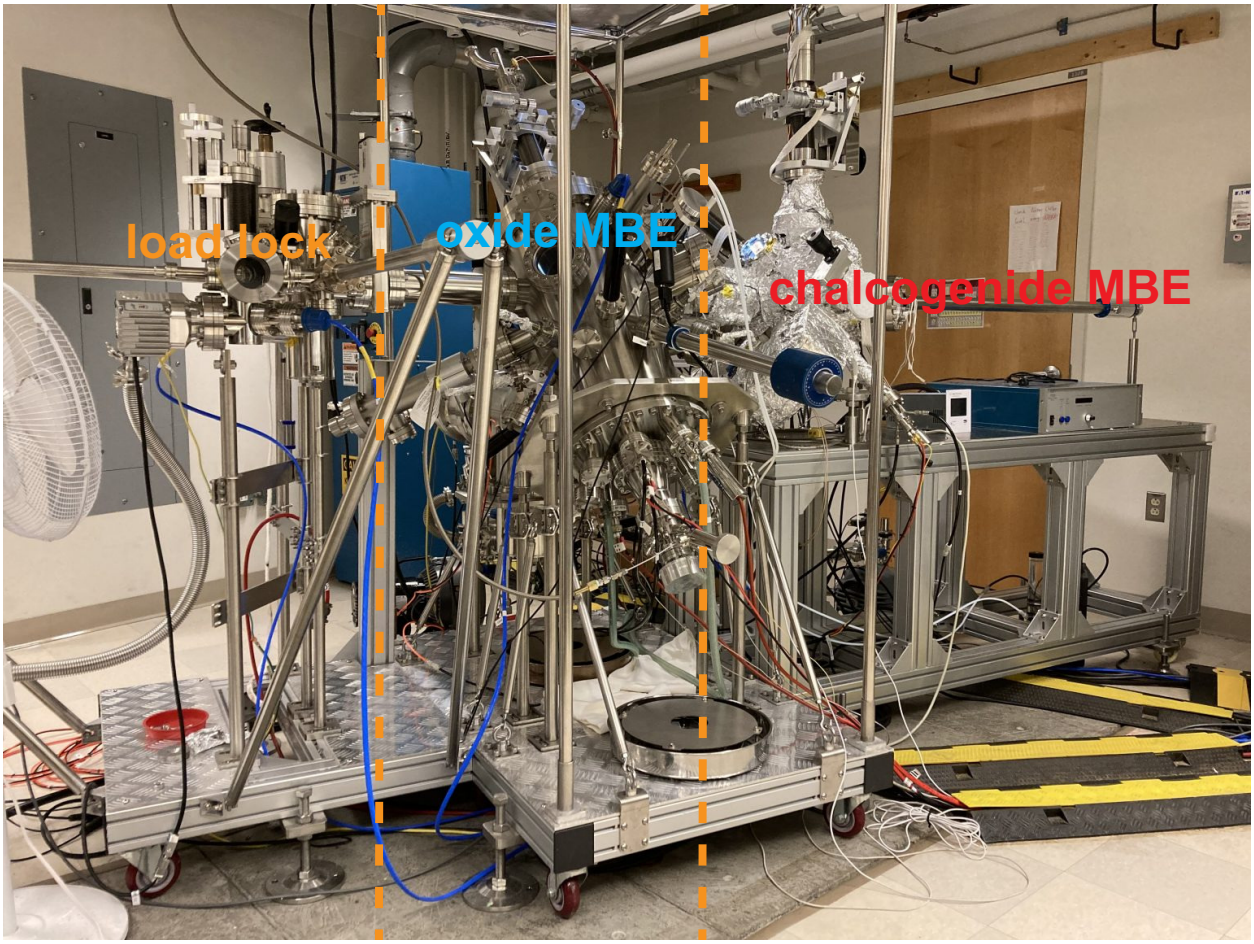

Figure 2.1.2: Dual MBE system in Zeljkovic Lab.

During the thin film growth, RHEED characterization is of the most importance as it is the only real-time method to judge if the quality of the growth meets certain criteria. The analysis of a RHEED pattern is based on the Ewald's sphere analysis, much like the X-ray diffraction. However, due to the small e-beam incident angle (less than 5°), only surface atoms contributes to the interference, and there is no diffraction along the c-axis. Therefore, reciprocal rods intersect the Ewald's sphere and determine the diffraction condition. An atomically flat surface would lead to a sharp RHEED pattern with well-defined bright spots on concentric half-rings. A terraced ordered surface would cause well-defined RHEED streaks. Fig. 2.1.3 shows the comparison of the RHEED pattern of a good thin film and a

bad one (but definitely not the worst).

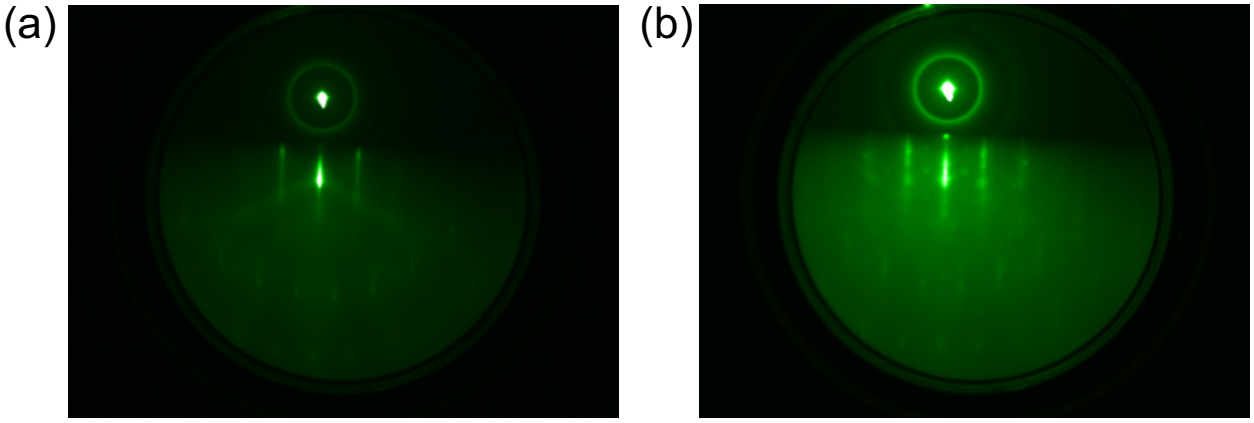

Figure 2.1.3: A good RHEED pattern of a grown film (a) and a bad one (b).

2.2 Scanning Tunneling Microscopy/Spectroscopy (STM/S)

Scanning tunneling microscopy/spectroscopy (STM/S) is a unique instrument to look at the surface of a solid sample with a sub-angstrom resolution. Invented by Binnig and Rohrer in 1980's [102], who were subsequently awarded a Nobel Prize in 1986, STM/S has become an extremely powerful experiental technique in modern condensed matter research. One can visualize the atomic lattice structure on a sample surface with the help of STM/S, and can also extract the local quasiparticle density of states and subsequently the quasiparticle scattering wavepattern by acquiring the differential conductance. Therefore STM/S is able to provide fruitful insights into the electronic structure of a solid.

The instrumentation include an atomically sharp probe, or a "tip", typically made of a simple metal such as tungsten or PtIr, that is mounted on a 3-dimentional piezoelectric motor such that the motion of the tip can be controlled with sub-angstrom precision. When the tip is brought as close as a few Å from the sample and a bias voltage is applied between the tip and the sample, quantum mechanical tunneling of electrons occurs. The tunneling current can be calculated using the "Fermi's golden rule" as derived below.

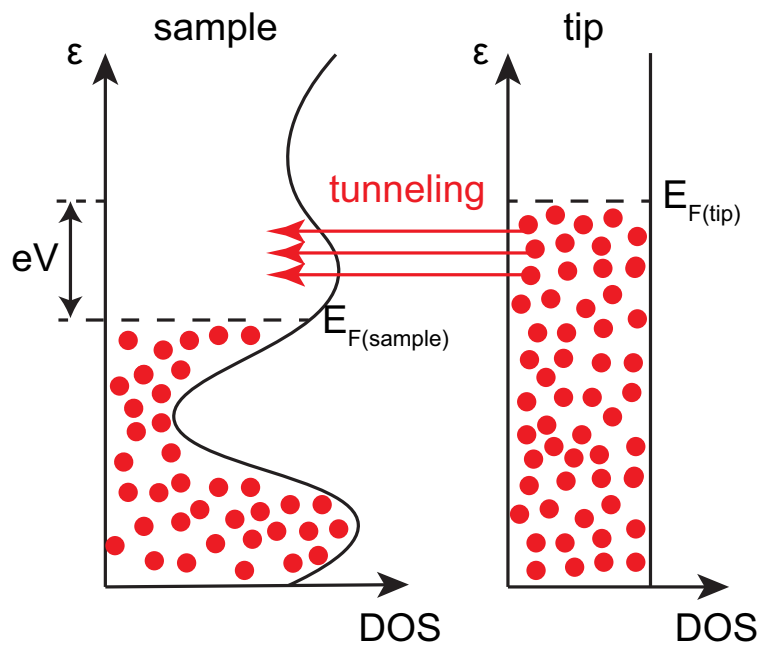

Figure 2.2.1: Schematic of the electron tunneling between STM tip and sample.

When a bias voltage V is applied to the sample, it is to equivalently shift the Fermi level of the sample down by eV with respect to the Fermi level of the tip (Fig. 2.2.1) (here electron charge is -e, e>0), therefore it favors a tunneling current from the tip to the sample. To calculate the net tunneling current, we calculate the tunneling current from the tip to the sample and from the sample to the tip, and find their difference:

$$I_{tip\rightarrow sample} = \int_{-\infty}^{\infty} -2e\frac{2\pi}{\hbar}|M|^2(\rho_t(\epsilon - eV)\cdot f(\epsilon - eV))\cdot(\rho_s(\epsilon)\cdot(1 - f(\epsilon)))d\epsilon \tag{2.1}$$

$$I_{sample\rightarrow tip} = \int_{-\infty}^{\infty} -2e\frac{2\pi}{\hbar}|M|^2(\rho_t(\epsilon - eV)\cdot(1 - f(\epsilon - eV)))\cdot(\rho_s(\epsilon)\cdot f(\epsilon))d\epsilon \tag{2.2}$$

So the net tunneling current from tip to sample is

$$I = -\frac{4\pi e}{\hbar}\int_{-\infty}^{\infty}|M|^2\rho_t(\epsilon - eV)\rho_s(\epsilon)[f(\epsilon)\cdot(1 - f(\epsilon - eV)) - f(\epsilon - eV)\cdot(1 - f(\epsilon))]d\epsilon \tag{2.3}$$

here M is the matrix element, $\rho_t(\epsilon)$ and $\rho_s(\epsilon)$ are the density of states of the tip and the

sample, and $f(\epsilon)$ is the Fermi-Dirac distribution function:

$$f(\epsilon) = \frac{1}{1 + e^{\frac{\epsilon}{k_B T}}} \tag{2.4}$$

We can make a few approximations to the equation of tunneling current. First, since the temperature is low compared to Fermi temperature, the Fermi distribution is approximately a sharp cutoff at zero energy. Second, assuming $\rho_t(\epsilon)$ is a constant, which is true for the conventional metallic STM tips near Fermi level, we can take it out of the integrand. Finally, the matrix element M is approximately independent of energy according to Bardeen [103], so it can also be taken out of the integral. Then the tunneling current reads

$$I \approx -\frac{4\pi e}{\hbar} \rho_t |M|^2 \int_0^{eV} \rho_s(\epsilon) d\epsilon \tag{2.5}$$

One note about the matrix element M: assuming that the vacuum barrier is a simple square barrier, and using the WKB approximation, one can write

$$|M|^2 \approx e^{-2\frac{s}{\hbar}\sqrt{2m\phi}} \tag{2.6}$$

where m is the mass of electron, s is the width of the square barrier (or roughly the sample-tip distance) and ϕ is the height of the barrier. Since the tunneling current is proportional to $|M|^2$, a larger ϕ means that changing s by the same amount would cause larger change in the tunneling current, therefore a better resolution.

Putting together everything, the tunneling current reads

$$I \approx -\frac{4\pi e}{\hbar} \rho_t e^{-2\frac{s}{\hbar}\sqrt{2m\phi}} \int_0^{eV} \rho_s(\epsilon) d\epsilon \tag{2.7}$$

Eq. 2.7 is the foundation of all the different types of STM measurements. The experimental handles in a given STM setup include the xyz control of the tip using a piezo, the

tunneling current that one can read and the bias voltage one can vary, all of which allow for many types of measurements.

The first type of measurement is the topography. By connecting the current reading and the piezo in a feedback loop, one can fix the tunneling current as the tip is moved across the sample surface. This is called the constant current mode. According to Eq. 2.7, a constant current results in a constant tip-sample distance s. Therefore, for a sample that has a spacially homogeneous density of states, the topography corresponds to the surface morphology. Note that since the tip has a sub-Å resolution, a topography can often be atomically resolved. However, a lot of times the DOS is not homogeneous across the sample, especially if there are exotic phenomena such as charge order, and in such cases constant-current topograph also shows information about the DOS, rather than just the structural information.

The second measurement type is the dI/dV spectra, which is more profound in terms of the electronic properties of the sample. dI/dV calculated from Eq. 2.7 is

$$\frac{dI}{dV} \approx -\frac{4\pi e^2}{\hbar}\rho_t e^{-2\frac{s}{\hbar}\sqrt{2m\phi}}\rho_s(eV) \tag{2.8}$$

Therefore dI/dV is proportional to the DOS of the sample. By turning off the feedback loop, the tip-sample distance is fixed. If one varies the voltage and measures the corresponding tunneling current, one can numerially compute dI/dV hence the DOS, but this would result in very noisy data. In practice, dI/dV is always measured using a lock-in amplifier. A bias modulation dV is applied at each bias voltage datapoint and subsequently the dI is measured and dI/dV can be nicely calculated as a function of V.

The third type of measurement, the DOS map, builts up over the second type. It is to essentially measure the dI/dV spectra as a function of the spatial location at the sample surface along x and y directions. Viewing such dataset as a collection of dI/dV($\mathbf{r}$) maps acquired at different biases, one can extract the spatial distribution of electronic DOS at

different energies. Since the DOS($\mathbf{r}$) map contains the standing wave patterns due to quasi-particle scattering, by doing Fourier transform, one can figure out these scattering wave vectors. Since this can be done at different energies, much information of the electronic band structure can be extracted.

The STM system used in this thesis is the Unisoku USM1300 STM (Fig. 2.2.2).

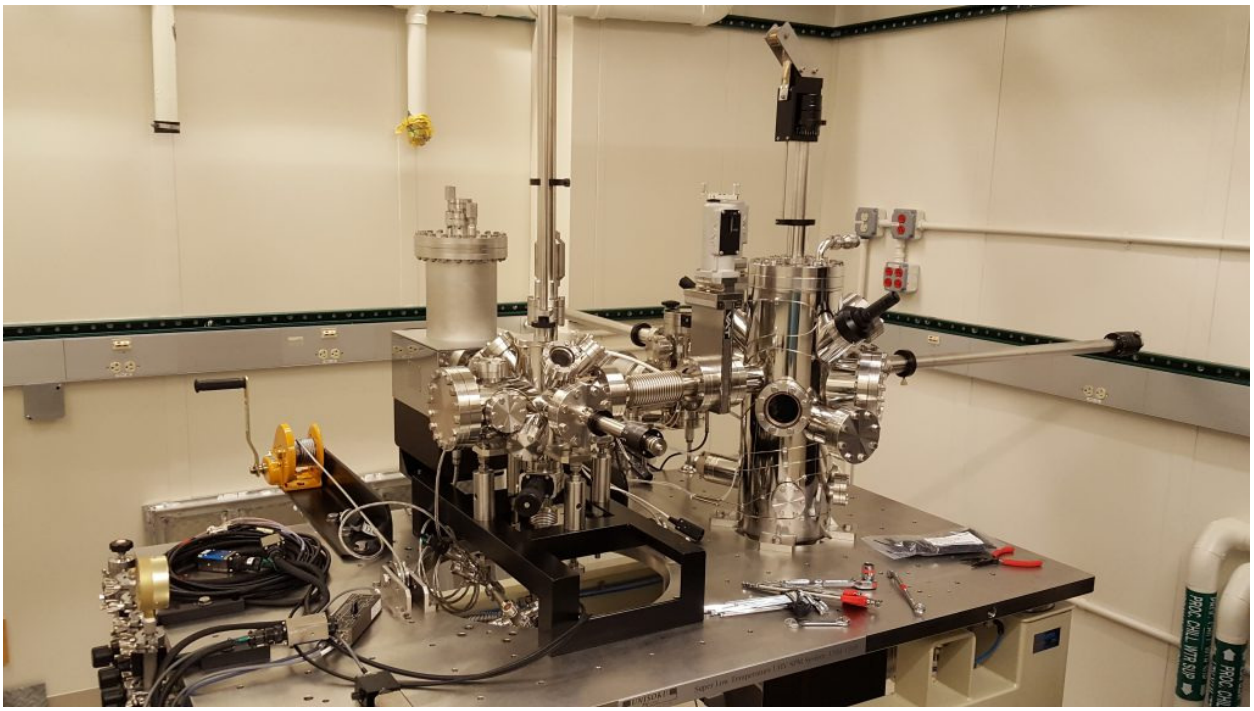

Figure 2.2.2: Picture of the Unisoku USM1300 STM in Zeljkovic Lab.

2.3 Other Techniques

Besides the MBE for thin film syntesis and the STM/S for characterization of sample surface, other experimental techniques that were used in this thesis include X-ray diffraction for bulk crystal structure characterization, Quantum Design MPMS3 SQUID for measurements of magnetization and an ARS UHV four-point probe station for measuring the resistance. Home-built "suitcase" portable vacuum chamber is used to transfer samples from MBE to STM without exposing them to air (Fig. 2.3.1).

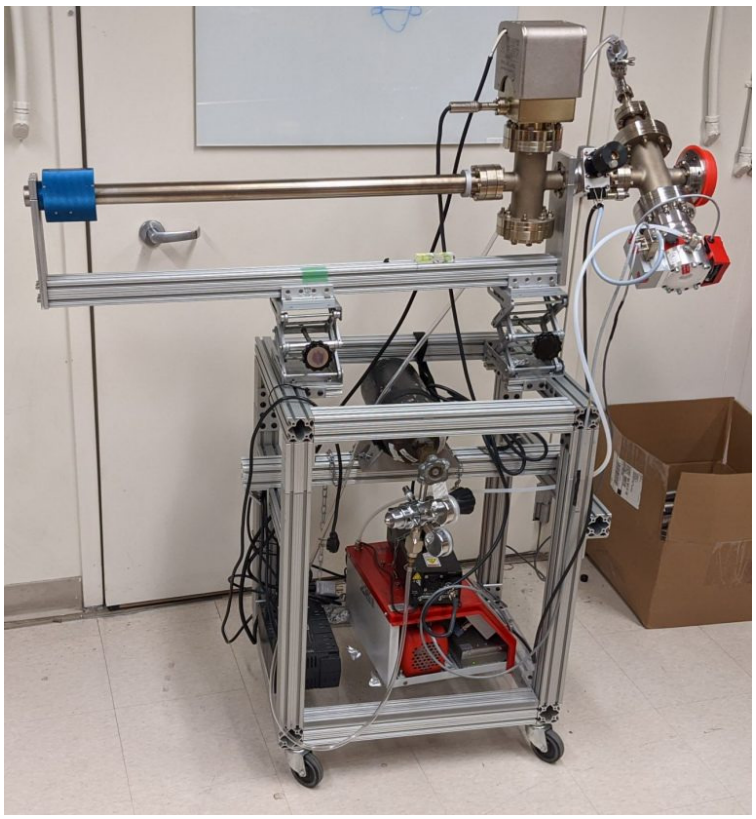

Figure 2.3.1: Picture of the home-built “suitcase” vacuum transfer chamber in Zeljkovic Lab.

Chapter 3

Visualizing a structural network and the electronic nematicity in $FeSe/SrTiO_3(001)$

3.1 Introduction

Nematicity is a rotational symmetry breaking phase and is found to be a key signature of cuprates and Fe-based superconductors due to its close relationshsip with the magnetism and the unconventional superconductivity [28–30, 104–107]. The spontaneous symmetry breaking appears both structurally, i.e. from tetragonal to orthorhombic upon cooling, and electronically, as evident in many measurements involving the electronic properties, including resistivity anisotropy [108–110], lifting of orbital degeneracy [111–115] and scattering of electrons with 2-fold symmetry [116, 117].

Although it is generally believed the electronic nematicity and the structural orthorhombicity appear hand-in-hand macroscopically, and the latter is secondary to the former, which is supported by the beautiful nematic susceptibility experiments [27, 35, 108, 109, 118], a microscopic study of the local correlation of electronic nematicity and the lattice distortion is lacking. In this chapter, I will present such a microscopic study using STM/S that probes both local electronic nematicity and local lattice deformation on $FeSe/SrTiO_3$ thin films grown by MBE.

I will first introduce the growth method and the characterization of the 1 monolayer FeSe film. Next I will describe in detail the characterization of the local lattice distortion, and then the visualization of electronic nematicity. I will discuss the interpretation of our data, which is an elaboration of our published work [119]. In the last two sections, I will show some unpublished interesting data.

3.2 Substrate Preparation and MBE Thin Film Synthesis

The pre-growth substrate preparation plays a central role in determining the quality of the FeSe film [47]. Various substrate preparation methods have been reported from different groups, but they typically include *ex-situ* etching and annealing and *in-situ* annealing treatment. The chemical etching can be done using deionized water [120] or (buffered) HCl [121, 122]. *Ex-situ* annealing can be performed in air [121, 123] or in oxygen [120, 122] at ∼1000 °C. *In-situ* annealing is essential for cleaning the substrate after it is introduced into the MBE chamber, and typically done at elevated temperatures above the tempeture for growth for a fraction of to several hours [120, 121, 123–125]. It has been shown that these preparation steps produce a double-layer TiO_2 termination on the surface of the substrate with certain reconstructions, which favors the growth of FeSe film [122]. Besides these preparation methods, another treatment, namely *in-situ* annealing at 950 °C in Se flux, stemming from the very first FeSe/$SrTiO_3$ work [101], was implemented by some groups. This step was hypothesized to create Se_O substitution sites, which favor the growth and also provide electron doping from oxygen vacancy and further contribute to the superconductivity [126].

The substrate we use is 0.05 wt% Nb-doped STEP $SrTiO_3$(001) from Shinkosha Co., Ltd. We first clean the substrate in a ultrasonic bath with acetone and then 2-propanol and dry it with flowing N_2 gas. Without etching (which we have tested using deionized water and HCl solution but the resulted substrate quality turned out to be unsatisfactory), we directly place the substrate in a quartz boat and insert it into a tube furnace (Fig. 3.2.1). Rough lab vacuum pump is used to keep a constant oxygen flow. A flow meter is mounted between the oxygen cylinder and the furnace to determine the flow rate. By trial and error we found that the optimal condition is to turn on the lab vacuum by a small amount and meanwhile to adjust the flow rate to be ∼1.7 L/min. After the oxygen flow is stablized, we ramp up the temperature to 1000 °C at ∼30 °C/min.

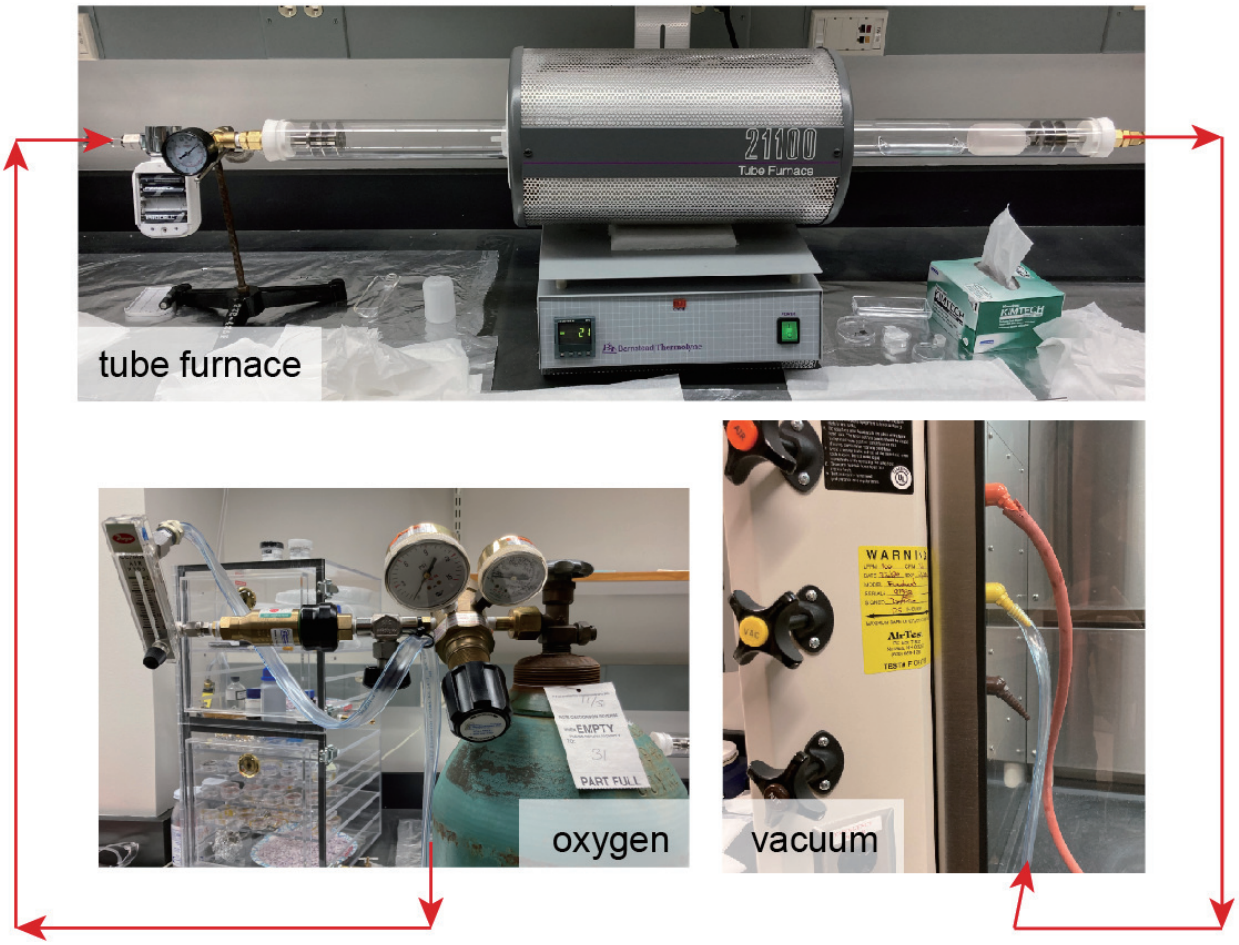

Figure 3.2.1: Picture of the tube furnace setup. The red arrows and lines indicate the directio n of the flowing oxygen.

The annealing at 1000 °C lasts 3 hours and then the furnace gradually cools down, while the same oxygen flow is maintained. We take out the prepared substrate after the furace reaches room temperature and load it in the MBE chamber in minimal time. We found that the proper *ex-situ* oxygen-annealing process leads to a $\sqrt{13} \times \sqrt{13}$ $R33.7°$ $SrTiO_3$ surface reconstruction [122, 127], which is determined by the RHEED image of the substrate and also the STM topograph of 1 ML FeSe film (Fig. 3.2.2(a,b)). In contrast, notably, we also found that if the lab vacuum is not turned up enough such that the oxygen flow rate is sufficiently high, a different surface reconstruction is obtained which results in poorer growth quality

(Fig. 3.2.2(c,d)).

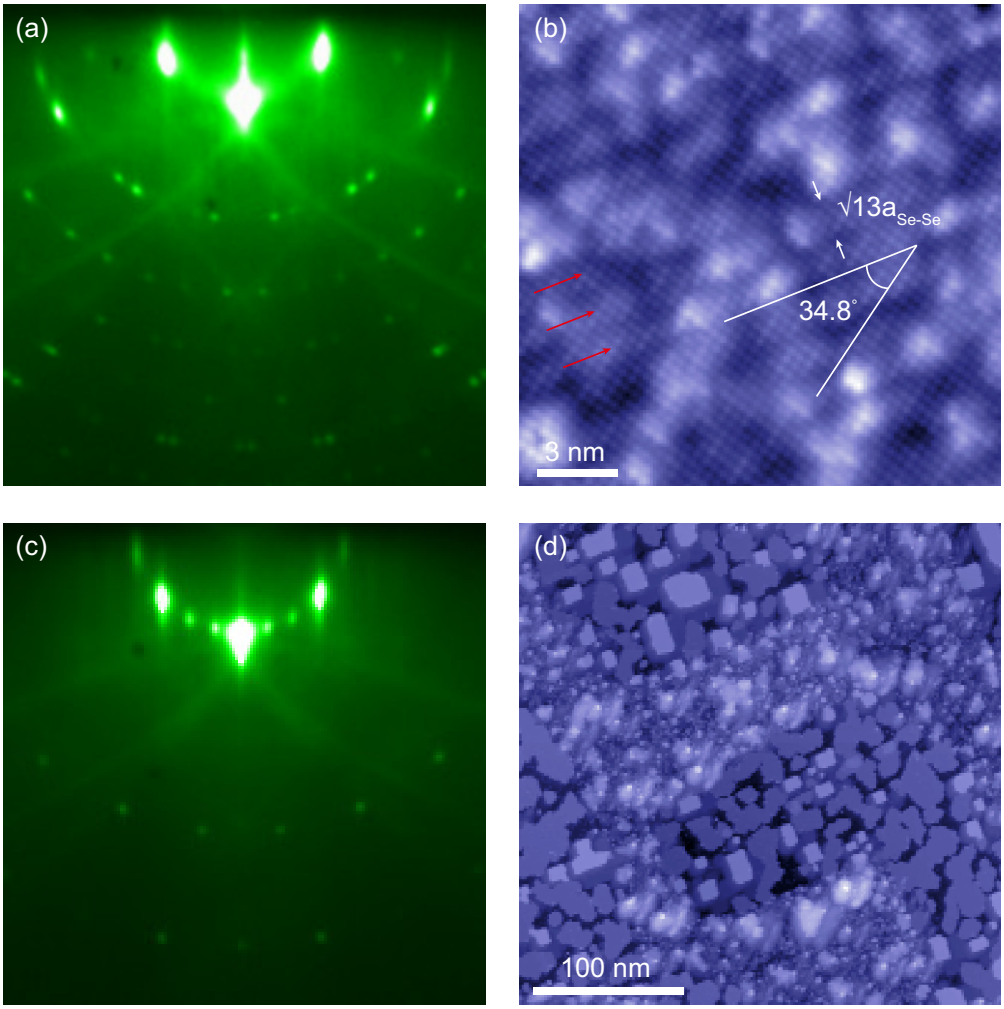

Figure 3.2.2: Surface reconstruction of $SrTiO_3$. (a) RHEED pattern of oxygen-annealed $SrTiO_3$(001) showing $\sqrt{13} \times \sqrt{13}$ $R33.7°$ reconstruction. (b) STM topograph of 1 ML FeSe that shows stripe-like reconstructions. Red arrows indicate the approximate position of some of the stripes. The angle 34.8° is measured between the direction of the stripes and topmost Se-Se lattice vector. The width of the stripes is measured to be $\sim\sqrt{13}a_{Se-Se}$. RHEED was taken using a 15 keV electron gun (Staib). (c) A different type of reconstruction. (d) FeSe film grown on the substrate shown in (c). STM setup condition: (b) I_{set} = 70 pA, V_{sample} = 100 mV. (d)I_{set} = 10 pA, V_{sample} = 1.8 V.

Once the substrate is transferred into the MBE chamber, we slowly heat it up towards the growth temperature at ∼400 °C. We use a pyrometer to determine the temperature of the substrate (emissivity = 0.7 [124]). No higher temperature *in-situ* annealing is done as that seems to bring contamination to the substrate in our case. At the same time Fe and Se Knudsen cells are heated up to their targeted temperature, which are determined by the QCM flux rate calibration beforehand. For most of the growths, temperature for Fe is 1100 °C and for Se, 145 °C, corresponding to the flux rates of 9.87×10^{-5} atoms/(sec·Å^2) for Fe and 3.37×10^{-3} atoms/(sec·Å^2) for Se. The FeSe film growth rate is solely determined by the Fe flux rate, as the growth occurs in a Se-rich environment. The nominal growth rate is ∼23 min/ML, but practically from the completeness of the ML of FeSe in STM topograph, we found that it takes a little longer time, that is ∼28 min, to form a complete ML. The thickness of the film, however, is not that uniform and 1 ML can be coexisting with 2 ML and even 3 or 4 ML.

The growth is monitored by RHEED. A typical RHEED movie that shows the transition from the $SrTiO_3$(001) pattern to the FeSe pattern in a 40-min growth can be found in Ref. [128]. After the deposition is finished, the Knudsen cells are cooled to their standby temperatures and the post-growth sample is kept at the growth temperature or at a slightly higher temperature of ∼450 °C for post-annealing for a few hours or overnight. A temperature higher than 500 °C can possibly make the film decompose, as manifested by the worsening of the RHEED pattern. After post-annealing, the sample is cooled off and transferred into a suitcase vacuum chamber, and then transferred into STM. An alternative way is to cap the film with 10-50 nm thick amorphous Se layer and take it out to air and decap in STM preparation chamber.

3.3 Characterization of Superconducting Monolayer FeSe

Now it is widely known that the 1 ML FeSe/$SrTiO_3$ heterostructure has an astonishingly high superconducting T_c and a large pairing gap [47]. Although we were not able to directly calibrate the T_c of our FeSe film using transport measurements, we observed a superconducting gap of ∼9 meV magnitude in differential conductance spectra repeatedly on the 1 ML FeSe film in STM (Fig. 3.3.1(a)). A larger energy range differential conductance spectra exhibits a gap-like opening (Fig. 3.3.1(b)) that is consistent with the gap at the Γ point [120].

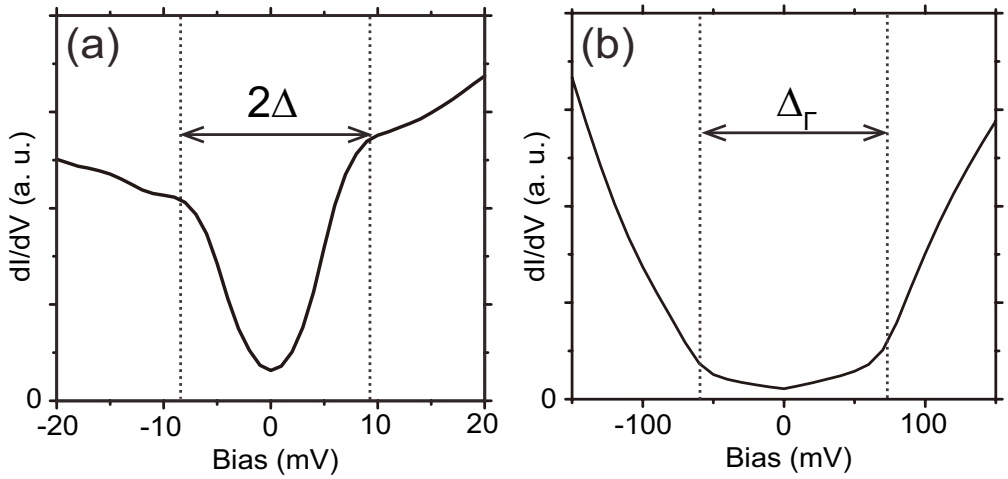

Figure 3.3.1: Superconducting gap of 1 ML FeSe and the gap at Γ point. (a) dI/dV of 1 ML FeSe showing the superconducting gap. (b) The gap at Γ point.

We also observe QPI patterns in 1 ML FeSe in differential conductance maps at various energies (Fig. 3.3.2(a-d)). The Fourier transform shows the ring-like QPI peaks (Fig. 3.3.2(e-h)) that correspond to the interpocket scattering between the electron pockets at M points of the Brillouin zone (Fig. 3.3.2(e) inset) [120].

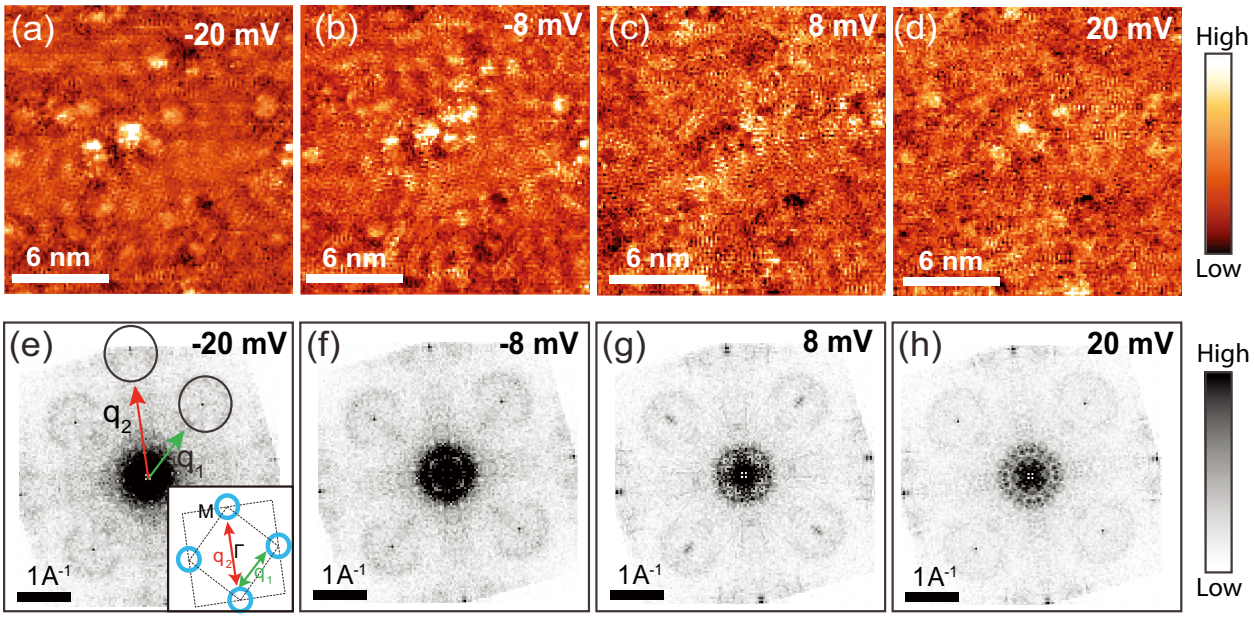

Figure 3.3.2: The QPI on 1 ML FeSe. (a-d) QPI observed in real space in differential conductance maps. (e-h) Fourier transform of (a-d).

3.4 Structural Modulation Observed on Multilayer FeSe and the Experimental Strain Maps

Although the most widely studied is the superconducting 1 ML FeSe and the surface of multi-layer FeSe grown on $SrTiO_3$ does not superconduct, as determined by surface-sensitive techniques [101, 129], the most exciting part of our study is in fact tied to the multi-layer FeSe/$SrTiO_3$. In the STM topographs taken at the surface of multi-layer FeSe, we find a network of structural modulation. As shown in Fig. 3.4.1(a,b), structural modulation lines, forming a square grid, are observed on 3 ML and 4 ML FeSe, while they are absent on 1 ML. Note that each atom spot in panel (b) represents a top layer Se atom (Fig. 3.4.1(c)), therefore the structural modulation lines orient themselves roughly along the Fe-Fe lattice vectors. The distance between neighboring modulation lines in panel (b) ranges from 14 to 21 nm. Similar structural modulation has been reported by cross-sectional transmission

electron microscopy in the same heterostructure [127].

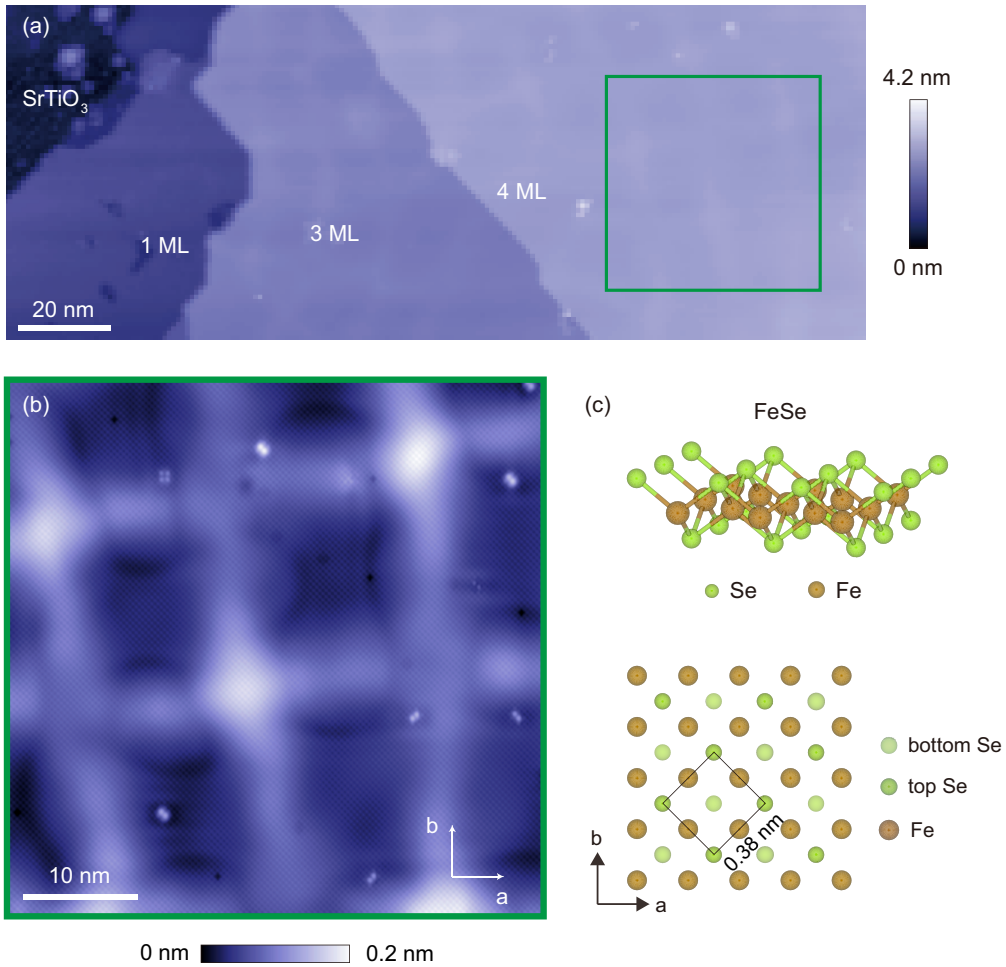

Figure 3.4.1: STM topographs that show the structural modulation network. (a) Large area topograph showing the substrate, 1 ML, 3 ML and 4 ML, as indicated in the figure. (b) Magnification of the region outlined by the green square in (a) a- and b-axis denote the two orthogonal Fe-Fe lattice directions. (c) Schematic that illustrates the crystal structure of FeSe. STM setup condition: (a) $I_{\text{set}} = 10$ pA, $V_{\text{sample}} = 1$ V. (b)$I_{\text{set}} = 60$ pA, $V_{\text{sample}} = 100$ mV.

A natural question to ask related to the structural modulation lines is how they might impact the atomic lattice: is there local displacement/strain induced by the modulation lines upon the crystal lattice? STM is a powerful tool to directly visualize the atomic lattice at

the surface of the sample and can be used to answer this question, as we can compare the real lattice with its perfectly periodic counterpart and figure out the displacement/strain. This approach is based on the Lawler-Fujita drift-correction algorithm [130]. The same method has been successfully applied in several different materials to determine the local atomic displacement or strain [131–134]. Here we give a brief explanation on how this method works.

An STM topograph is a quasi-periodic function $T(\mathbf{r})$ defined in 2-dimentional real space. A perfectly periodic atomic lattice can be expressed in discrete Fourier series:

$$T_{\text{ideal}}(\mathbf{r}) = \sum_i H_i e^{i\mathbf{g}_i \cdot \mathbf{r}}, \tag{3.1}$$

where $\mathbf{g}_i$ represents reciprocal lattice vectors. A real STM topograph, due to the thermal and piezoelectric drift, is distorted from an ideal one. The real topograph can be expressed as

$$T_{\text{real}}(\mathbf{r}) = \sum_i H_i e^{i\mathbf{g}_i \cdot (\mathbf{r} - \mathbf{u}(\mathbf{r}))}. \tag{3.2}$$

Our goal is to find the displacement field $\mathbf{u}(\mathbf{r})$ such that after applying it to the original topograph, i.e. moving the point at $\mathbf{r}$ to $\mathbf{r} - \mathbf{u}(\mathbf{r})$, the processed topograph is perfectly periodic. The key to do this is to realize that there is a difference in the length scale of the $T(\mathbf{r})$ field and the $\mathbf{u}(\mathbf{r})$ field. As the Bragg peaks in the FT of the raw topograph are already very much well defined (only smeared out over a few pixels typically), $\mathbf{u}(\mathbf{r})$ varies in a much *larger* length scale than $T(\mathbf{r})$. Assuming over the length scale L, $\mathbf{u}(\mathbf{r})$ is approximately constant but $e^{i\mathbf{g}\cdot\mathbf{r}}$ traverses multiple wavelengths, we can consider such an integral over the entire plane:

$$T_j(\mathbf{r}) = \int T(\mathbf{r}') e^{-i\mathbf{g}_j \cdot \mathbf{r}'} \frac{1}{2\pi L^2} e^{-\frac{|\mathbf{r}' - \mathbf{r}|^2}{2L^2}} d\mathbf{r}' \tag{3.3}$$

Plugging in Eq. 3.2, this integral reads

$$T_j(\mathbf{r}) = \int H_j e^{-i\mathbf{g}_j\cdot\mathbf{u}(\mathbf{r}')} \frac{1}{2\pi L^2} e^{-\frac{|\mathbf{r}'-\mathbf{r}|^2}{2L^2}} d\mathbf{r}' + \sum_{i\neq j} \int H_i e^{i(\mathbf{g}_i-\mathbf{g}_j)\cdot\mathbf{r}'} e^{-i\mathbf{g}_i\cdot\mathbf{u}(\mathbf{r}')} \frac{1}{2\pi L^2} e^{-\frac{|\mathbf{r}'-\mathbf{r}|^2}{2L^2}} d\mathbf{r}' \tag{3.4}$$

Making use of the assumption that over the length scale L near $\mathbf{r}$, $\mathbf{u}(\mathbf{r}') \approx \mathbf{u}(\mathbf{r})$, we can take the exponential terms containing $\mathbf{u}(\mathbf{r}')$ out of the integral, i.e.:

$$T_j(\mathbf{r}) = e^{-i\mathbf{g}_j\cdot\mathbf{u}(\mathbf{r})} \int H_j \frac{1}{2\pi L^2} e^{-\frac{|\mathbf{r}'-\mathbf{r}|^2}{2L^2}} d\mathbf{r}' + \sum_{i\neq j} e^{-i\mathbf{g}_i\cdot\mathbf{u}(\mathbf{r})} \int H_i e^{i(\mathbf{g}_i-\mathbf{g}_j)\cdot\mathbf{r}'} \frac{1}{2\pi L^2} e^{-\frac{|\mathbf{r}'-\mathbf{r}|^2}{2L^2}} d\mathbf{r}' \tag{3.5}$$

The first term contains an integral of a Gaussian and the second term contains the Fourier transform of a Gaussian which is another Gaussian. The simplified equation reads

$$T_j(\mathbf{r}) = e^{-i\mathbf{g}_j\cdot\mathbf{u}(\mathbf{r})} H_j + \sum_{i\neq j} e^{-i\mathbf{g}_i\cdot\mathbf{u}(\mathbf{r})} H_i e^{i(\mathbf{g}_i-\mathbf{g}_j)\cdot\mathbf{r}} e^{-\frac{L^2}{2}|\mathbf{g}_i-\mathbf{g}_j|^2} \tag{3.6}$$

Note that the length scale L is large compared to the period of the lattice, i.e. $|\mathbf{g}_i - \mathbf{g}_j| >> 1/L$. Therefore $e^{-\frac{L^2}{2}|\mathbf{g}_i-\mathbf{g}_j|^2} \approx 0$, hence

$$T_j(\mathbf{r}) \approx e^{-i\mathbf{g}_j\cdot\mathbf{u}(\mathbf{r})} H_j \tag{3.7}$$

To summarize, we compute $T_j(\mathbf{r})$ for all Bragg peaks numerically using Eq. 3.3 from the raw topograph and then find the displacement field $\mathbf{u}(\mathbf{r})$ using Eq. 3.7. Applying the $\mathbf{u}(\mathbf{r})$ to the raw topograph, we can generate a drift-corrected topograph where each Bragg peak is much better concentrated in one pixel. An example of drift correction on an atomically resolved STM topograph is shown in Fig. 3.4.2.

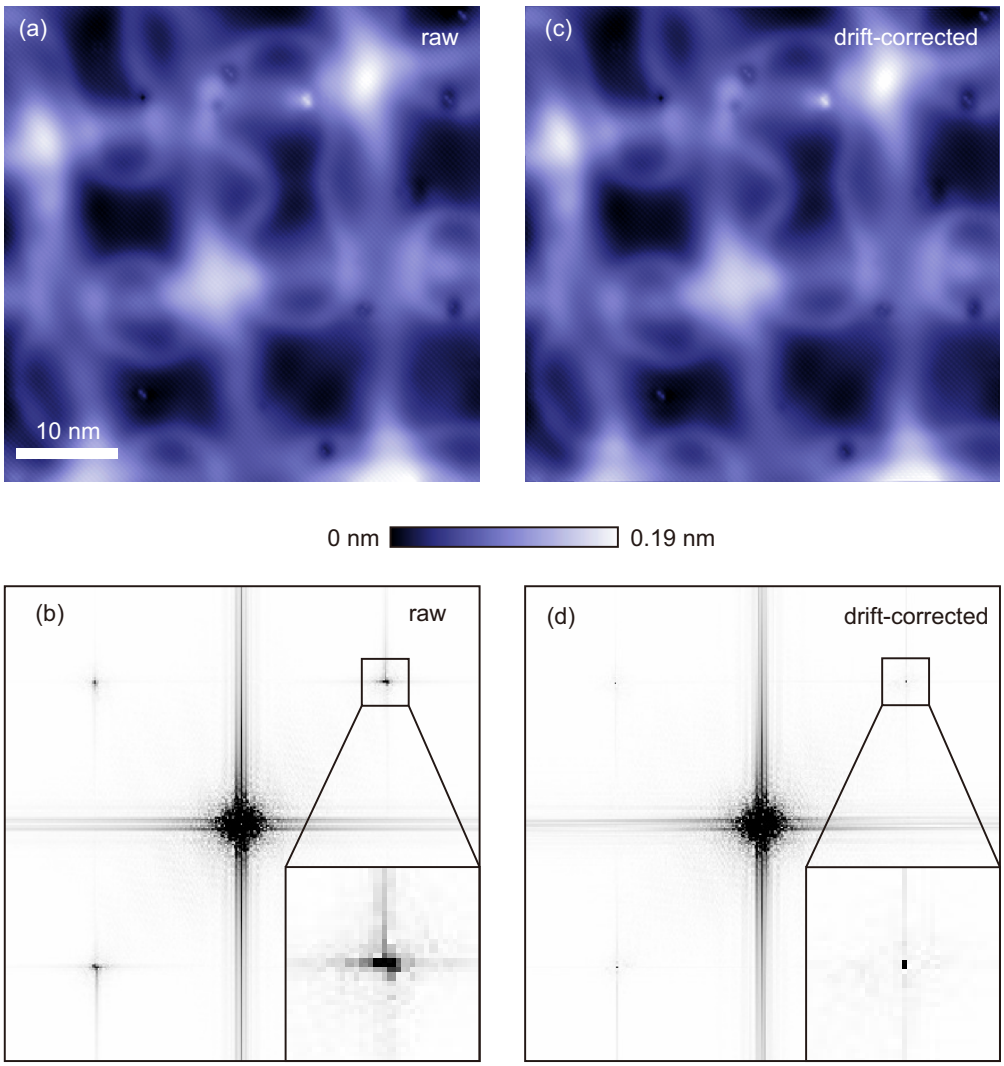

Figure 3.4.2: Drift correction. (a,b) Raw topograph and FT. (c,d) Drift-corrected topograph and FT. Coarsening length scale used here is $L = 2a$ where a is the lattice constant.

This is yet the end of the story. Thermal and piezoelectric drift usually causes a displacement field varying on a large length scale and one can examine this on the $\mathbf{u}(\mathbf{r})$ maps generated using the algorithm described above. However, if there are finer features in $\mathbf{u}(\mathbf{r})$ maps, they could be real structural displacements in the material, i.e. strain. To extract the real strain, we first filter out the long-wavelength background that is due to the thermal and piezoelectric drift of the STM scanner by 2nd-degree-polynomial fitting the $\mathbf{u}(\mathbf{r})$ maps and

subtracting that from the $\mathbf{u}(\mathbf{r})$ maps. Thereafter, according to the definition of the strain tensor, i.e.

$$\begin{pmatrix} \epsilon_{xx} & \epsilon_{xy} \\ \epsilon_{yx} & \epsilon_{yy} \end{pmatrix} = \begin{pmatrix} \frac{\partial u_x}{\partial x} & \frac{1}{2}(\frac{\partial u_x}{\partial y} + \frac{\partial u_y}{\partial x}) \\ \frac{1}{2}(\frac{\partial u_y}{\partial x} + \frac{\partial u_x}{\partial y}) & \frac{\partial u_y}{\partial y} \end{pmatrix} \tag{3.8}$$

we can calculate each component of the strain tensor. The $\mathbf{u}(\mathbf{r})$ field can be decomposed into any two orthogonal axes, not just x,y-axis, and the strain tensor can be calculated along those two axes. It's easy to prove the strain tensor satisfies a rotational transformation. For example, assuming a,b-axis are clockwise rotated from x,y-axis by 45°, strain tensors satisfy

$$\begin{pmatrix} \epsilon_{aa} & \epsilon_{ab} \\ \epsilon_{ba} & \epsilon_{bb} \end{pmatrix} = \begin{pmatrix} \frac{1}{\sqrt{2}} & -\frac{1}{\sqrt{2}} \\ \frac{1}{\sqrt{2}} & \frac{1}{\sqrt{2}} \end{pmatrix} \begin{pmatrix} \epsilon_{xx} & \epsilon_{xy} \\ \epsilon_{yx} & \epsilon_{yy} \end{pmatrix} \begin{pmatrix} \frac{1}{\sqrt{2}} & \frac{1}{\sqrt{2}} \\ -\frac{1}{\sqrt{2}} & \frac{1}{\sqrt{2}} \end{pmatrix} \tag{3.9}$$

Strain components calculated for the topograph in Fig. 3.4.2(a) are shown in Fig. 3.4.3. They are calculated along Fe-Fe a,b-axis as defined in Fig. 3.4.1. Coarsening length scale as defined above, $L = 2a$ and $L = 5a$ (a is the lattice constant) are used and shown separately.

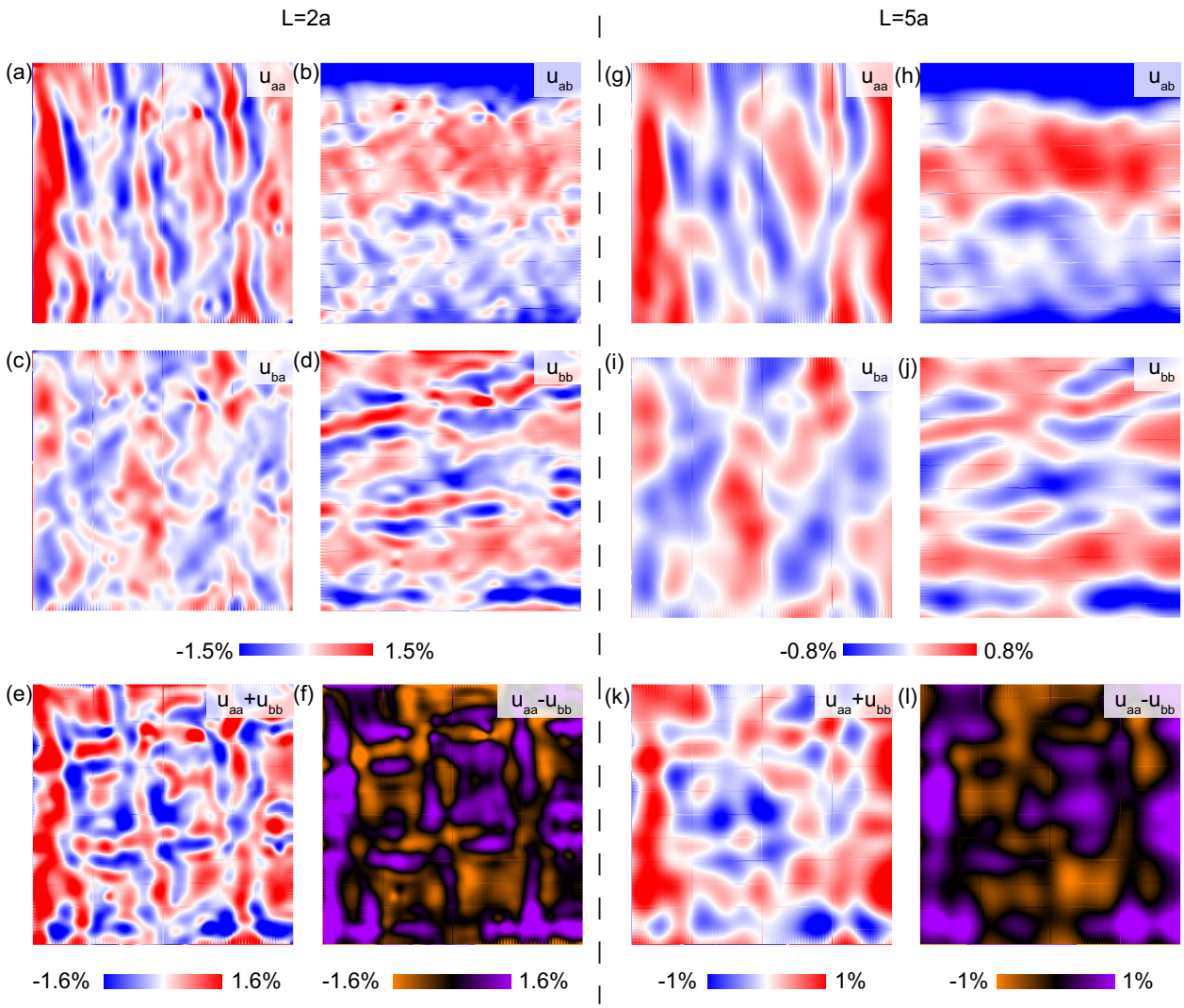

Figure 3.4.3: Strain components of the topograph as described in the text. (a-d) Strain components $u_{ij} = \partial u_i / \partial u_j$ ($i, j = a, b$; a, b-axis are defined in Fig. 3.4.1) using $L = 2a$. (e,f) symmetric and antisymmetric strain components $u_{aa} + u_{bb}$ and $u_{aa} - u_{bb}$ using $L = 2a$. (g-l) corresponding strain components similar to (a-f) using $L = 5a$.

3.5 Dislocation Network Modeling and Theoretical Strain Maps

It is crucial to understand the origin of the structural modulation. We can attribute a single, isolated structural ridge/trough to the imperfectness of the sample, but the grid-like

modulation observed here is not random. In fact, similar periodic structural modulations have been reported in other epitaxial heterostructures, for example, in PbTe/PbSe(001) [135] and in SnTe/PbSe [132, 134]. In those heterostructures, usually consisting of two similar FCC rock salt materials with a small lattice mismatch, the origin of the structural modulations is understood to be the edge dislocations [135]. Dislocations are line defects embedded in the sample or usually appearing at the interface of a heterostructure. In lattice mismatched epitaxial film growths, dislocation lines are a mechanism for strain relief when the thickness of the film reaches a critical thickness hence large amount of strain energy is accumulated [136]. For each dislocation line, the structural deformation looks essentially like an additional or missing half plane of atoms on one side of the line as schematically shown in Fig. 3.5.1.

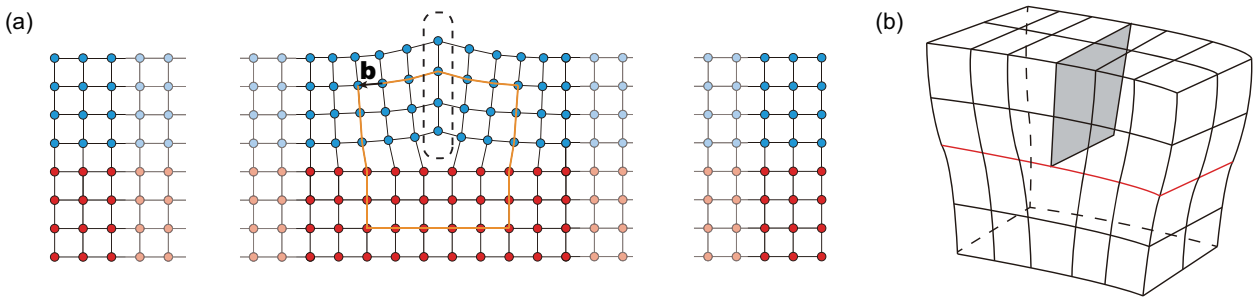

Figure 3.5.1: Schematics of an edge dislocation. (a) Front view of the lattice structure containing the extra half plane of blue atoms in the dashed box. **b** is the Burgers vector. (b) 3D schematic of the edge dislocation.

Unless the dislocation lines form a grid or end at the edge of the sample, an isolated dislocation core should ends as two threading dislocation impurities on the surface. The threading dislocation impurities are direct evidence that the structural modulation lines are caused by dislocations. We observe the threading dislocations in STM topographs where the modulation grid is broken (Fig. 3.5.2).

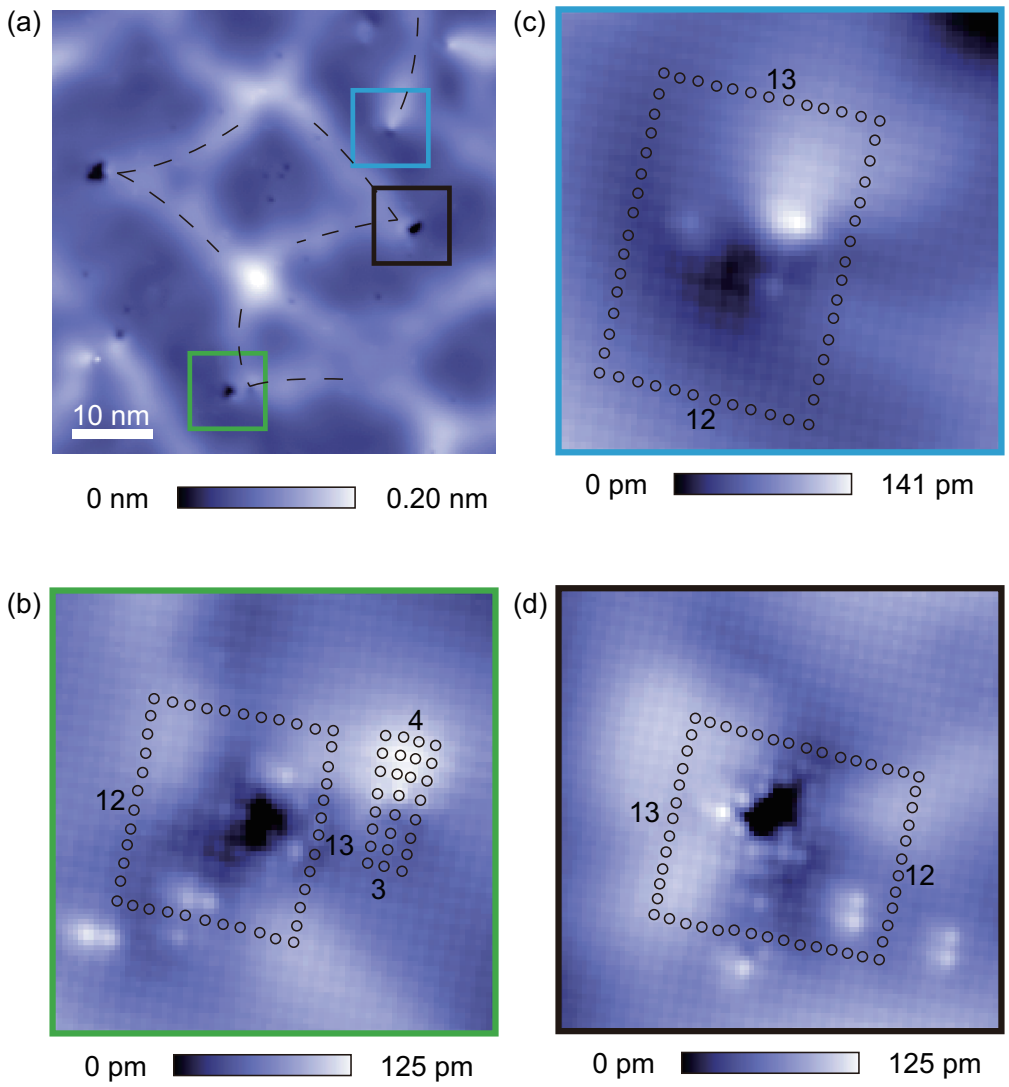

Figure 3.5.2: Threading dislocations observed on the surface of FeSe. (a) A 55×55 nm area containing at least six threading dislocation impurities. (b-d) Magnifications of three of the threading dislocations outlined by green, blue and black boxes. Each little circle indicates an Se atom. The numbers indicate the one atom offset on the two side of a dislocation impurity. STM setup condition: (a) $I_{\text{set}} = 10$ pA, $V_{\text{sample}} = 1$ V.

The elastic properties of the dislocations have been studied and understood very well on the classical level and can be found in numerous textbooks of this subject. Here we are mainly interested in the displacement field and strain caused by the dislocation lines and

the comparison between the theoretical strain field based on an edge dislocation model and the experimental strain field extracted from atomically resolved STM topographs using the Lawler-Fujita algorithm. It turned out the most elementary dislocation model, i.e. one that assumes a homogeneous continuous medium, works quite well. Based on the derivation in Ref. [137], the in-plane displacement field u_x, in the bulk of continuum, of a single edge dislocation line has the form:

$$u_x = \frac{b}{2\pi}\left[\arctan\frac{y}{x} + \frac{xy}{2(1-\nu)(x^2+y^2)}\right] \tag{3.10}$$

where x is the distance to the dislocation core in the direction parallel to the Burgers vector (in-plane) and y is the distance to the dislocation core along the out-of-plane direction; b is the Burgers vector and ν the Poisson's ratio.

As we are interested the displacement field on the surface of the film, an extra boundary condition has to be taken into account while deriving the displacement field: the stress should vanish in the direction normal to the surface. Therefore the u_x field on the surface should take the following form [138]:

$$u_x = \frac{b}{\pi}\left[-\arctan\frac{x}{d} + \frac{xd}{(x^2+d^2)}\right] \tag{3.11}$$

where d is the depth of the dislocation core from the surface. Note that of a single edge dislocation line, the displacement parellel to it vanishes. Now taking the derivative of the displacement would give us an estimate of the strain, i.e.

$$u_{xx} = -\frac{2bd}{\pi}\frac{x^2}{(x^2+d^2)^2} \tag{3.12}$$

We set the Burgers vector to be 0.53 nm, i.e. the Se-Se distance along [110] direction in the Se layer of the FeSe ML. The thickness d is set as 1.6 nm, which is roughly the thickness

of 3 ML of FeSe. u_{xx} is plotted as in Fig. 3.5.3(b) inset. To simulate the experimental strain maps as shown in Fig. 3.4.3, we simply calculate the linear superposition of the strain field caused by individual dislocation lines. For example, for u_{aa}, we add up the strain caused by each of the three dislocation lines roughly oriented along b-axis, and the same for u_{bb}. Fig. 3.5.3 demonstrates the theoretically calculated strain maps (we did 2-atom Gaussian smoothing on them). $S(\mathbf{r})$ map is calculated as the summation of u_{aa} map and u_{bb} map. $U(\mathbf{r})$ is calculated by subtracting u_{bb} map from u_{aa} map.

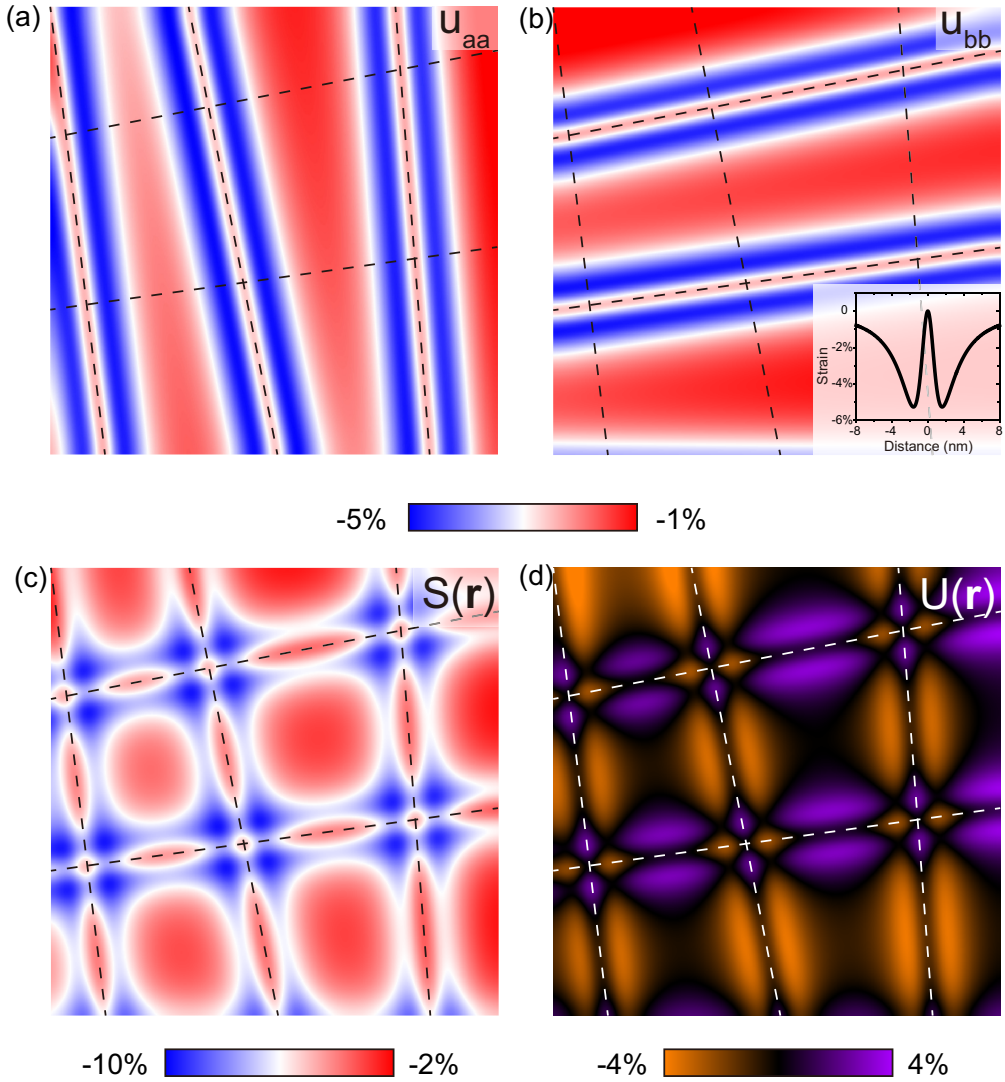

Figure 3.5.3: (a-d) Calculated strain maps u_{aa}, u_{bb}, $S(\mathbf{r}) = u_{aa} + u_{bb}$, $U(\mathbf{r}) = u_{aa} - u_{bb}$. (b) inset plots the u_{xx} profile of a single edge dislocation line.

Note that since the u_{aa} and u_{bb} maps are calculated with respect to the undeformed lattice constant of the substrate, so they always take negative values. However, since $U(\mathbf{r})$ is the difference between u_{aa} and u_{bb}, we can directly compare the landscape and the scale of experimental and theoretical $U(\mathbf{r})$. They show remarkable resemblance (Fig. 3.5.4), indicative of the edge dislocation as the major origin of the strutural modulation.

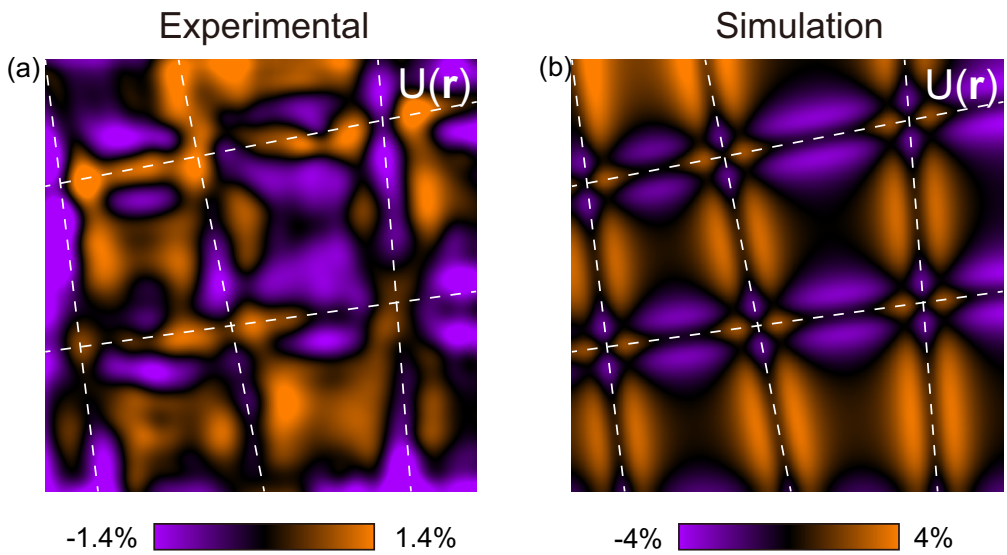

Figure 3.5.4: Comparison between experimental and simulated $U(\mathbf{r})$ maps.

3.6 Visualizing the Electronic Nematic Domains

As discussed in the introduction chapter, nematicity is a ubiquitous rotational-symmetry-broken phase found in both iron pnictides and iron chalcogenides above the critical temperature of the superconducting phase. The broken rotational symmetry appears both structurally and electronically, and it has been generally believed they appear hand-in-hand. STM is able to detect the structural symmetry breaking, as we have done in the previous section, as well as electronic symmetry breaking using $\mathrm{d}I/\mathrm{d}V$ maps.

We aquired $\mathrm{d}I/\mathrm{d}V$ maps over the identical region shown in previous sections from -100 mV to 100 mV with the resolution 256×256 pixels (Fig. 3.6.1, data can also be downloaded from Ref. [139]). As discussed in the experimental techniques chapter, by doing so we are able to visualize any spacially varying electronic density of states.

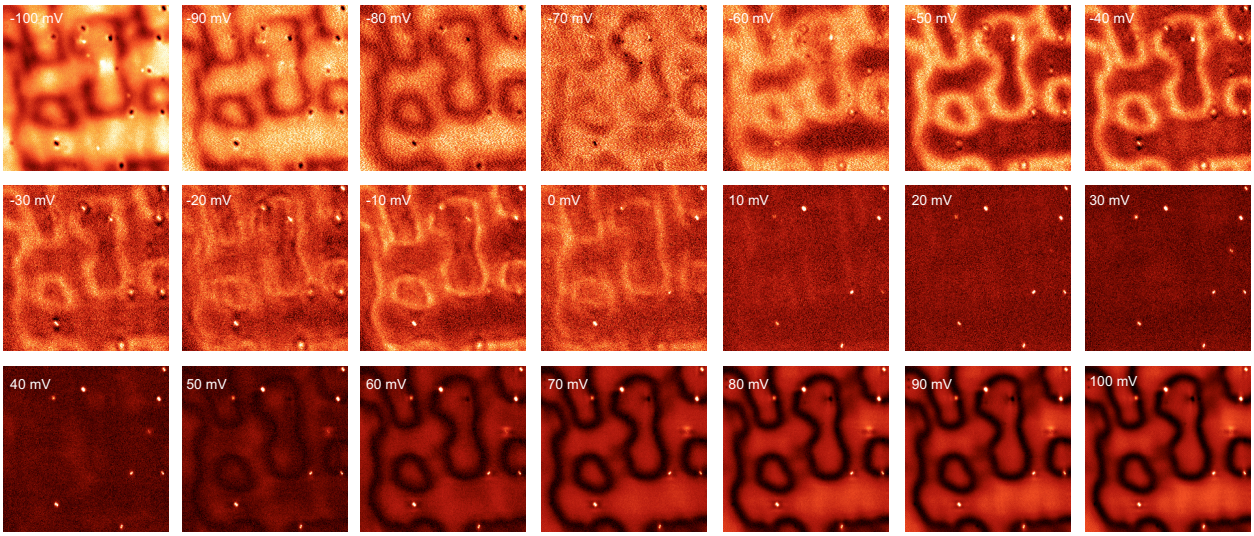

Figure 3.6.1: STM setup condition: I_{set} = 110 pA, V_{sample} = -100 mV, V_{exc} = 5 mV.

In the $\mathrm{d}I/\mathrm{d}V$ maps (or sometimes I maps, which are $\mathrm{d}I/\mathrm{d}V$ maps integrated over some V range), we are able to discern several striking features. First, there are the irregularly shaped contours, either brighter or darker than the rest of the map. Fig. 3.6.1 presents the evolution of these contours as a function of the bias voltage. We denote the regions on the two sides of the contours domain A and B (Fig. 3.6.2(b)). Second, in $\mathrm{d}I/\mathrm{d}V$ maps at some of the biases and, more prominently, in some current maps (Fig. 3.6.2(b)), we observe stripes that are not dispersive as a function of energy (Fig. 3.6.2(c)). The stripes within one domain are oriented along the same direction, but are orthogonal across the domain boundaries (Fig. 3.6.2(b)). The nearest-neighbor spacing between the stripes is ∼1.8 nm. Finally, in contrast to the non-dispersive charge stripes, we notice the dispersive C_2-symmetric modulations pinned to dumbbell-shaped impurities. The directions of the dispersion are again orthogonal in domain A and B (Fig. 3.6.3).

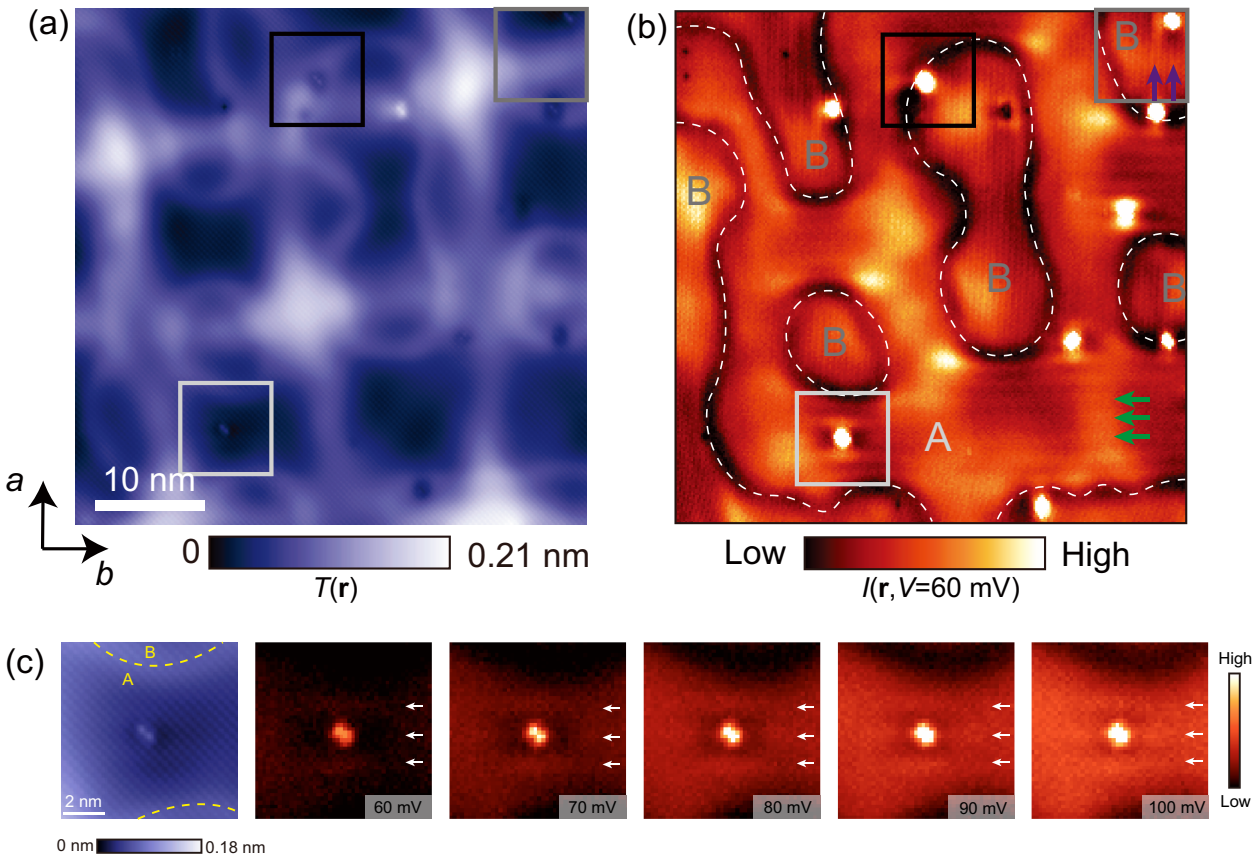

Figure 3.6.2: (a) Topograph. (b) Tunneling current map. A and B denote two orthogonal nematic domains. Green and purple arrows point towards the non-dispersive stripe charge order in domain A and B, respectively. Black, gray and white squares in (a) and (b) outline three dumbell impurites. White dashed lines highlight the nematic domain boundaries. (c) Charge stripes (in $\mathrm{d}I/\mathrm{d}V$ maps) pinned by the impurity in the white square and they are not dispersing as a function of bias. STM setup condition: (a) I_{set} = 110 pA, V_{sample} = -100 mV; (b) I_{set} = 110 pA, V_{sample} = -100 mV; (c) I_{set} = 110 pA, V_{sample} = -100 mV, V_{exc} = 5 mV.

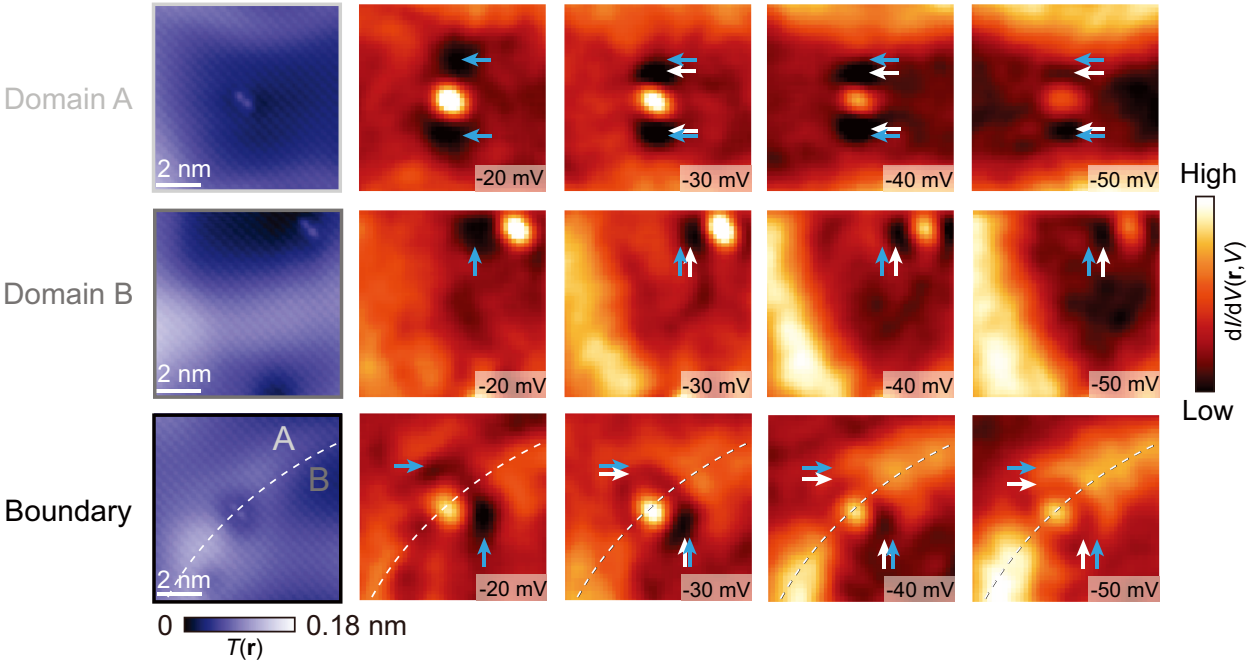

Figure 3.6.3: C_2-symmetric modulations pinned to dumbbell-shaped impurities. Top, middle and bottom rows are associated with the impurities outlined by white, gray and black squares in Fig. 3.6.2(b), respectively. The blue and white arrows are guides to the eye for the C_2-symmetric dispersions. STM setup condition: I_{set} = 110 pA, V_{sample} = -100 mV, V_{exc} = 5 mV.

Similar C_2-symmetric features have been reported in $\mathrm{d}I/\mathrm{d}V$ maps acquired at the surface of bulk iron pnictides [140–142] and chalcogenides [143–145], which are closely associated with the nematic states. Particularly, they have also been reported on the surface of multilayer FeSe/$SrTiO_3$ [146, 147]. In Ref. [146], the authors observed a maze-like nematic domain pattern, which is not exactly the same as what we observed here. We ascribe the difference to the different thickness of the film and we will address this in the remaining sections of this chapter. The nearest-neighbor spacing of their stripes is ∼1.9 nm which is almost identical as our observation. The dispersion of the C_2-symmetric modulations is also similar to what we observed. Per Ref. [146], the non-dispersive stripes point to a local charge order associated with the local magnetic order pinned by the impurities, which is embedded in the

nematic phase. In Fig. 3.6.2, domain A and B are associated with electronic nematicity of two orthogonal orientations.

3.7 Interplay of Structural Modulation and Electronic Nematicity

Now that we have obtained the strain maps and electronic $\mathrm{d}I/\mathrm{d}V$ maps in the identical region, we are able to explore their interplay on an atomic level. In bulk Fe-pnictides/chalcogenides, the amount of structural orthorhombicity is characterized by a dimentionless parameter δ, defined as $\delta = (a-b)/(a+b)$ [148]. Here, to a first approximation, antisymmetric strain $U(\mathbf{r}) \equiv u_{aa} - u_{bb} \approx 2\delta$. Therefore it is meaningful to compare the $U(\mathbf{r})$ map and $\mathrm{d}I/\mathrm{d}V$ map. To do this, first we drift-correct the high resolution topograph acquired independently and the lower resolution topograph acquired at the same time as the $\mathrm{d}I/\mathrm{d}V$ map, and rescale them such that they have identical Bragg peaks. Next, we align them perfectly by adding a constant to the displacement field now that they have identical Bragg peaks. Finally, with these displacement fields, we drift-correct the $U(\mathbf{r})$ map (associated with the high resolution topograph) and the $\mathrm{d}I/\mathrm{d}V$ maps at all biases (associated with the lower resolution topograph). After that, it is legit to superimpose the $U(\mathbf{r})$ map on top of the $\mathrm{d}I/\mathrm{d}V$ maps to directly compare the local features.

In Fig. 3.7.1(c), the domain boundaries (white solid lines) of the electronic nematic domains are superimposed on top of the experimental $U(\mathbf{r})$ map. Even solely with bare eyes without statistical investigations, we are able to discern the correlation of the structural anisotropy and electronic nematicity, namely, within nematic domain A, the $U(\mathbf{r})$ map is colored orange by and large, and within nematic domain B violet. This is consistent with the orientation of the charge stripes or the C_2-symmetric modulations, i.e. if the charge-stripe wave vector is oriented along a-axis, the lattice constant along a-axis would be larger than the lattice constant along b-axis [146]. Notably, the impact of the electronic nematicity

on the structural anisotropy can be found at the central region of each quadrilateral of the structural modulation network, where in the simulated $U(\mathbf{r})$ map $U(\mathbf{r}_{central}) \approx 0$ (Fig. 3.5.4(b)), but in the experimental $U(\mathbf{r})$ map it is further away from zero and highly correlated with each electronic nematic domain (i.e. orange in A and violet in B).

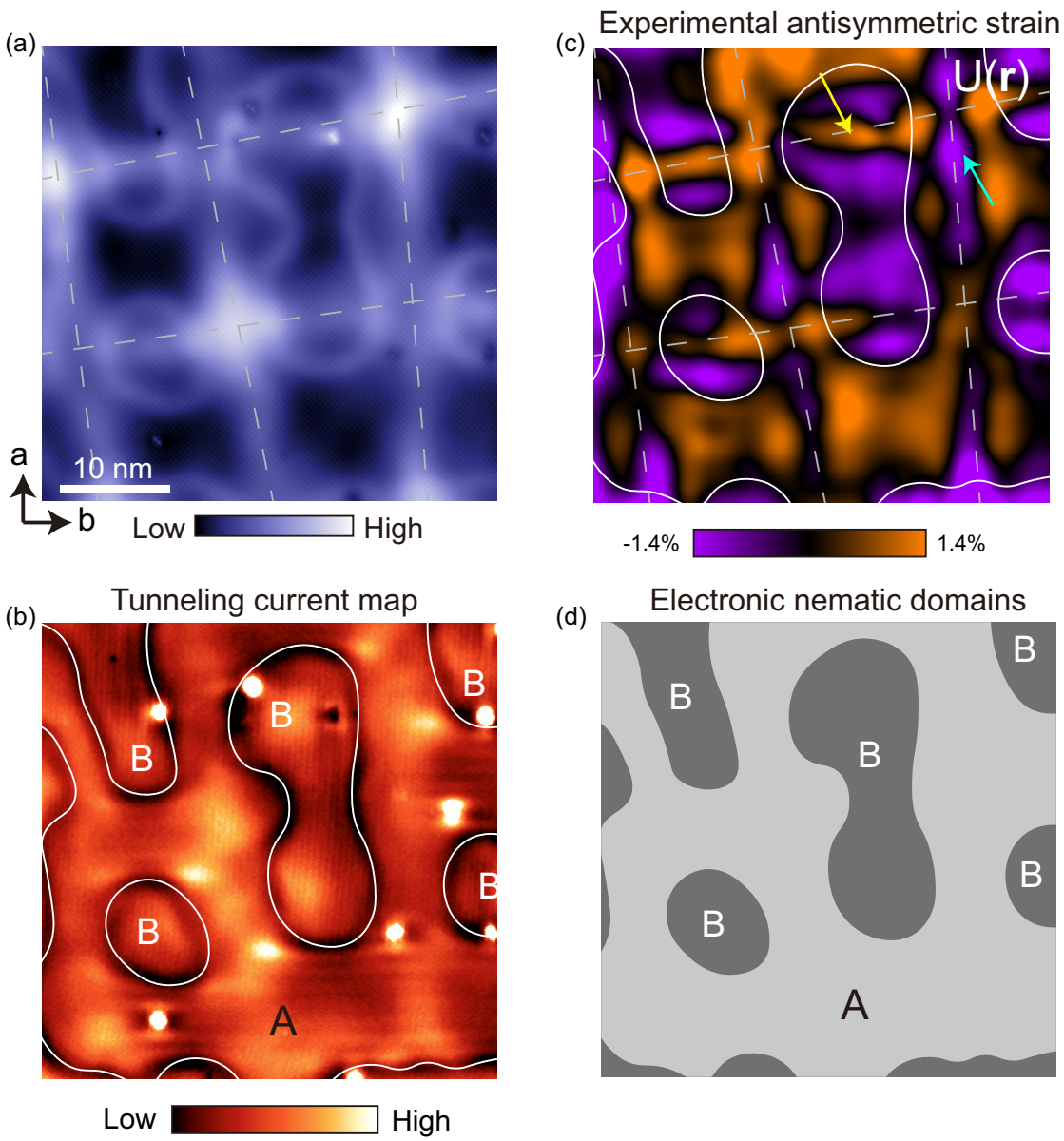

Figure 3.7.1: (a) STM topograph. Dashed lines denote the network of structural modulations. a,b-axis are the Fe-Fe axes. (b) Tunneling current map acquired on the identical region in (a). Solid white lines outline the electronic nematic domains A and B. (c) Experimental $U(\mathbf{r})$ map calculated from (a). Yellow and blue arrows point to where the decoupling of structural anisotropy and electronic nematicity occurs. (d) A schematic showing electronic nematic domains A and B. STM setup condition: (a) I_{set} = 110 pA, V_{sample} = -100 mV; (b) I_{set} = 110 pA, V_{sample} = -100 mV.

However, interestingly, there are minor regions that show apparent decoupling between the structural anisotropy and the electronic nematicity, as pointed by the yellow and blue arrows in Fig. 3.7.1(c). We note that in these regions the $U(\mathbf{r})$ are mostly determined by the edge dislocation lines instead of the electronic nematicity, as one can tell by comparing the experiemental $U(\mathbf{r})$ map and the simulated one and observing the similarities in those minor regions. To statistically survey the correlation of the $U(\mathbf{r})$ map and the electronic nematic domains, we present the histogram of the value of $U(\mathbf{r})$ in each pixel within electronic nematic domain A and B (Fig. 3.7.2(a)). In nematic domain A, while 69% of the area exhibits consistent orientations of structural anisotropy and electronic nematicity, there are 31% of the pixels that show the decoupling. In nematic domain B, the decoupled region takes up 21% of the area.

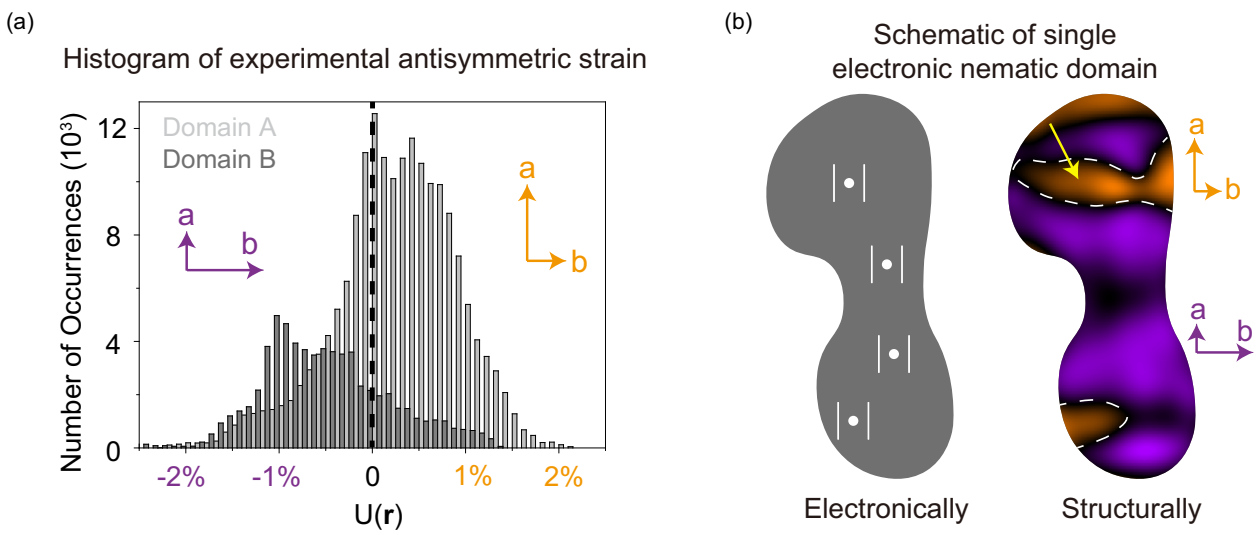

Figure 3.7.2: (a) Histogram of $U(\mathbf{r})$ in electronic nematic domains A and B. (b) Magnification of a single nematic domain B and the $U(\mathbf{r})$ map in it. White dots and double lines depict the Fe impurities and electronic stripes associated with the direction of electronic nematicity. Dashed lines highlight the borders between regions of positive and negative $U(\mathbf{r})$.

To understand the interplay of structural anisotropy and the electronic nematicity, we first note that, based on the resemblance between the experimental $U(\mathbf{r})$ map and the

simulated one (Fig. 3.5.4), by and large the landscape of the antisymmetric strain is the consequence of the dislocation network, which is a strain relief mechanism in the lattice mismatched epitaxial growth. Particularly, in the minor regions with the decoupling, $U(\mathbf{r})$ is caused by the dislocations. Second, the decoupling is the direct microscopic evidence that the nematicity is an electronic order instead of being secondary to the structural anisotropy. Previously, it has been macroscopically proved that nematicity is an electronic order by measuring the divergent nematic susceptibility, which is defined as $\mathrm{d}\psi/\mathrm{d}\epsilon$, where ψ is the resistivity anisotropy and ϵ is the strain [149]. Here, the decoupling directly suggests the electronic nematicity exists independently, instead of being subsidiary to the strain, because if it is, the strain of the opposite direction in those decoupled region would dictate the opposite nematicity.

In the following, we use a simple phenomenological model to show that the decoupling is a result of the (spatially) fast varying strain field, given that the electronic nematicity has its own order. We assume the electronic nematicity is described by a Ising order parameter field Ψ_i, where i denotes a single site assuming that the plane is represented by a 2D square grid of lattice sites. Each site has $\Psi_i = \pm 1$, where the plus (minus) sign represents the local nematicity oriented along a-axis (b-axis). To form the nematic order, we assume an nearest-neighbor Ising term $-\alpha \sum_{\langle i,j \rangle} \Psi_i \Psi_j$ where the coupling parameter $\alpha > 0$. The elasto-nematic coupling can be represented by a linear term $-\beta \sum_i U_i \Psi_i$ where $\beta > 0$ and U_i is the antisymmetric strain at site i (assuming $U_i = \pm 1$). So the total energy is

$$H = -\alpha \sum_{\langle i,j \rangle} \Psi_i \Psi_j - \beta \sum_i U_i \Psi_i \tag{3.13}$$

Note that here the strain field is determined by the dislocation network, therefore it is external. If U_i is constant over the whole plane, the ground state would simply be aligning Ψ_i with U_i at all sites. However, if the U_i field forms domains of 1 and -1, although within

the single domain it would be energetically favored to align Ψ_i with U_i, at the border of $U_i = 1$ and $U_i = -1$ domains, there is an energy cost due to the first term in Eq. 3.13 if Ψ_i is 1 on one side and -1 on the other side. If the size of the U_i domains are large, the border energy cost might be neglible compared to the energy gain from aligning Ψ_i with U_i within the area of the domain. However, if the U_i domains are small enough, the border energy will be comparable to the energy gain from aligning Ψ_i with U_i, or even could result in a negative net energy gain if Ψ_i is aligned with U_i everywhere. In this case, it might be energetically favorable to form some decoupling between Ψ_i and U_i so that there is no energy cost from the boundary between $\Psi_i = 1$ and $\Psi_i = -1$. Such an argument can be used to explain why there is decoupling in Fig. 3.7.2(b): the antisymmetric strain $U(\mathbf{r})$ changes sign in too small a lengthscale, and the energy gain from couple the electronic nematicity 100% with $U(\mathbf{r})$ cannot compensate for the energy cost from the electronic boundary energy along the white dashed lines.

3.8 Possible thickness-dependent structural modulations and the electronic nematic responses

In the previous sections we discussed a structural modulation network, accompanying which the electronic nematic patterns, that was observed at the surface of a four ML thick FeSe film. The results have been published in Ref. [22]. In this section and the next section, we show some additional results that have not been published yet as this thesis is being written.

We observe a distinct structural modulation network at the surface of a thicker FeSe film with an estimated thickness of 8 ML or larger. The difference between this modulation pattern and that observed at the surface of 4 ML FeSe film is two-fold. First, instead of orienting themselves along Fe-Fe lattice directions as in the latter case (Fig. 3.8.1(a)), the modulation lines (or dislocation lines) propogate along the Se-Se directions in the former case (Fig. 3.8.1(c)). Also, in the 8 ML case, every structural peak in the network is at a similar

height, in contrast to the 4 ML case where along each of the two orthogonal dislocation line directions, the height of every other peak is higher (Fig. 3.8.1(a) black arrows), while each structural peaks next to the higher ones are lower.

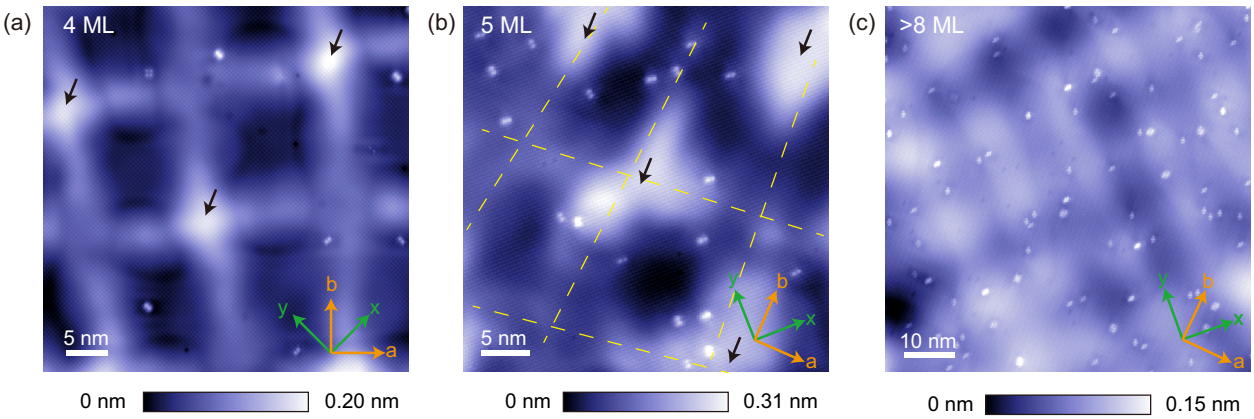

Figure 3.8.1: Structural modulation patterns as a function of thickness. STM topographs acquired at the surface of (a) 4 ML, (b) 5 ML and (c) >8 ML. a,b-axis denotes the Fe-Fe lattice directions while x,y-axis denotes the Se-Se directions.

Interestingly, at the surface of a 5 ML FeSe film, we observe a similar modulation pattern as 4 ML, i.e. an Fe-Fe oriented grid with higher/lower alternating grid nodes, but the higher nodes in the 5 ML case stand out more (Fig. 3.8.1(b)). The higher nodes form another grid that is 45° off the Fe-Fe oriented grid, and considering the fact that the Se-Se oriented grid (Fig. 3.8.1(c)) is also oriented in that direction, we speculate that, as the thickness increases, the higher nodes stand out more and more from the Fe-Fe grid, and eventually become the Se-Se grid.

We measure the average distance between the nearest-neighbor higher nodes in the Fe-Fe grids (Fig. 3.8.1 (a), (b) and (c); in the case of (c) Se-Se grid, this distance is the distance between the nearest-neighbor nodes) and plot it as a function of the thickness (Fig. 3.8.2(a)). We also fit the three data points based on the theoretical dislocation network spacing l as a function of the thickness h in the same plot using the following equation (the Matthews

model) (Fig. 3.8.2(a)) [150]:

$$l = \frac{b}{f - \frac{b}{8\pi h(1+\nu)}(\ln(\frac{h}{b}) + 1)} \tag{3.14}$$

where b is the Burgers vector in the Se-Se lattice and is the parameter to optimize here, while the other two parameters - the lattice mismatch between FeSe and $SrTiO_3(001)$ f and the Poisson ratio of FeSe ν - are fixed at 0.034 and 0.18 [151], respectively. The theoretical curve shows great consistency with the measured dislocation spacing and moreover, the fitted Burgers vector b is 0.367 nm, in agreement with the lattice constant of FeSe.

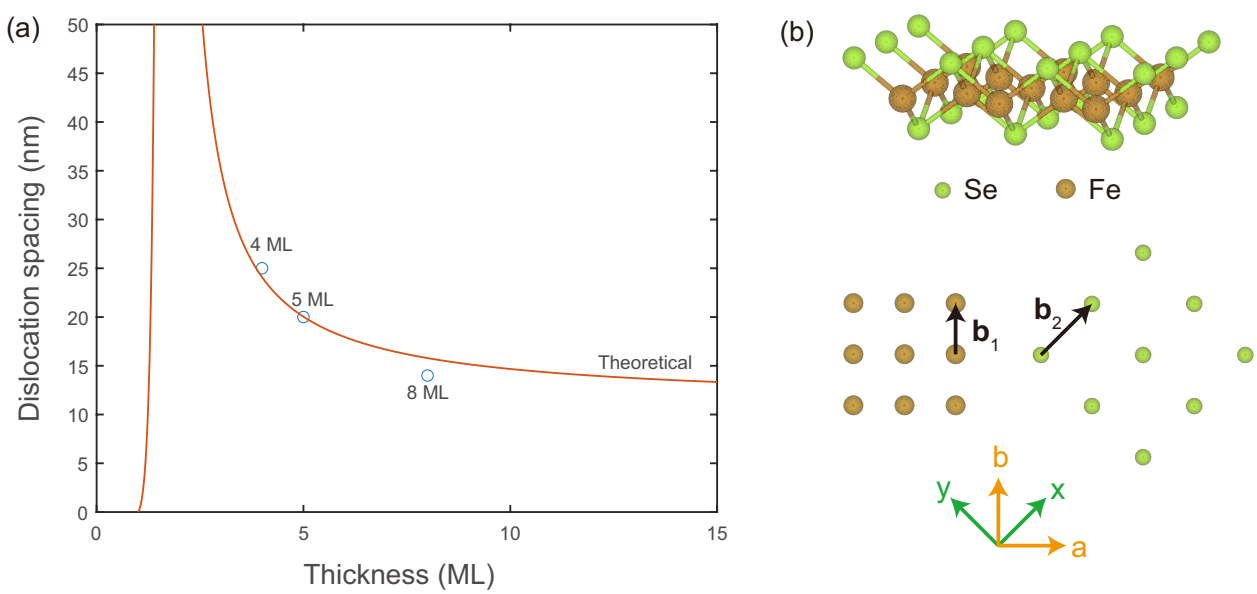

Figure 3.8.2: (a) Se-Se dislocation network spacing as a function of thickness. Blue circles are the average Se-Se dislocation spacing measured from Fig. 3.8.1(a-c) (see the text). Orange curve is the fit based on the Matthews model. (b) Schematic of the two Burgers vectors assumption. Top is the monolayer FeSe sandwich structure, where green circles stand for the Se atoms and brown circles are Fe atoms. Bottom indicates the two Burgers vectors $\mathbf{b}_1$ and $\mathbf{b}_2$.

The consistency of the measured Se-Se dislocation spacing as a function of film thickness

with the Matthews model supports our speculation that the higher nodes in the Fe-Fe dislocation network in the thinner films evolve into the Se-Se dislocation network in the thicker films. To understand the mechanism behind the dislocation network evolution as a function of the thickness, we propose a "two Burgers vectors" assumption. There are two dislocation orientations/networks, namely the Fe-Fe networks manifested in 4 ML and 5 ML as well as the Se-Se networks manifested in >8 ML and also as the higher nodes in 4/5 ML. The characteristic Burgers vectors of these two dislocation networks are $\mathbf{b}_1$ and $\mathbf{b}_2$, respectively (Fig. 3.8.2(b)), corresponding to the lattice constant of the "Fe lattice" and the "Se lattice" where the latter is the real lattice constant of FeSe. The relationship between $\mathbf{b}_1$ and $\mathbf{b}_2$ is in agreement with the relationship between the Fe-Fe network and the Se-Se network (or in 4 ML, the higher nodes) in 4 ML (Fig. 3.8.1(a)), i.e. $\mathbf{b}_2$ can be obtained by rotating $\mathbf{b}_1$ by 45° and multiplying it by a factor of $\sqrt{2}$.

The self-energy per unit length of an edge dislocation line reads [136]

$$E = \frac{Gb^2}{4\pi(1-\nu)}\ln(\frac{\alpha R}{b}) \tag{3.15}$$

where G, ν and α are elastic constants, R is the distance from the dislocation line and b is the Burgers vector. This equation favors a smaller Burgers vector to minimize the energy. Therefore, the shorter Burgers vector, $\mathbf{b}_1$, of the "Fe lattice" is favored. However, $\mathbf{b}_1$ is not the real periodic unit of the lattice but the Se-Se lattice vector, which is $\mathbf{b}_2$, is. We hypothesize that, when the thickness is small enough, although $\mathbf{b}_1$ is not a legit Burgers vector, because of the less self-energy of dislocations defined by $\mathbf{b}_1$ and the "Fe lattice" being a "quasi periodic lattice", it is favored to form the $\mathbf{b}_1$ dislocations instead of the $\mathbf{b}_2$ dislocations. However, when the thickness is greater than a threshold, which is 5 ML as observed in 3.8.1, the Burgers vector has to be the real periodic unit of the lattice, so there can only be the $\mathbf{b}_2$ dislocations.

A distinct landscape of electronic nematic domains is observed on the surface of thicker

films, as shown in Fig. 3.8.3. Due to the Se-Se oriented dislocation lines, the pre-existing strain is along Se-Se instead of Fe-Fe, therefore has much less impact in the fragmentation of the electronic nematic domains. A much higher correlation of the $U(\mathbf{r})$ calculated along Fe-Fe directions and the electronic domains is observed. The domains are "maze-like" in this case [146].

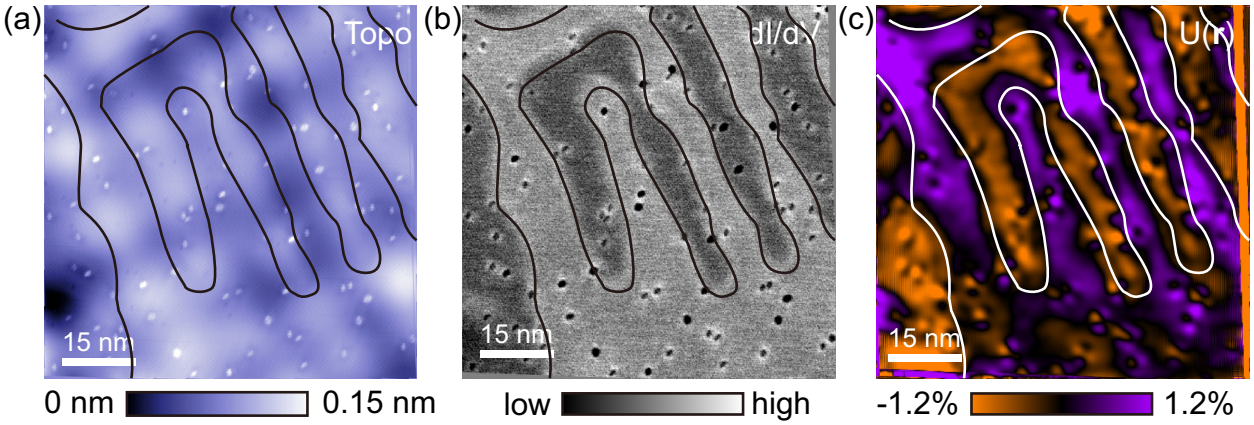

Figure 3.8.3: The "checkerboard" dislocation pattern in the 8ML case and the resulting $U(\mathbf{r})$ map and electronic nematic domains. The contours outline the electronic nematic domains.

Interestingly, Fig. 3.8.3(b) exhibits a intensity contrast between the electronic nematic domain A and B. In fact, such contrast is bias dependent (Fig. 3.8.4): from 0 mV to 40 mV, there is no contrast; around 80-100 mV, the contrast between domain A and B is negative and reaches the maximum; from 120 mV to 140 mV, the contrast is positive and peaks at 140 mV, although further investigation above 140 mV is desired. The energy difference between the maximal negative contrast and the maximal positive contrast is ∼50 meV, consistent with the energy scale of d_{xz} d_{yz} orbital splitting in FeSe [114]. We hypothesize the tip is more sensitve to one of the d_{xz} and d_{yz} orbitals than to the other at certain biases [152]. We have observed similar nematic contrast in other FeSe/$SrTiO_3$ samples. Further more careful investigation is needed.

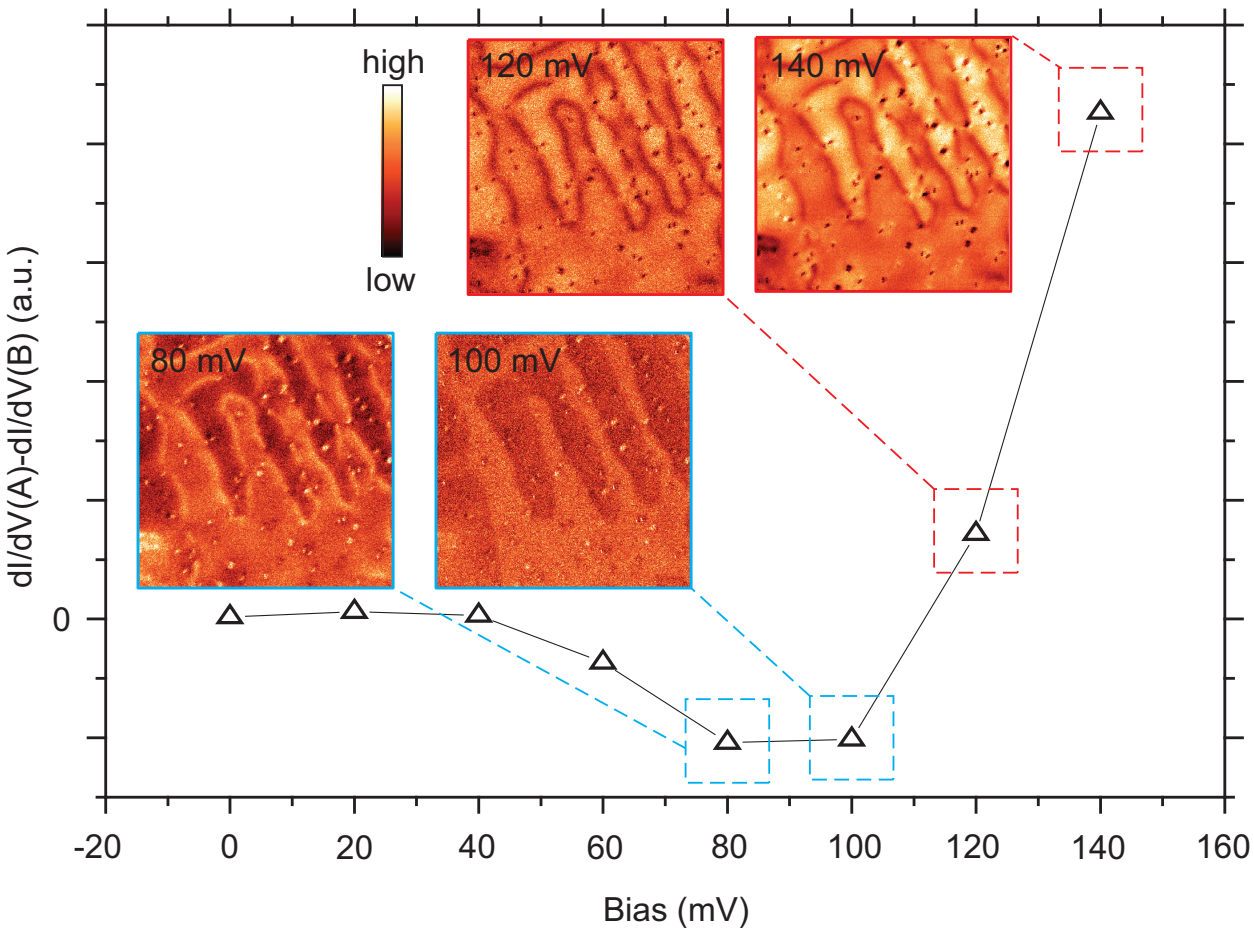

Figure 3.8.4: Nematic contrast in dI/dV maps.

3.9 Preliminary results on temperature and magnetic field dependence of nematicity

Investigation of nematicity in Fe-based superconductors as a function of temperature is of great importance for a couple of reasons. First, due to the complex interplays of the nematic phase, the magnetic phase and also the superconducting phase, it is crucial to identify the transition temperatures of each phase in order to reveal the relationship between the nematic order, magnetic order and superconductivity [36]. Secondly, it is also interesting to explore the interplay of the electronic nematicity and structural distortion above the nematic critical

temperature, which provides the information of nematic susceptibility [110, 149, 153, 154].

The interplay between nematicity and magnetism is also an intriguing topic, especially in the case of FeSe, where the nematic phase is not followed by a long range magnetic order as the temperature is cooled down [155]. This is in contrast to the iron pnictides, where typically there is an antiferromagnetic order upon cooling down from the nematic phase [36]. There is ongoing debate on the origin of nematicity in iron-based superconductors, whether it is a spin order or charge/orbital order [36, 156]. Investigation into the magnetic field dependence of the electronic nematicity in our FeSe thin films may shed light on this question.

Fig. 3.9.1 shows the STM topographs of the same 50×50 nm region acquired at 5 K, 10 K, 20 K and 30 K. The $U(\mathbf{r})$ maps are calculated from each of the topographs and do not exhibit significant differences. The electronic nematic domains display a good correlation with $U(\mathbf{r})$ at 5 K as shown in Fig. 3.9.1(j). We were not able to acquire a high quality $\mathrm{d}I/\mathrm{d}V$ map at 30 K.

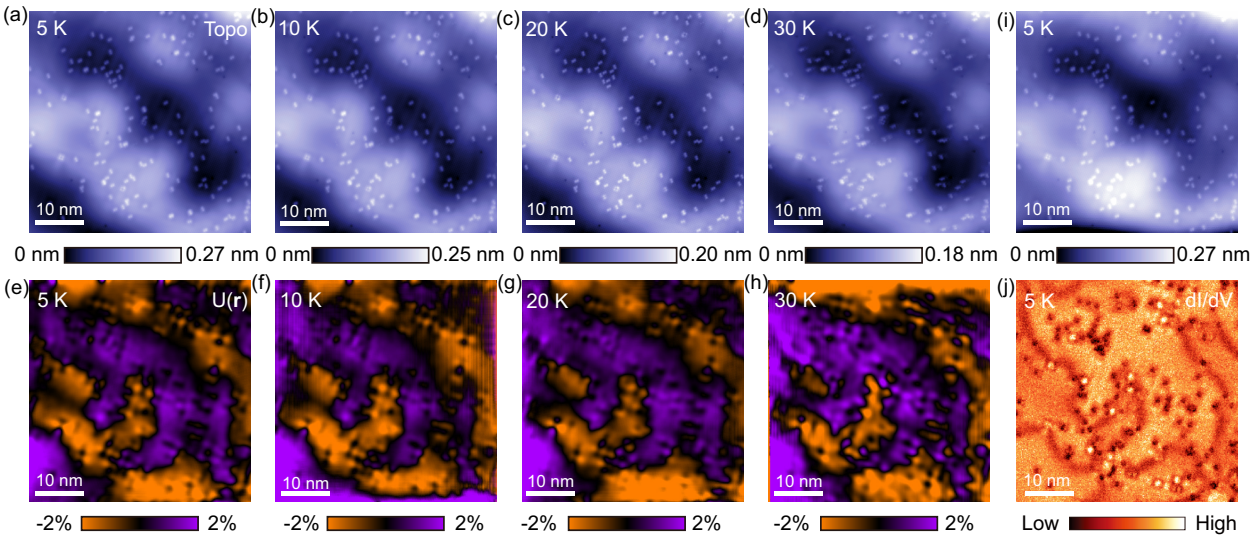

Figure 3.9.1: Temperature dependence of $U(\mathbf{r})$ and the electronic nematicity. (a)-(d) STM topographs acquired at 5-30 K. (e)-(h) Corresponding $U(\mathbf{r})$ derived from (a)-(d). (j) $\mathrm{d}I/\mathrm{d}V$ map aquired at 5 K. All maps have been drift-corrected to align with each other.

Fig. 3.9.2 shows the magnetic field dependence of the topograph, $U(\mathbf{r})$ and $\mathrm{d}I/\mathrm{d}V$ map acquired on the same region as an 8 T field is applied parallel to the c-axis. We do not observe significant differences between the maps acquired in zero field and in an 8 T out-of-plane field.

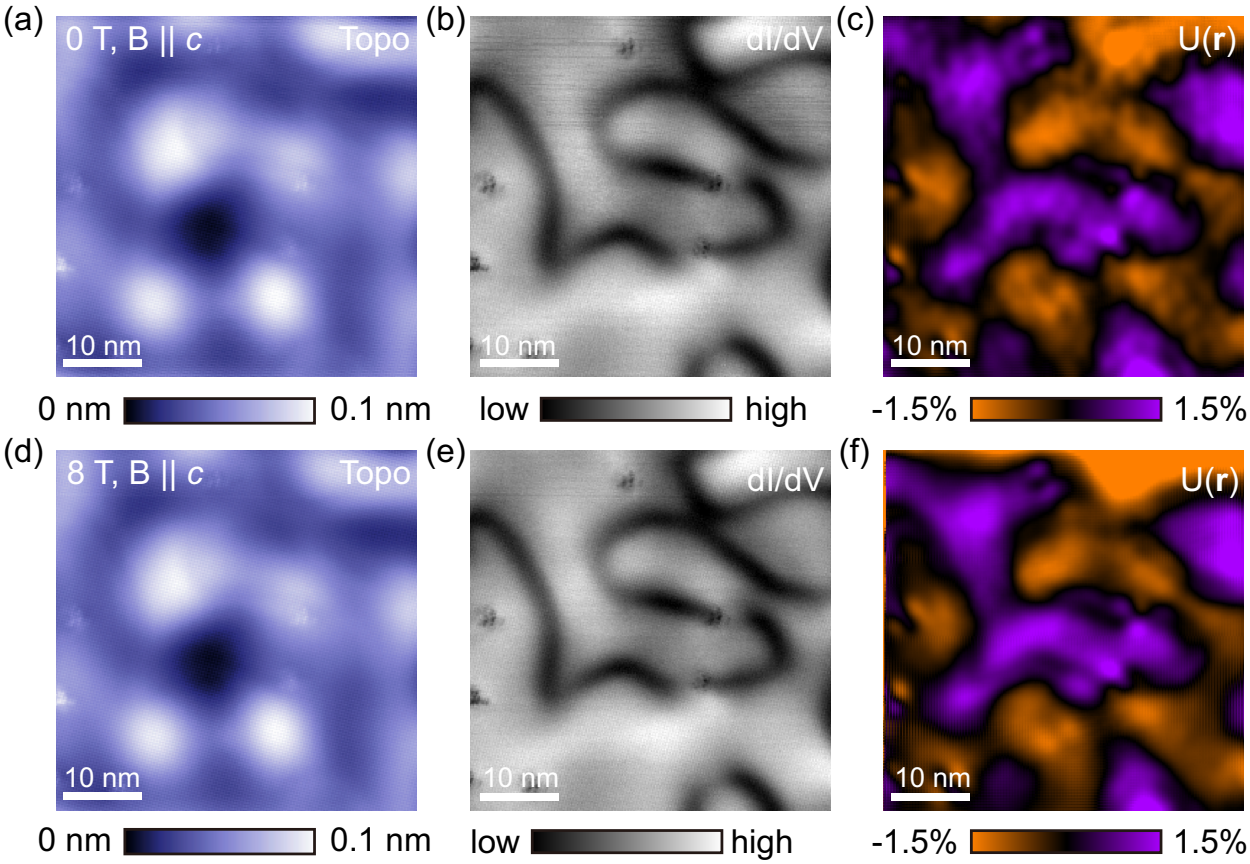

Figure 3.9.2: Out-of-plane magnetic field dependence of $U(\mathbf{r})$ and the electronic nematicity. (a)-(c) STM topograph, $U(\mathbf{r})$ and $\mathrm{d}I/\mathrm{d}V$ map acquired at 5 K in zero field. (d)-(f) STM topograph, $U(\mathbf{r})$ and $\mathrm{d}I/\mathrm{d}V$ map acquired at 5 K in an 8 T field parallel to the c-axis.

Knowing that an out-of-plane field up to 8 T would not caused significant change, we mounted the sample on a 20° slanted STM sample holder and applied an 8 T field along the tip direction. This is equivalent to a 2.74 T in-plane field and a 7.52 T out-of-plane field. Fig. 3.9.3 shows the magnetic field dependence of the topograph, $U(\mathbf{r})$ and $\mathrm{d}I/\mathrm{d}V$ map acquired

on the same region as such a magnetic field is applied. Still, the difference between the top row and the bottom row is insignificant.

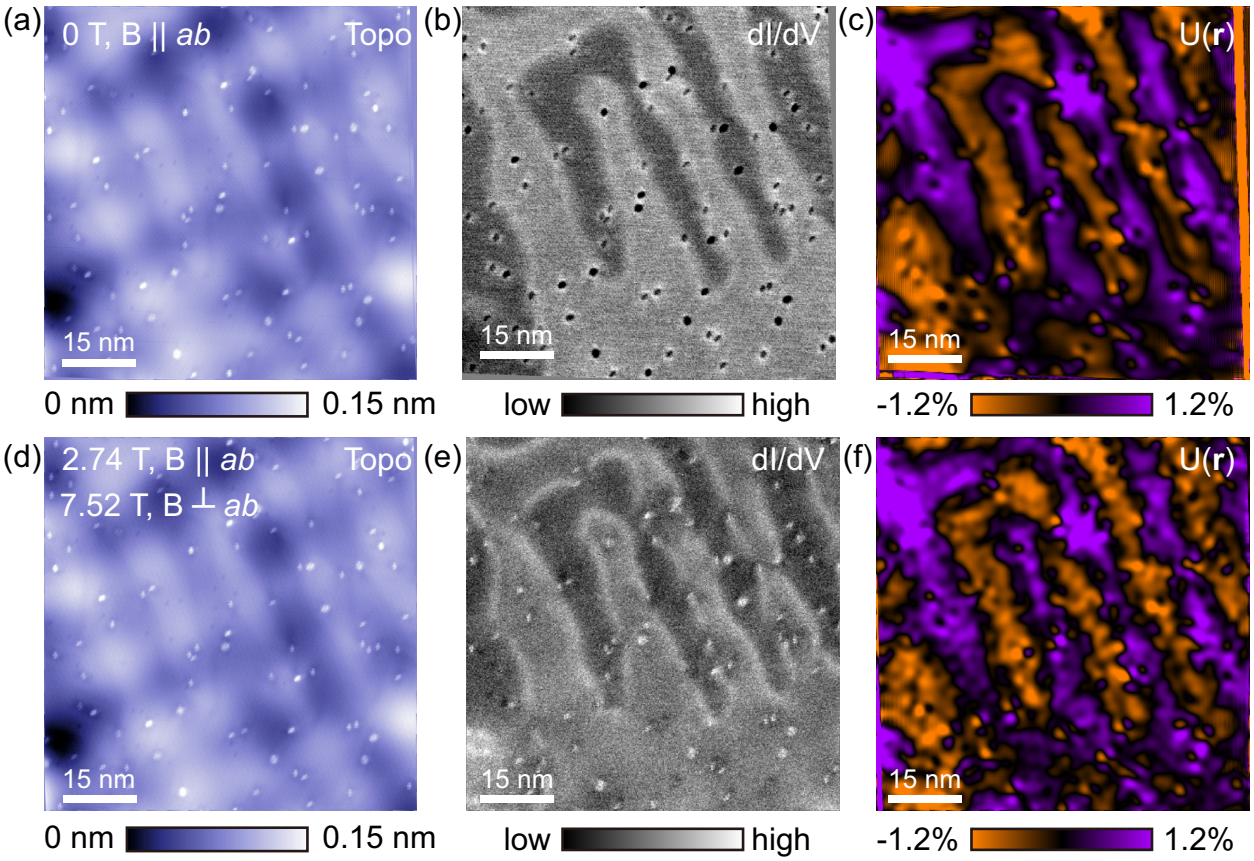

Figure 3.9.3: In-plane magnetic field dependence of $U(\mathbf{r})$ and the electronic nematicity. (a)-(c) STM topograph, $U(\mathbf{r})$ and $\mathrm{d}I/\mathrm{d}V$ map acquired at 5 K in zero field. (d)-(f) STM topograph, $U(\mathbf{r})$ and $\mathrm{d}I/\mathrm{d}V$ map acquired at 5 K in a 2.74 T field parallel to the ab-plane and a 7.52 T field perpendicular to the plane.

We note that the temperatures that we explored here are still well below the nematic critical temperature [146] and the magnetic field we applied might be too small. Further experiments at higher temperatures and in larger magnetic fields are desired.

3.10 Conclusion

We synthesize FeSe thin films of thickness of a monolayer to ∼8 monolayers on the $SrTiO_3$ substrates. A network of dislocation lines is observed when the thickness is greater than 2 ML, and such network shows a thickness-dependence. Modulation of the FeSe lattice, as a result of the dislocation networks, was extracted quantitatively, and is found to be remarkably consistent with theoretical results. The interplay of the lattice modulation and the distribution of the nematic domains is analyzed.

Chapter 4

Doping a topological insulator thin film with magnetic atoms

4.1 Introduction

As discussed in the Introduction Chapter, the ancestor of the topogical materials nowadays is the integer quantum Hall effect discovered back in the 1980's [49] and subsequently explained by the famous TKNN paper [54]. In 1988, Haldane [55] proposed another version of the quantum Hall system where the time-reversal symmetry is broken by a complex staggered magnetic flux pattern where the net flux is zero on a honeycomb lattice. This is the earliest proposal of a quantum anomolous Hall effect, i.e. an external magnetic field is not required to achieve quantized Hall conductance. However, such a model is challenging to be experimentally realized. Years later, with the proposal and realization of the topological insulators that preserve time-reversal symmtry [61, 157–159], it was theoretically proposed and experimentally realized that by introducing long-range magnetic order in a topological insulator, the time-reversal symmetry is broken and an exchange gap is opened in the surface Dirac cone [160, 161]. Futhermore, chiral edge states and quantized Hall conductance can be realized if Fermi energy is tuned into the exchange gap [160, 162]. Such quantum anomolous Hall systems have been realized in magentically doped topological insulator thin films [100], thin flakes of intrinsic magnetic topological insulators [163] and also moire graphene systems [164].

In this chapter, I will introduce our effort in doping the magnetic Fe atoms in the topogical insulator Bi_2Se_3 thin films using MBE. Synthesis method will be described in detai firstl, and then I will discuss how we characterize the synthesized Fe: Bi_2Se_3 thin films.

4.2 Synthesis of Fe-doped Bi_2Se_3 thin films

Fe-doped Bi_2Se_3 (Fe: Bi_2Se_3) thin films were grown on Nb-doped (0.05 wt%) $SrTiO_3$(001) (Shinkosha STEP) substrates. The substrates were sonicated in acetone and 2-propanol for 10 min each, dried in N_2 gas and subsequently inserted into our MBE system (Fermion Instruments) with a base pressure of $\sim 4 \times 10^{-10}$ Torr. We first co-evaporated Bi and Se to form a Bi_2Se_3 buffer layer, then co-evaporated Fe, Bi and Se to grow the Fe: Bi_2Se_3 films. The Bi_2Se_3 buffer layer was adopted to bridge the substrate and Fe-doped layers, as the latter was found harder to be directly grown layer-by-layer on the substrates. Reflection high-energy electron diffraction (RHEED) was used to monitor the growths. During the growth, the substrates were kept at ∼230 °C monitored by a pyrometer. Fe (99%), Bi (99.999%) and Se (99.999%) were stabilized in three Knudsen cells at 1030 °C, 493 °C and 145 °C, respectively. Nominally it takes ∼20 minutes to grow 1 quintuple layer (QL) of Bi_2Se_3 as calculated from the QCM flux rates. The sample shown in the results section has 8 QL of Bi_2Se_3 as the buffer layer and 9.5 QL of Fe: Bi_2Se_3 on top of that. The sample was post-annealed for 13 hours at the growth temperature, then quickly cooled them down to room temperature and used vacuum suitcase chamber to transfer them to the STM.

4.3 Characterization

We start with examining the quality of the thin film. As a van der Waals layered material, Bi_2Se_3 can be relatively handily grown on various substrates, such as Al_2O_3, $SrTiO_3$(111), Si(111) and graphene terminated 6H-SiC(0001) [165–173]. Here we use $SrTiO_3$(001) as the substrate. Despite the fact that the substrate surface has a square lattice in contrast to the hexagonal lattice of Bi_2Se_3, the quality of the growth judged by the streaky RHEED pattern of the Bi_2Se_3 buffer layer is surprisingly good Fig. 4.3.1(a). We note that there are two sets of streak pattern indicated by the yellow and blue arrows. The spacing of the latter

is $\sqrt{3}$ times of the former. They correspond to two twin domains of Bi_2Se_3, one rotated by 30° from the other. Unlike the growths on hexagonal substrates, the formation of twin domain cannot be eliminated when grown on a square lattice as in our case. Practically we discovered that the 2D growth of Fe: Bi2Se3 was much more easily achieved on a Bi2Se3 buffer layer than directly grown on $SrTiO_3$ (001) substrate. However, the Fe dopants induce disorder into the growths, i.e. the growths of Fe: Bi_2Se_3 can no longer maintain perfectly 2D (Fig. 4.3.1(a) bottom).

A closer look at the quality of the Fe: Bi_2Se_3 films is achieved with the STM topographs. Consistent with the overall streaky with a few dotty features RHEED pattern, the large field-of-view (FOV) topograph of Fe: Bi_2Se_3 show clean and mostly flat landscape with triangular-like steps formed by dislocation disorders (Fig. 4.3.1(b)). The step height is ∼1 nm. As we zoom in to a 40 nm by 40 nm FOV, we observe a considerable amount of dark impurities with a uniform density distribution (Fig. 4.3.1(c)). We proceed to identify these impurities in a smaller FOV atomically resolved STM topograph (Fig. 4.3.1(d)). The bright lattice sites are the topmost Se sites in a quintuple layer (QL) of Bi_2Se_3. Within each of the dark impurity, the center is a bright spot, and the position of that is at the center of the triangle formed by three nearest topmost Se sites. By analyzing the lattice structure of Bi_2Se_3, we conclude that the dark impurities are positioned at the Bi atoms closer to the topmost Se layer, as indicated by the purple lattice plane (Fig. 4.3.1(e)).

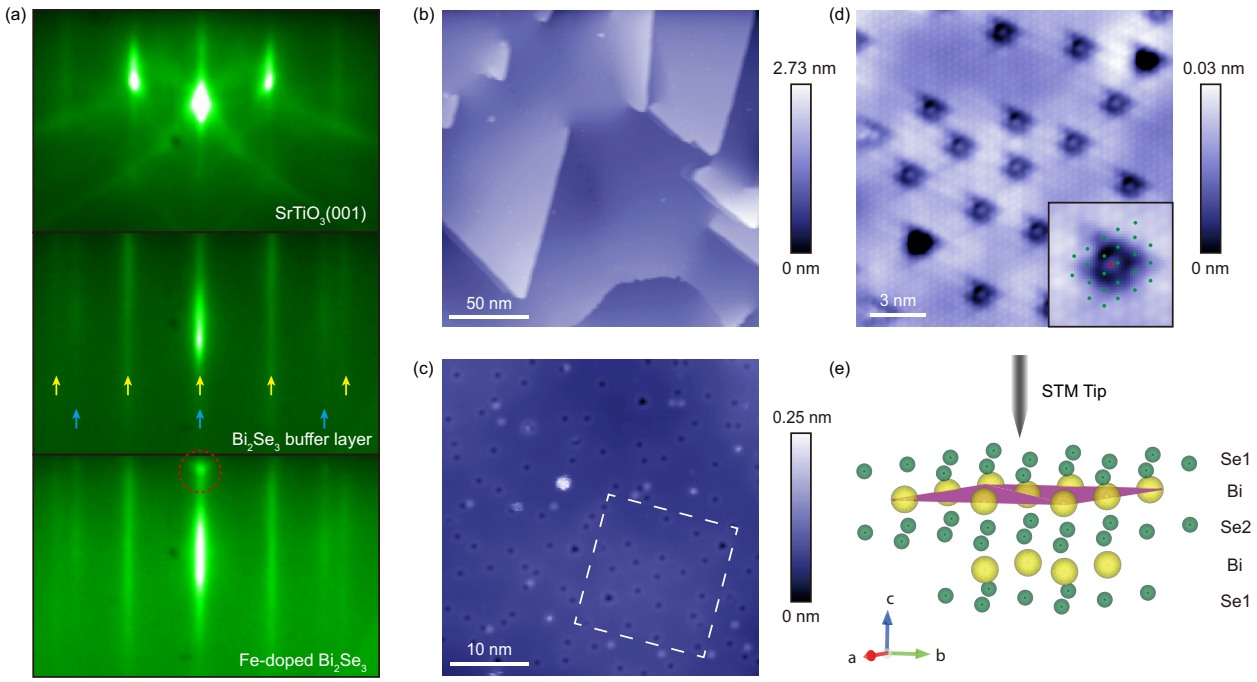

Figure 4.3.1: (a) RHEED images of the substrate, the Bi_2Se_3 buffer layer and the Fe-doped Bi_2Se_3 layers. The yellow and blue arrows denote two sets of RHEED pattern (see text). The dashed red circle outlines the sign of 3D growth. (b) Large-scale STM topograph. (c) STM topograph showing the impurities. (d) Magnification of the region outlined by the dashed white box in (c). Inset shows the lattice schematic superimposed on the topograph. (e) Schematic of the crystal structure. The pink plane indicates the locations of the Fe substitution.

The impurities most likely are Fe substitutions of Bi^{3+} as Fe^{3+} due to the uniform density and the sizable amount of them. To quantify the doping ratio of Fe from the density of the impurities, we count the number of the impurities in Fig. 4.3.1(c), calculate the number of Bi_2Se_3 unit cells from the area of the FOV, and then find out the doping ratio. Hence the doping ratio of Fe:Bi calculated from the STM topograph is ~1%. Here we assume there is no gradient of Fe density along the thickness of the film, i.e. each QL has the same amount of Fe impurities as the topmost QL. The doping ratio calculated here is in drastic difference

from the Fe doping ratio calculated from the flux rates of Fe and Bi measured by QCM, which is ∼22.5%. The huge difference in the doping ratio is beyond the error of measurements, inferring possible inhomogeneity of the Fe dopants. The hidden Fe dopants may reside as intercalations, in twin domain boundaries or form clusters, or there could be a gradient of Fe density along the thickness (or as an extreme case most of Fe atoms hide at the interface between the thin film and substrate).

We then investigate the electronic properties of the same region of Fe:Bi_2Se_3 as in Fig. 4.3.1(d) by acquiring dI/dV(**r**, V) maps over an energy range of hundreds of meV (where I is the tunneling current, V is the bias voltage applied to the sample) on a densely-spaced pixel grid. Quasiparticle interference (QPI) wave pattern is clearly observed (Fig. 4.3.2(a)-(f)). By Fourier transforming the dI/dV maps, we observe two QPI dispersing modes along Γ-M directions (Fig. 4.3.2(g)) between 0.30 to 0.45 $Å^{-1}$ and the energies range from 200 to 350 meV and from 350 to 500 meV, respectively, resulting in a q-dispersion velocity of ∼1 VÅ. We note that similar QPI modes have been reported in bulk Fe: Bi_2Se_3 [174], where q ranges from 0.2 to 0.35 $Å^{-1}$ and energies generally shifted up from our data and also a smaller q-dispersion velocity. These differences could be the consequences of the different Fe doping ratio and the different thickness of our sample from theirs. Despite the differences, the close resemblance of our data and Ref. [174] is another evidence of the quality of the sample.

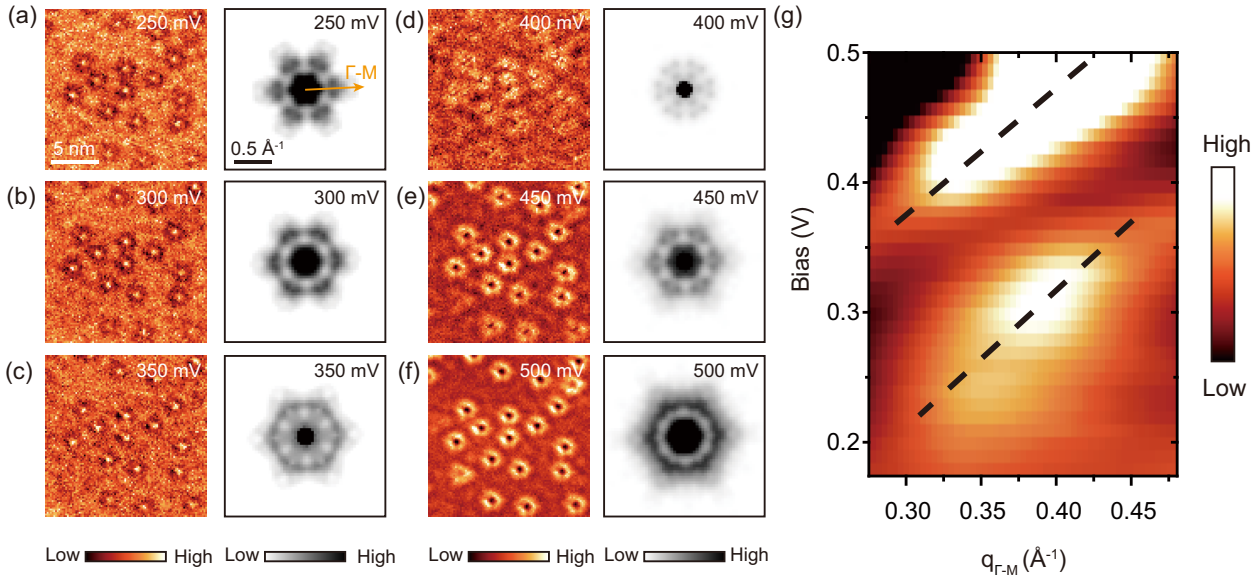

Figure 4.3.2: QPI electronic properties of Fe:Bi_2Se_3 thin film. (a)-(f) dI/dV maps (left) and their FTs (right) at six biases from 250 mV to 500 mV. The FTs have been six-fold symmetrized for a greater signal-to-noise. (g) FT linecut along the Γ-M direction denoted in (a). Dashed lines serve as guide to the eye for the dispersions.

We proceed to characterize the magnetic properties of the sample by conducting magnetic field sweep measurements. A hysteresis loop is observed with a coercive field of ∼25 Oe (Fig. 4.3.3(b)). Subtracting the diamagnetic part of the signal which is ascribed to Bi_2Se_3 and the substrate, we extract the saturation magnetization as 6.8×10^{-6} emu. The average magnetization of one Fe^{3+} ion is calculated to be 1.02 μ_B using the number of Fe atoms calculated from the flux rate of Fe calibrated by QCM and the growth time. There are possibly three spin configurations of Fe^{3+} d^5 orbital in which the total spin S are 5/2, 3/2 and 1/2, and the corresponding magnetic moments are 5.92 μ_B, 3.88 μ_B and 1.73 μ_B, respectively. The extracted average magnetization per Fe^{3+} is lower but close to these values. The reason for the lower magnetization could be impurity phases, such as Fe_7Se_8, where the average magnetization per Fe is only 0.25 μ_B (ref). The magnetization results agree with

the nominal Fe doping ratio calculated from the flux rates calibrated using QCM.

To further support our argument that the observed Fe doping ratio in STM topographs is drastically lower than the nominal one, we use energy-dispersive X-ray spectroscopy (EDX) to directly analyze the composition of the samples (Fig. 4.3.3(a)). For a better signal-to-noise of the Fe:Bi_2Se_3 layers, we choose a ∼69 QL Fe:Bi_2Se_3 sample with the same growth conditions as the sample shown in Fig. 4.3.1 and Fig. 4.3.2. n_{Fe} : (n_{Fe}+n_{Bi}) was found to be ∼24.8%, in consistency with the ratio calculated using QCM calibrated flux rates.

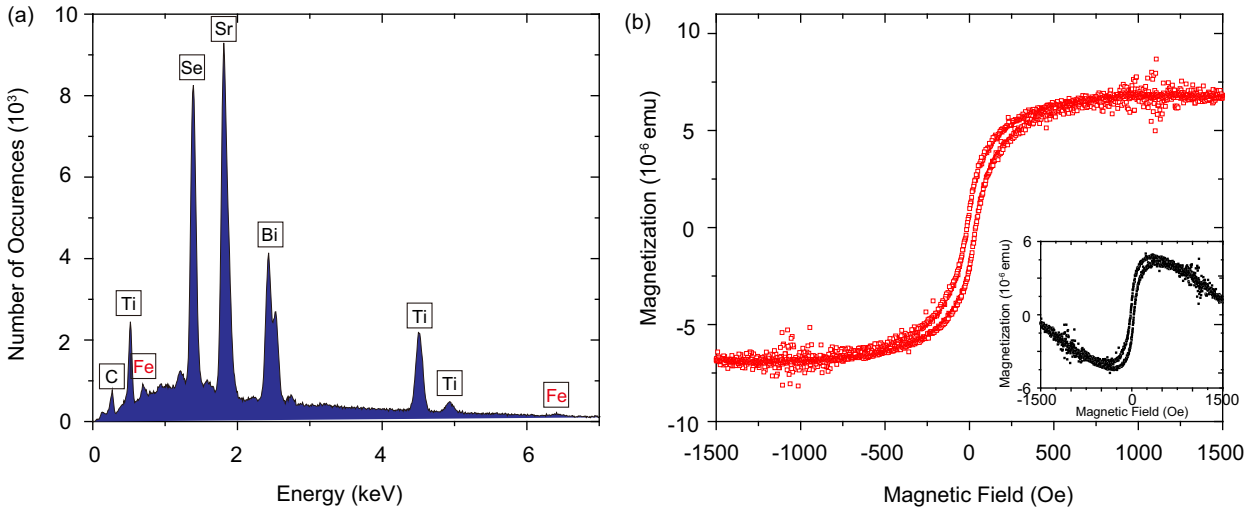

Figure 4.3.3: (a) EDX characterization of the ∼69 QL Fe:Bi_2Se_3 thin film. (b) Magnetization as a function of the in-plane magnetic field. The inset (black) shows the data with the DM signal from the substrate and Bi_2Se_3. The red curve was calculated by subtracting the DM signal, which was obtained by fitting the 1000-1500 Oe portion of the raw data.

4.4 Conclusion

We grow Fe:Bi_2Se_3 thin films on $SrTiO_3$ (001) substrates and discover that the Fe doping ratio calculated from STM topographs is ∼20 times lower than the nominal doping ratio, which is cross-checked by QCM flux ratio, EDX composition analyses and magnetic sweep

measurements. We conclude that there is possible Fe inhomogeneity in the possible forms of clustering, intercalation, density gradient or impurity phases.

Chapter 5

Kagome thin films Fe_xSn_y: a playground for correlated states and band topology

5.1 Introduction

A kagome lattice is a 2-dimensional corner-sharing triangular lattice (Fig. 5.1.1). It has three sublattices A, B and C, as shown in the figure. A simple tight binding calculation involving only the nearest-neighbor hopping terms would yield an interesting bandstructure [175–178]. Here I briefly derive it as follows.

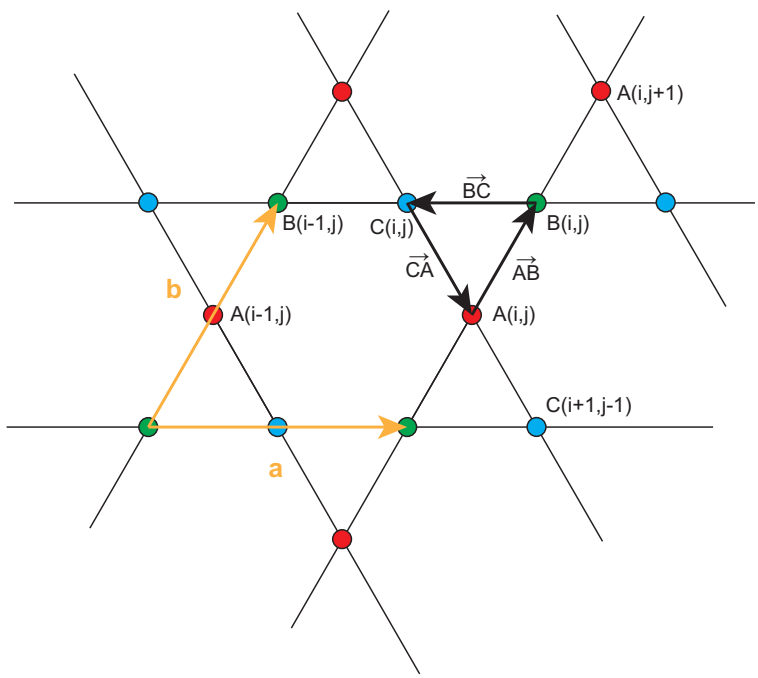

Figure 5.1.1: Kagome lattice structure and a simple tight binding calculation.

As shown in Fig. 5.1.1, there are sublattices A, B and C, and the real space labels (i,j) are shown in the figure. The basis vectors are $\mathbf{a} = \hat{x}$ and $\mathbf{b} = \hat{x}/2 + \sqrt{3}\hat{y}/2$ assuming lattice constant is 1. We use $A^\dagger$ and A to denote the real space creation and annihilation operators

on site A (same for B and C). The Hamiltonian is

$$H = \sum_{ij}(B_{ij}^{\dagger}A_{ij} + C_{ij}^{\dagger}B_{ij} + A_{ij}^{\dagger}C_{ij} + C_{i+1,j-1}^{\dagger}A_{ij} + A_{i,j+1}^{\dagger}B_{ij} + B_{i-1,j}^{\dagger}C_{ij} + H.c.) \quad (5.1)$$

Plug in

$$A_{ij} = \frac{1}{\sqrt{N}}\sum_{\mathbf{k}} e^{-i\mathbf{k}\cdot\mathbf{A}_{ij}}\tilde{A}_{\mathbf{k}} \quad (5.2)$$

and the similar Fourier transforms for B and C sites (here $\mathbf{A}_{ij}$ means the position vector of site A(i,j)), we can convert the first term into

$$\begin{aligned}\sum_{ij} B_{ij}^{\dagger}A_{ij} &= \frac{1}{N}\sum_{ij}\sum_{\mathbf{k}} e^{i\mathbf{k}\cdot(\mathbf{A}_{ij}+\overrightarrow{AB})}\tilde{B}_{\mathbf{k}}^{\dagger}\sum_{\mathbf{k}'} e^{-i\mathbf{k}'\cdot\mathbf{A}_{ij}}\tilde{A}_{\mathbf{k}'} \\ &= \sum_{\mathbf{k}} e^{i\mathbf{k}\cdot\overrightarrow{AB}}\tilde{B}_{\mathbf{k}}^{\dagger}\tilde{A}_{\mathbf{k}}\end{aligned} \quad (5.3)$$

Here the vector $\overrightarrow{AB}$ is defined as in Fig. 5.1.1. Similarly, we can convert every term in Eq. 5.1 to k-space, and the resulting Hamiltonian is

$$H_{\mathbf{k}} = \begin{pmatrix}\tilde{A}_{\mathbf{k}}^{\dagger} & \tilde{B}_{\mathbf{k}}^{\dagger} & \tilde{C}_{\mathbf{k}}^{\dagger}\end{pmatrix}\begin{pmatrix} 0 & 2\cos(\mathbf{k}\cdot\overrightarrow{AB}) & 2\cos(\mathbf{k}\cdot\overrightarrow{CA}) \\ 2\cos(\mathbf{k}\cdot\overrightarrow{AB}) & 0 & 2\cos(\mathbf{k}\cdot\overrightarrow{BC}) \\ 2\cos(\mathbf{k}\cdot\overrightarrow{CA}) & 2\cos(\mathbf{k}\cdot\overrightarrow{BC}) & 0\end{pmatrix}\begin{pmatrix}\tilde{A}_{\mathbf{k}} \\ \tilde{B}_{\mathbf{k}} \\ \tilde{C}_{\mathbf{k}}\end{pmatrix} \quad (5.4)$$

By diagonalizing this Hamiltonian, we can calculate the energy eigenvalues as follows:

$$\begin{aligned}E_1(\mathbf{k}) &= -2 \\ E_{2,3}(\mathbf{k}) &= 1 \pm \sqrt{2(\cos k_x + \cos(\frac{k_x+\sqrt{3}k_y}{2}) + \cos(\frac{k_x-\sqrt{3}k_y}{2})) + 3}\end{aligned} \quad (5.5)$$

We plot this band structure in Fig. 5.1.2. From the band structure, one can find three interesting features. Firstly, there is a dispersionless band, or "flat band", throughout the

entire Brillouin zone. The vanishing kinetic energy is dominated by the electron-electron correlation and there can potentially be exotic phenomena, such as unconventional superconductivity and magnetism, if the Fermi level is near the flat band [18, 179, 180]. Secondly, there are the saddle points, namely the van Hove singularities, at the M points. The large electronic density of states at these high symmetry points would potentially favor charge density waves and/or other electronic phases, which has recently been experimentally found in the AV_3Sb_5 (A=Cs, K, Rb) kagome materials [181–192]. Thirdly, there are Dirac points located at the K and K' points of the Brillouin zone [192–195].

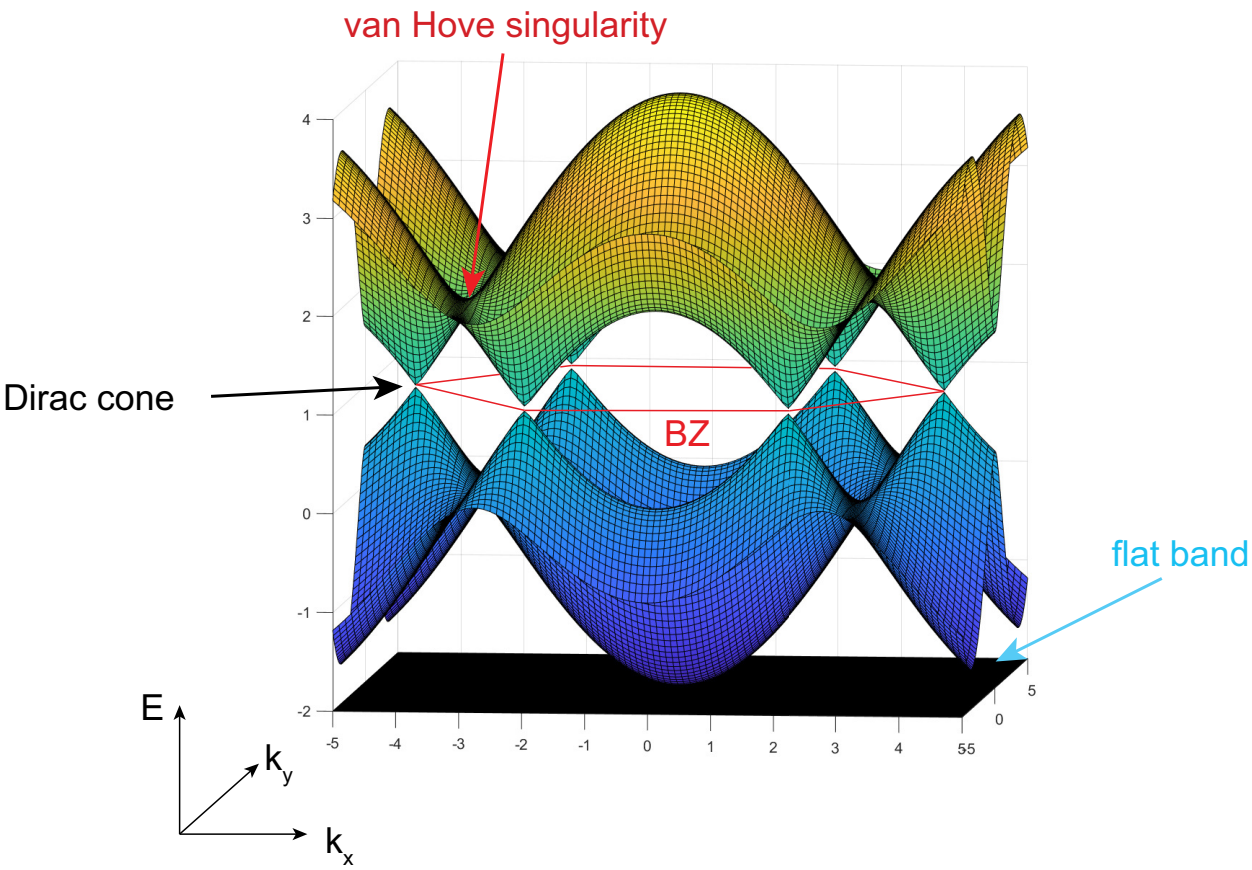

Figure 5.1.2: Kagome band structure derived from the simplest tight-binding model.

If spin-orbit coupling and/or ferromagnetic ordering are included in the Hamiltonian, gap openings can occur at both the quadratic touching point at Γ and also the linear Dirac

touching at K/K' [175]. The Dirac gap opening can lead to topological insulator phase or Chern insulator phase [177, 196, 197]. The flat band can also acquire a nonzero Chern number and also have finite band width, and it may favor the fractional Chern insulator phase (fractional quantum Hall state) [175, 198].

In this chapter, I will first discuss the selective MBE synthesis of the kagome magnet thin films FeSn and Fe_3Sn_2 [80, 199]. I will then discuss the STM/S results on Fe_3Sn_2 and a possible interpretation of the data [80].

5.2 Selective MBE synthesis of kagome magnet thin films FeSn and Fe_3Sn_2

Quantum solids composed of atoms arranged on a kagome lattice are a versatile platform to explore new electronic phenomena at the intersection of band topology and electronic correlations [175, 177, 178, 200–205]. While the initial excitement behind these systems stemmed from the possibility of realizing spin liquid phases [200, 206], recent experiments revealed a range of other novel electronic phases that can emerge on a kagome lattice in the presence of spin-orbit coupling, non-trivial Berry curvature and/or magnetism. These for example include topological flat band [195, 207], Chern magnet phase [197], Weyl semimetal phase and Fermi arcs [75], and various charge density waves [181–192].

In the pursuit of these exotic phenomena, family of Fe_xSn_y kagome magnets has been of particular interest [193, 194, 208–213]. They are characterized by a relatively simple crystal structure (Fig. 5.2.1a-c) and magnetic ordering that can be tuned by the Fe:Sn composition ratio and temperature [214–216]. Two distinct crystal structures – FeSn (antiferromagnetic with Neel temperature T_N ~370 K [215]) and Fe_3Sn_2 (ferromagnetic with Curie temperature T_c ~640-660 K [208, 214, 216]) – have emerged as model members of this family of kagome magnets. The two compounds exhibit prototypical kagome lattice electronic structure consisting of Dirac fermions at the Brillouin zone boundary and dispersionless flat bands

[193, 194, 209]. Fe_3Sn_2 also exhibits anomalous Hall response [194, 208] and a surprising magnetic field induced electronic nematic response [210]. Theory further predicts that this system should host ferromagnetic helical nodal lines [217]. The majority of experimental work thus far has focused on the synthesis and exploration of bulk single crystals of FeSn and Fe_3Sn_2. However, a controllable synthesis of thin film in these two crystal structures, crucial for the application in devices and nano-patterned structures, has lagged behind the bulk crystal growth. In particular, while FeSn thin films have recently been successfully grown using molecular beam epitaxy (MBE) [218–220], MBE growth of Fe_3Sn_2 has been difficult to successfully realize. Here we use MBE to synthesize and study thin films of both FeSn and Fe_3Sn_2. By tuning the elemental flux ratio and the substrate temperature, we demonstrate how each of the two structures can be created. We characterize the films using electron and X-ray diffraction, magnetization measurements and scanning tunneling microscopy/spectroscopy (STM/S) to evaluate structural, electronic and magnetic properties of our films. Our work provides a foundation for the application of FeSn and Fe_3Sn_2 thin films in mesoscale devices and heterostructure bilayers.

Crystal structure of Fe_xSn_y materials is composed of two constituent layers, a kagome Fe_3Sn layer and a honeycomb Sn layer, stacked along the c-axis (Fig. 5.2.1a-c). In FeSn, the hexagonal unit cell (a=b=5.31 Å, c=4.46 Å) consists of a honeycomb Sn layer and a kagome Fe_3Sn layer (Fig. 5.2.1b). The lattice structure of Fe_3Sn_2 is also hexagonal (a=b=5.34 Å, c=19.79 Å), composed of alternating Fe_3Sn bilayers and Sn layers that generate a 9-layer unit cell (Fig. 5.2.1a).

To grow thin films of FeSn and Fe_3Sn_2, buffered hydrogen fluoride treated Nb-doped (0.05 wt%) $SrTiO_3$ (111) substrate (5 mm $\times$ 5 mm $\times$ 0.5 mm) (Shinkosha) was cleaned in acetone and 2-propanol in an ultrasonic bath and then introduced into our MBE system (Fermion Instruments) with a base pressure of $\sim 5 \times 10^{-10}$ Torr. The substrate was first slowly heated to the growth temperature (Table 5.1), which was continuously monitored by

a pyrometer (emissivity=0.7). Thereafter, Fe (99%) and Sn (99.9999%) were co-evaporated from individual Knudsen cells after the flux rates were calibrated using a quartz crystal microbalance (QCM) (Table 5.1). For STM measurements, thin films were transferred using a vacuum suitcase chamber held at 1×10^{-9} Torr, and are never exposed to air. For *ex-situ* X-ray diffraction and magnetization measurements, a brief exposure to air and the storage in the desiccator over a course of few days did not seem to interfere with the sample properties.

Sample	Fe temperature (°C)	Sn temperature (°C)	Fe:Sn flux ratio	Substrate temperature (°C)
A_1, A_2	1187	987	1:1	615
B	1187	976	1.3:1	615-626
C_1, C_2, C_3	1187	970	1.3:1	660

Table 5.1: Growth parameters of samples.

Sample	A_1	A_2	B	C_1	C_2	C_3
Thickness (nm)	243	979	343	230	46	20

Table 5.2: Thickness of samples.

We present data from films grown at three different temperatures: FeSn grown at ∼615 °C (samples A_1 and A2 with different thickness (Table 5.2)), Fe_3Sn_2 grown at ∼660 °C (samples C1, C2 and C3 (Table 5.2)) and the mixture of the two structures grown at an intermediate temperate ∼615 - 626 °C (sample B). Based on the morphology of the post-growth reflection high-energy electron diffraction (RHEED) pattern, all films show high crystallinity (Fig. 5.2.1d-k). RHEED images at two high symmetry azimuthal angles separated by 30 degrees also demonstrate the expected hexagonal ab-plane structure of the film surface. The spacing between the streaks in the RHEED pattern of thin films is slightly larger than that of $SrTiO_3$, which is expected based on the differences in the bulk lattice constants.

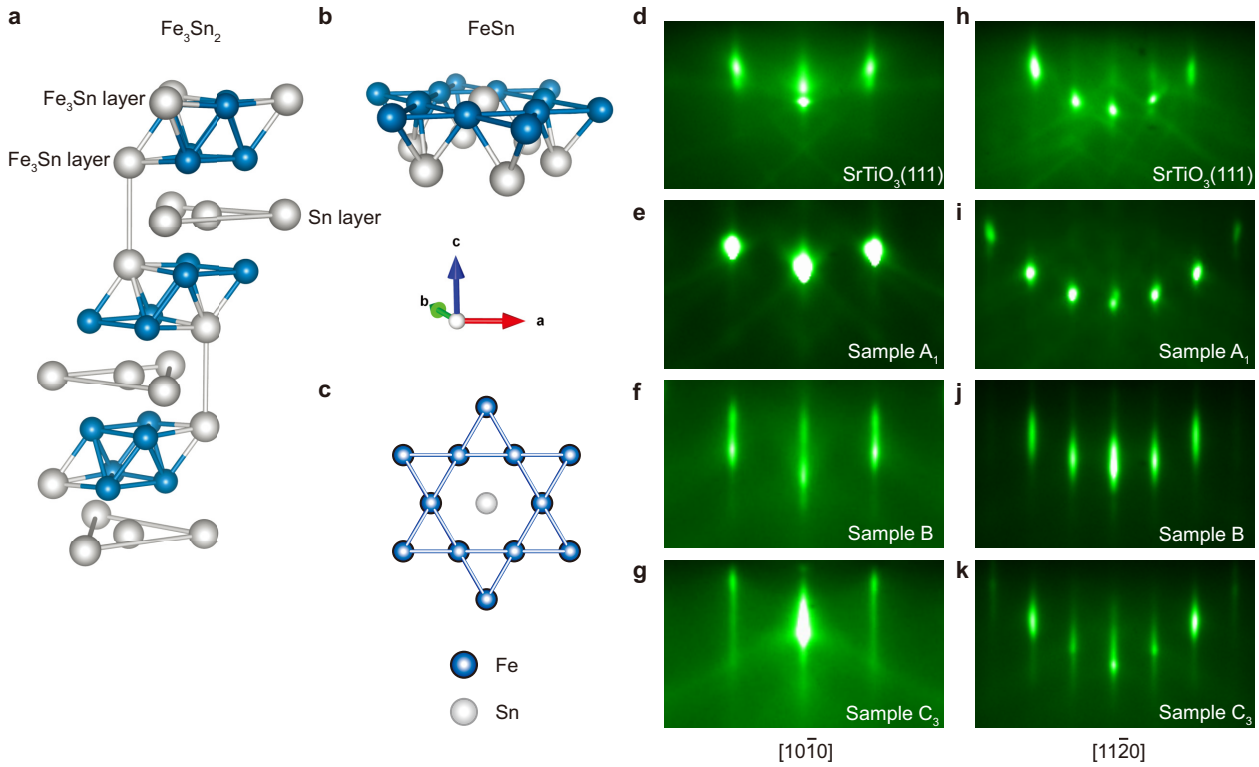

Figure 5.2.1: Crystal structures and reflection high energy electron diffraction (RHEED) images. a, b Crystal structure of Fe_3Sn_2 and FeSn, showing layers composing a single unit cell in each system. c The schematic of the Fe_3Sn kagome layer. Blue spheres represent Fe atoms and gray spheres represent Sn atoms. d-g RHEED images of $SrTiO_3$ substrate, samples A_1, B and C3 in $[10\bar{1}0]$ direction. h-k RHEED images of $SrTiO_3$ substrate, samples A_1, B and C3 in $[11\bar{2}0]$ direction.

Since in-plane lattice constants of FeSn and Fe_3Sn_2 are nearly identical, the two structures cannot be easily distinguished from in-situ RHEED images. Therefore, to identify the exact structure of each film, we use ex-situ room temperature X-ray diffraction with a copper K_α source (Fig. 5.2.2). Sample A_1, which was grown at the lowest temperature with Fe:Sn ∼1:1 flux ratio, primarily shows diffraction peaks (000l) (l=1,2) associated with FeSn, while the Fe_3Sn_2 peaks are notably absent, indicating the epitaxial growth of FeSn phase. sample C_1, grown at the highest temperature and Fe:Sn ∼1.3:1 flux ratio, predominantly shows the

Fe_3Sn_2 diffraction peaks (000l) (l=3, 6 and 9). This behavior is consistent with the Fe-Sn binary phase diagram, where lower temperature favors the formation of FeSn phase, while higher temperatures favors the Fe_3Sn_2 phase [221]. We note that the sample B, synthesized at an intermediate temperature and 1.3:1 flux ratio, shows the mixture of the two phases (Fig. 5.2.2b).

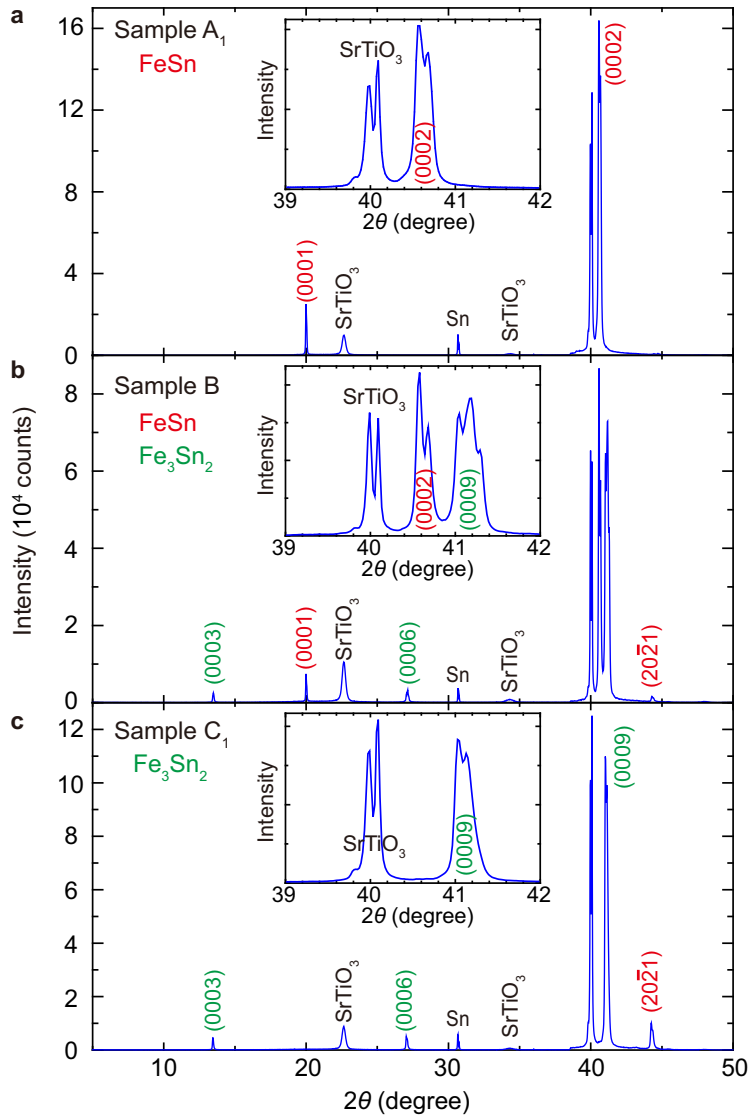

Figure 5.2.2: a-c X-ray diffraction measurements of samples A_1, B and C1, as indicated in the top left corner of each panel. Diffraction peaks consistent with FeSn (Fe_3Sn_2) phase are labeled in red (green). The inset in each panel magnifies the relevant peaks within 39° - 42° range, where peaks related to the film and the substrate can be clearly distinguished. We note that the peak at ∼44° is likely related to residual formation of small randomly oriented FeSn clusters, as hypothesized in Ref. [219]. Data was acquired at 295 K using a copper K_α source.

We proceed to investigate magnetic properties of our films by measuring magnetization (M) as a function of temperature (T) and in-plane magnetic field (H) using a magnetic properties measurement system (Quantum Design MPMS3). For the FeSn thin film (sample A_2), M vs. T curve shows a bump at ∼369 K (Fig. 5.2.3b inset), which is consistent with the onset of antiferromagnetic ordering at a nearly identical temperature as that observed in FeSn bulk single crystals [215]. As expected, the net magnetic moment per Fe atom is very small across the entire temperature range measured (Fig. 5.2.3b), consistent with the value measured on bulk FeSn [222]. In contrast, the magnetic moment in Fe_3Sn_2 thin film (sample C_2) is ∼1-2 orders of magnitude larger (Fig. 5.2.3d). It saturates at +/- 1 T field applied perpendicular to c-axis, which is indicative of ferromagnetic ordering in the film (Fig. 5.2.3d). The saturation moment per Fe in our MBE-grown Fe_3Sn_2 thin films is comparable to that in Fe_3Sn_2 films grown by magnetron sputtering [223] and bulk single crystals [194, 210]. We note that the expected Curie temperature of ∼640 -660 K [208, 214, 216] is beyond the range of our MPMS, and we cannot identify it in this study. Nevertheless, the emergence of ferromagnetism is further supported by the hysteresis in M vs H plot that we can clearly observe at low temperature (inset in Fig. 5.2.3d).

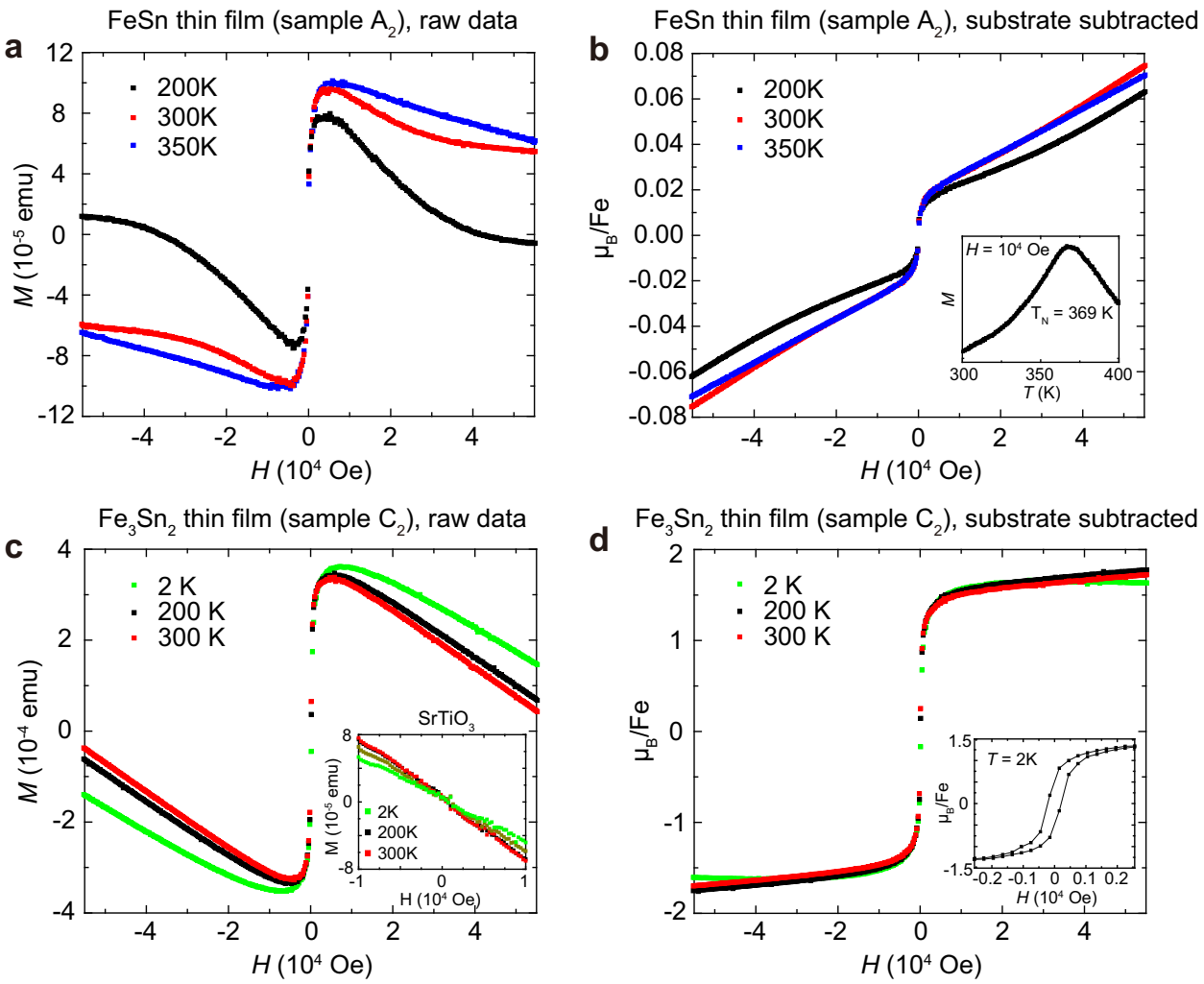

Figure 5.2.3: Magnetic properties of FeSn and Fe_3Sn_2 thin films. a Magnetization (M) vs. magnetic field (H) raw data of FeSn thin film (sample A_2). b M vs. H curves of the same sample A_2 after the diamagnetic substrate moment (inset in c) is subtracted out. The ferromagnetic-shaped part of the curves near zero field in a,b is possibly due to residual amounts of Fe_3Sn_2 impurity phase or excess Fe. Inset in b shows the M vs. temperature (T) curve of sample A_2 obtained in 104 Oe field after the substrate contribution is subtracted out. c, d M vs. H data of Fe_3Sn_2 (sample C_2) before (c) and after (d) subtracting the substrate moment. Inset of d shows ferromagnetic hysteresis loop of sample C_2 after subtracting the substrate moment, acquired at 2 K. Magnetic field was applied parallel to the ab-plane in all panels.

Lastly, we explore the surface structure and surface magnetic properties using low-temperature STM/S at ∼4.5 K (Unisoku USM1300). Atomically-resolved STM topographs of both FeSn (sample A_1) and Fe_3Sn_2 (sample C_3) films show the expected hexagonal lattice structure (Fig. 5.2.4a,e). Large-scale STM topograph of FeSn also shows atomic steps, each consistent with a single unit cell height of FeSn (Fig. 5.2.4b). Differential conductance dI/dV spectra acquired on the surface of the FeSn film are not sensitive to externally applied magnetic field, and look remarkably similar to the dI/dV spectra obtained on the Sn surface of FeSn bulk single crystals (Fig. 5.2.4c,d). This provides further support that the electronic structure of our FeSn thin films is similar to that of FeSn bulk single crystals. STM results on the Fe_3Sn_2 films will be discussed in the next section.

We also examine the layer stacking in Fe_3Sn_2 in an STM topograph across an Fe_3Sn-Fe_3Sn step (Fig. 5.2.5a). The insets show that the local minima in the topograph correspond to the Sn atoms, so we pick out the local minima represented by the yellow single pixels in Fig. 5.2.5b. By connecting these points along a-axis or b-axis seperately on the upper layer and lower layer by the orange and blue lines, and by comparing the relative spacing between these lines, we find a consistent stacking to the ideal Fe_3Sn_2 lattice (Fig. 5.2.5c).

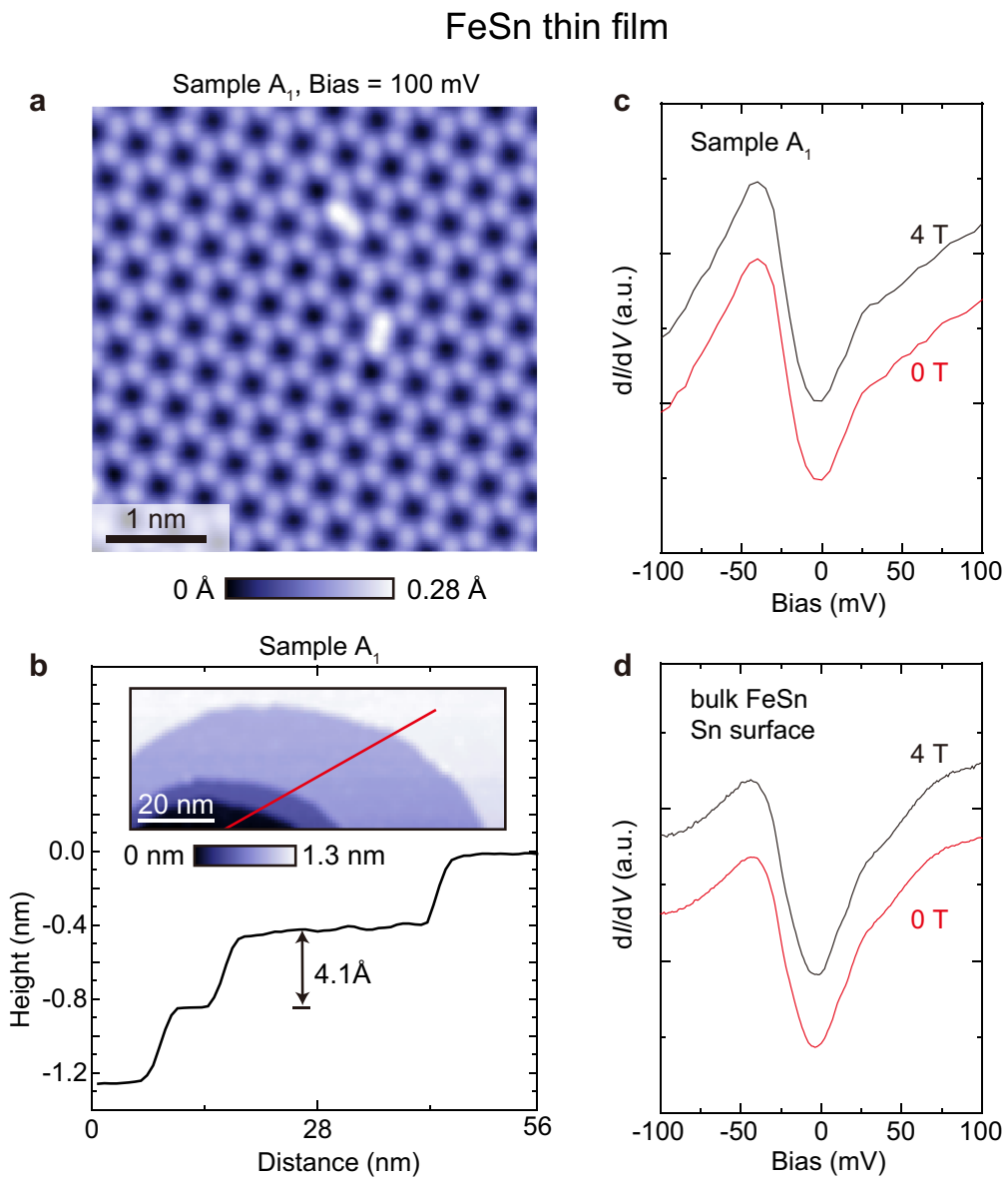

Figure 5.2.4: a STM topograph of FeSn thin film (sample A_1). b Topographic height profile across atomic steps with single unit cell height, denoted by the red line in the inset. c dI/dV spectra acquired on FeSn thin film (sample A_1) that show no magnetic field dependence. d dI/dV spectra acquired on the Sn surface of bulk FeSn sample, which closely resemble those on FeSn thin film in c. STM setup conditions: a I_{set} = 500 pA, V_{sample} = 100 mV; b I_{set} = 10 pA, V_{sample} = 1 V.

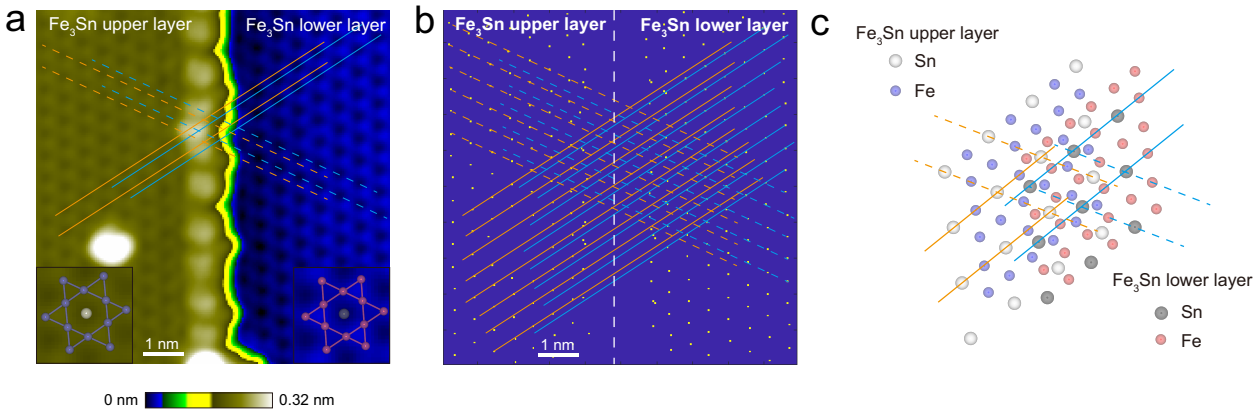

Figure 5.2.5: a STM topograph of an atomic step across the Fe_3Sn-Fe_3Sn step. b Local minima picked out from a as the yellow pixels. c Schematic of the ideal Fe_3Sn-Fe_3Sn step.

In summary, we synthesize FeSn and Fe_3Sn_2 thin films on top of $SrTiO_3(111)$ substrates using molecular beam epitaxy. We characterize structural properties of the films by using in-situ RHEED imaging, ex-situ X-ray diffraction and scanning tunneling microscopy, which all confirm the expected surface and bulk structure of the films. Magnetization measurements as a function of temperature and magnetic field show signatures of antiferromagnetism and ferromagnetism, consistent with FeSn and Fe_3Sn_2, respectively. Lastly, we confirm that the STM topograph and the dI/dV spectra acquired on the FeSn thin film is comparable to the bulk single crystals. Future experiments could explore the effects of strain on electronic and magnetic properties of FeSn and Fe_3Sn_2 by for example using substrates with different lattice constants or by exploring films of reduced thickness.

5.3 Plethora of spectral features in Fe_3Sn_2 thin films

With the high quality of the Fe_3Sn_2 thin film, we next explore its electronic properties using STM/S. dI/dV spectra of the films are found to be generally consistent with those from the bulk material [209]. The upturn at E_0 is consistent with Ref. [209] where it was attributed to the flat band. The spectra are robust across a large area over the sample,

showing minimal effect of the defects (Fig. 5.3.1(b)). FT of the L-maps ((dI/dV)/(I/V)) exhibits predominantly diffuse scattering wave vectors near the center, but a enhanced signal is observed near E_0 in the radially averaged linecut of the FT of the L-maps. A minimal thickness-dependence (Fig. 5.3.1(c) inset) shows the robustness of the electronic structure of our films.

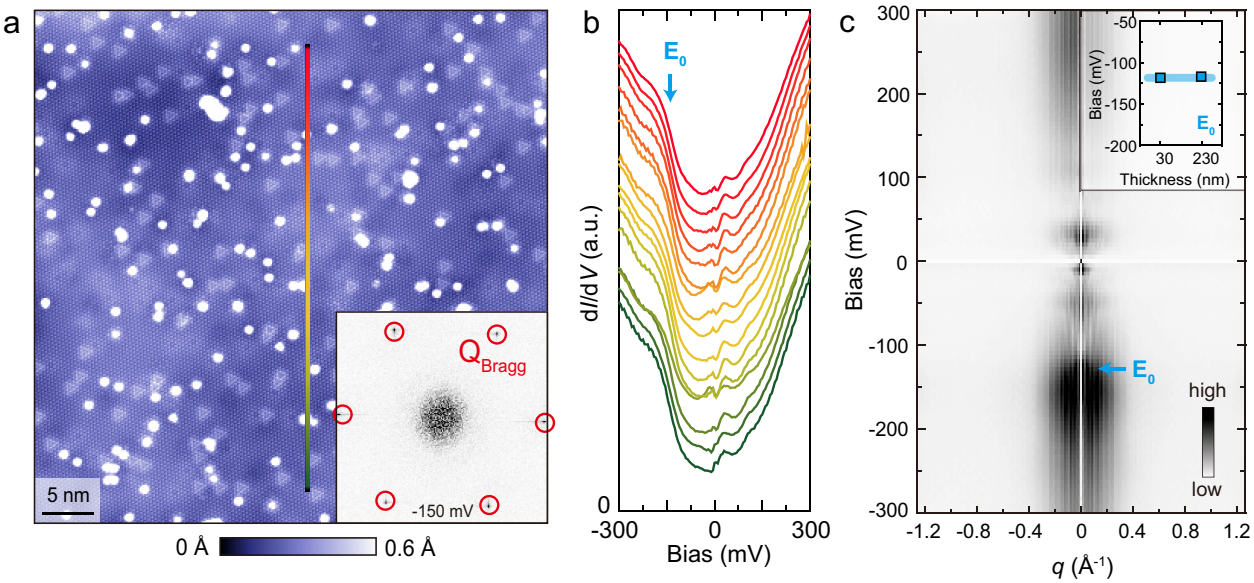

Figure 5.3.1: (a) Large region STM topograph. Inset shows the FT of a L-map ((dI/dV)/(I/V)) for bias V = -150 mV. (b) dI/dV spectra taken along the vertical line in (a). E_0 denote the upturn associated with the flat band [209]. (c) Radially averaged linecut starting from the center of the FT of L-map. Inset indicates the consistency of E_0 between two films of different thicknesses. STM setup conditions: a I_{set} = 96 pA, V_{sample} = 12 mV; inset in a, b-c I_{set} = 1 nA, V_{sample} = 300 mV, V_{exc} = 5 mV.

Next we turn to the spectral features in the vicinity of E_F. Remarkbly, there are six peaks discerned in the dI/dV spectra within $E_F \pm 50$ mV which all disperse when a magnetic field along c-axis is applied (Fig. 5.3.2(a)). By calculating the numerical second derivative of the dI/dV spectra, these features are even better manifested (Fig. 5.3.2(b)).

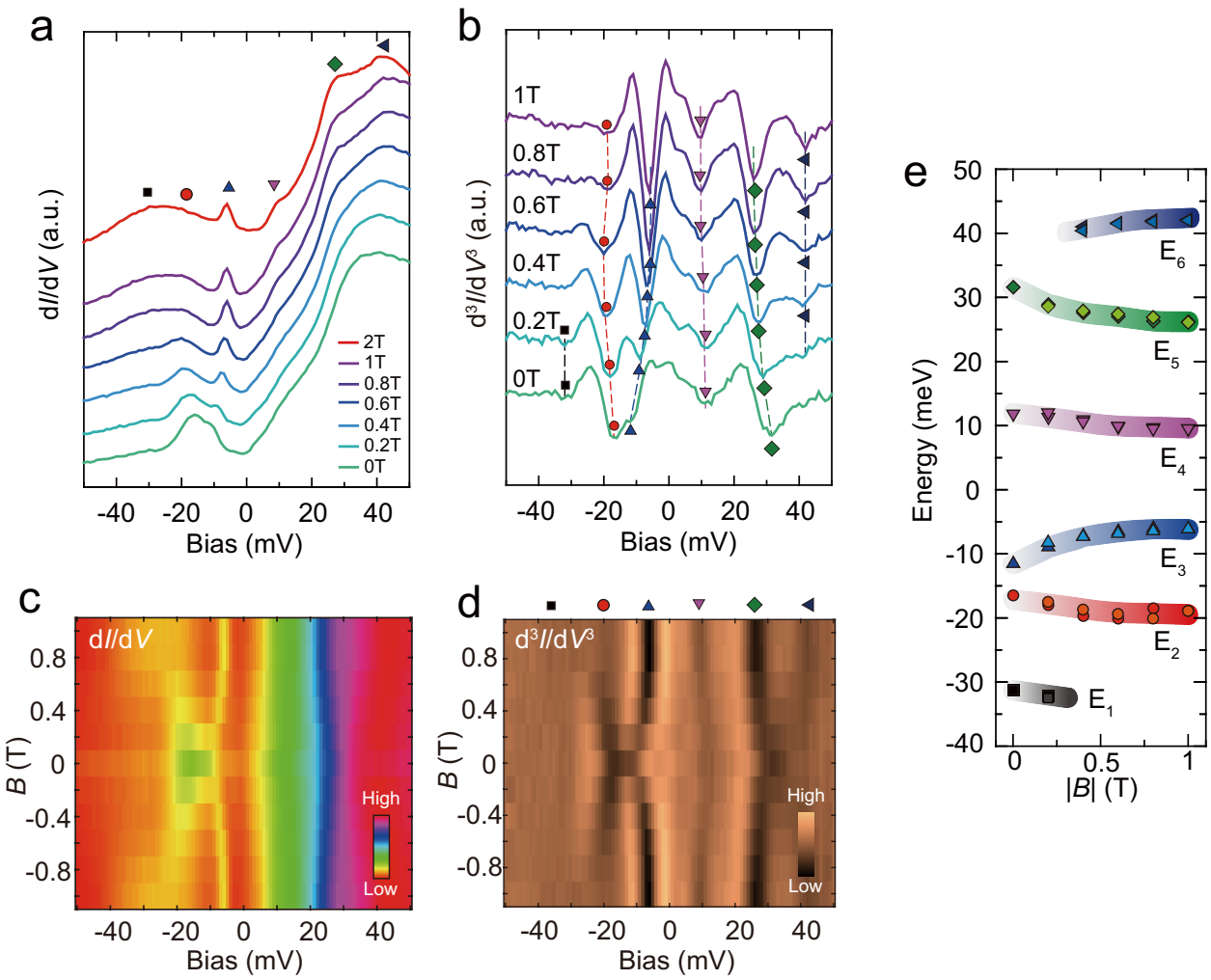

Figure 5.3.2: Plethora of dI/dV features tunable by field. (a) Average dI/dV spectra acquired in different fields. (b) Second derivative of (a). (c),(d) Waterfall plots of dI/dV and the second derivative as a function of the field, including the negative fields. (e) Dispersion of the dI/dV features in field, extracted from (b).

The peak dispersion apparently saturates at ∼1 T, indicating that the dispersion is driven by the rotation of the magnetic moments as the magnetization data also exhibits a saturation at 1 T (Fig. 5.2.3). Furthermore, applying a field antiparallel to the c-axis yield the same dispersion (Fig. 5.3.2(c,d)). By identifying the local minima in the second derivative plot, which correspond to the peaks in dI/dV spectra, we extract the dispersion of the six peaks

in field (Fig. 5.3.2(e)).

To further verify the extracted peak dispersion, we also use an alternative method. Since the dI/dV spectra within (-100,0) mV is generally flat (Fig. 5.3.1(b)), we can use three Gaussians to fit the three peaks $E_{1,2,3}$. Fig. 5.3.3(a-f) display the raw dI/dV spectra (blue circles) and the fits (thick green curves). The fitting turns out to be extremely good. The dispersion of peaks $E_{1,2,3}$ is extracted by plotting the Gaussian centers (Fig. 5.3.3(g)), and it is highly consistent with the dispersion extracted by the second derivative method.

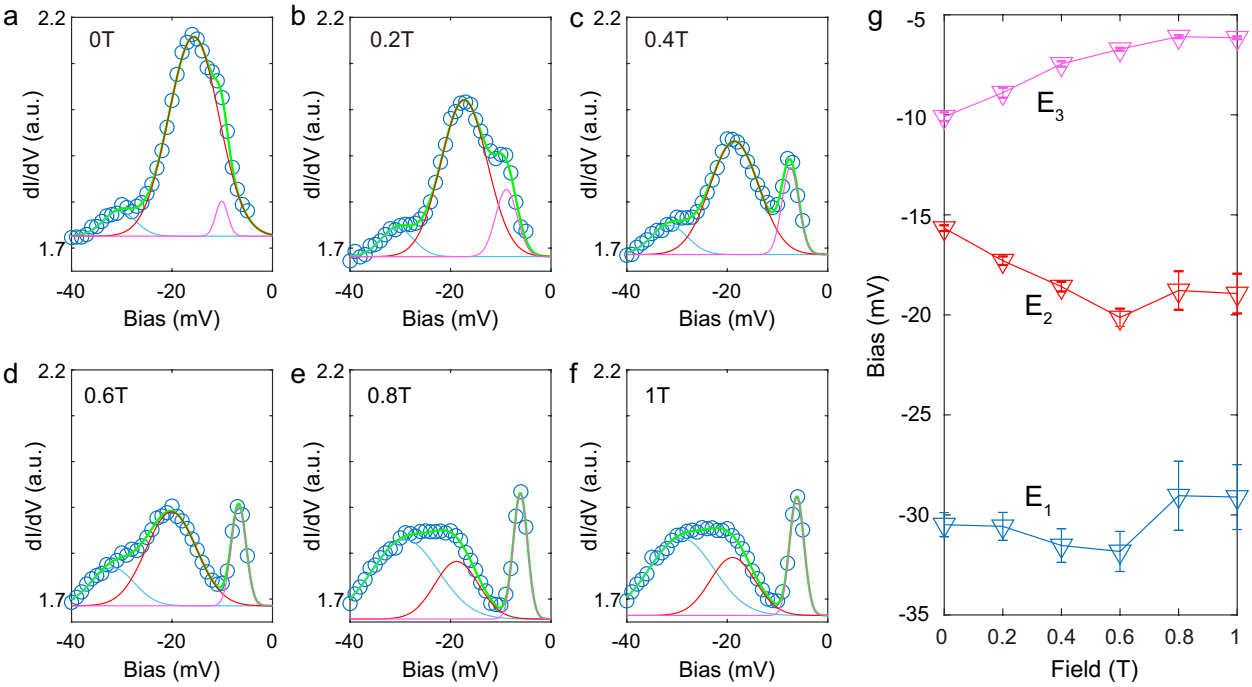

Figure 5.3.3: (a-f) Negative bias portion of the dI/dV spectra (blue circles) fitted by three Gaussian curves (thin lines). Thick green curves are the sum of three Gaussians. (g) Dispersion of $E_{1,2,3}$ extracted from the center of the three Gaussians as a function of field.

Furthermore, we observe quasiparticle interference (QPI) features in the dI/dV($\mathbf{r}$, V) maps. The main scattering wave vector $\mathbf{q}_1$ corresponds to the scattering between Brillouin zone corners (K, K' points) (Fig. 5.3.4(a)). These QPI signal appears within a small bias range and exhibits a field-dependence similar to the dI/dV features (Fig. 5.3.4(b,c)).

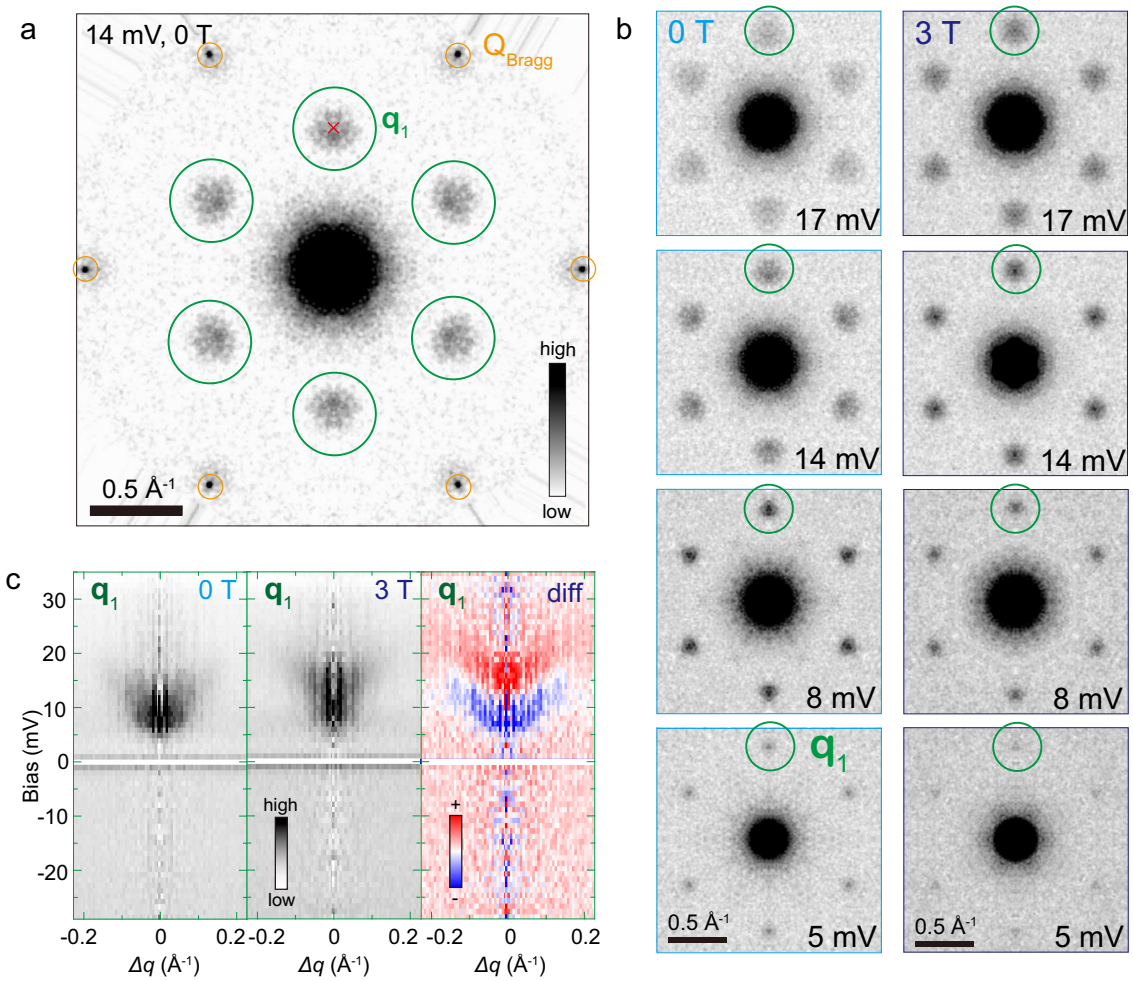

Figure 5.3.4: QPI in the vicinity of Fermi level. (a) Six-fold symmetrized FT of L-map at 14 mV. Bragg peaks are enclosed by the orange circles. The QPI wave vectors are circled in green. (b) Comparison of FT of L-maps acquired in 0T and 3T. (c) Radially averaged linecuts of FT of L-maps starting at $(\mathbf{Q}_{Bragg,1} + \mathbf{Q}_{Bragg,2})/3$, focusing on the region within the green circles at 0T, 3T and their difference. STM setup conditions: I_{set} = 280 pA, V_{sample} = 35 mV, V_{exc} = 1 mV.

5.4 Interpretation of the spectral features in the context of Weyl physics

In this section I will try to provide a possible interpretation of our data. Although magnetic field tunability is common in magnetic materials, for example in Ref. [224], it is extremely rare to observe as many as six tunable features in the vicinity of E_F. While Landau levels can produce many dI/dV peaks [225–227], it is ruled out here as the dispersion of the dI/dV peaks saturates at 1 T. Ref. [210] suggests a Dirac gap modulation, however, this is again unlikely in our case because the Dirac cones observed by ARPES in Fe_3Sn_2 bulk materials reside well below E_F [194].

Interestingly, recent *ab initio* calculations suggest the existence of six sets of Weyl points within $E_F \pm 50$ meV in Fe_3Sn_2, assuming the magnetization is polarized out-of-plane [217]. By comparing the energy of the dI/dV peaks E_1-E_6 and the energy of the Weyl points W_1-W_6, we find them to be remarkably consistent (Fig. 5.4.1(a)). Since a pair of Weyl nodes in the bulk is accompanied by the Fermi arc surface state connecting the surface projection of the two nodes, enhancement in dI/dV spectra can be understood as the contribution of DOS from the surface Fermi arc states of the six sets of Weyl points [228, 229]. Furthermore, Weyl points are predicted to be tunable by rotating the magnetization [230, 231], which may explain the peak dispersion in magnetic field that we observe.

The QPI signatures are another piece of evidence supporting the Weyl physics interpretation. Theoretically predicted Weyl nodes W_4 are located near the Brillouin zone corners, whose Fermi arc states, if assumed to be localized near W_4, would facilitate quasiparticle scattering between K, K' points, which is consistent with the QPI signatures $\mathbf{q}_1$ in our data (Fig. 5.4.1(b)). Moreover, the energy window (5-20 meV) where $\mathbf{q}_1$ appears is compatible with the energy of W_4 (Fig. 5.3.4).

Putting all the pieces of evidence together, our data is highly consistent with the calculated Weyl points in Fe_3Sn_2.

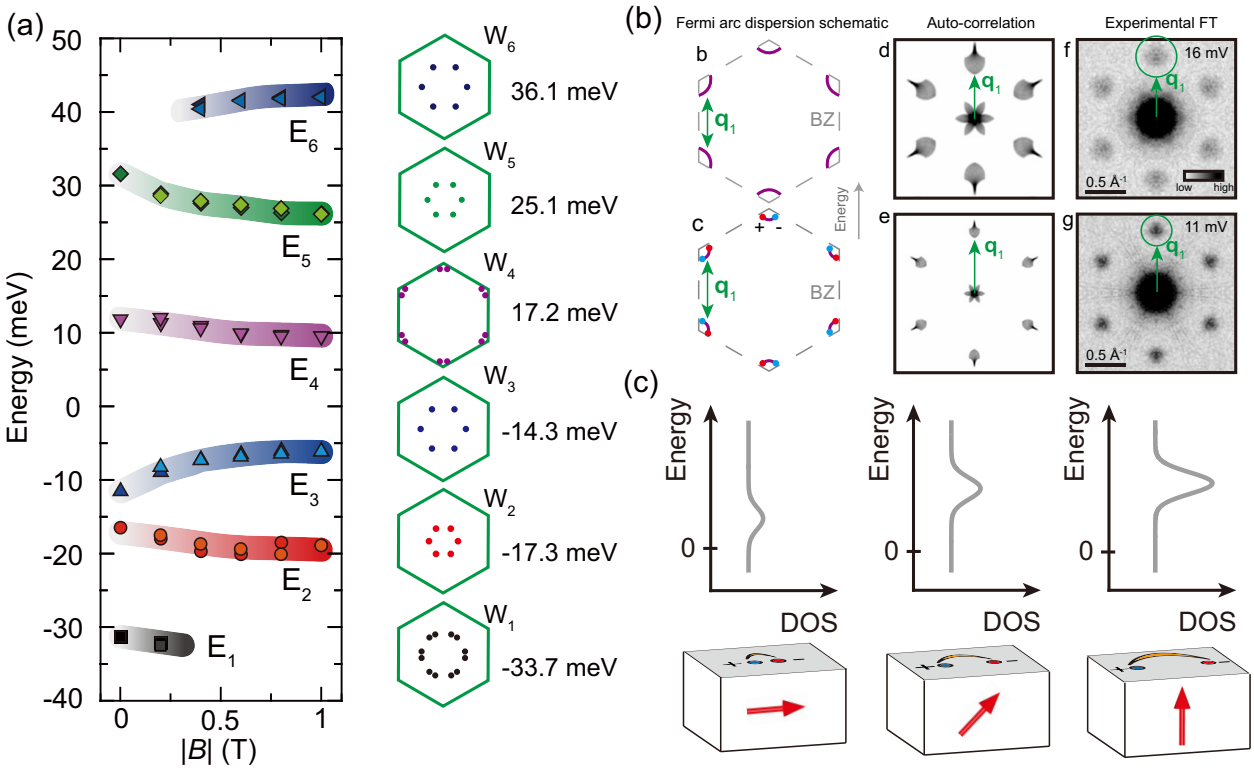

Figure 5.4.1: Comparison of spectral features and calculated Weyl points. (a) Comparison of dI/dV peak energy and the energy of the six sets of Weyl points. (b) Schematic of Fermi arcs of W_4 (left), their auto-correlation (middle) and the experimental FT of L-maps. (c) Schematic of the tunability of the Fermi arc states as the magnetization is rotated out-of-plane and the modulation of the DOS.

5.5 Conclusion

We implement a simple MBE synthesis recipe for the selective synthesis of the FeSn and Fe_3Sn_2 thin films. We cross-check the quality of the films by measuring the structural, magnetic and electronic properties using RHEED, XRD, STM/S and SQUID. In Fe_3Sn_2 thin films, we discover a plethora of spectral features and find that it is highly consistent with a set of theoretically proposed Weyl points.

The successful synthesis of the Fe_xSn_y thin films offers a platform for exploring the

correlated and topological states. Further experiments include using other experimental probes to study the Weyl physics, studying the strain effects by depositting the films on different substrate materials, and pursuing ultra-thin limit of these kagome structure.

References

[1] Wikipedia contributors. Quantum materials — Wikipedia, the free encyclopedia, 2022. [Online; accessed 21-April-2022].

[2] Wikipedia contributors. Macroscopic quantum phenomena — Wikipedia, the free encyclopedia, 2021. [Online; accessed 21-April-2022].

[3] N.W. Ashcroft, A.N. W, N.D. Mermin, N.D. Mermin, and Brooks/Cole Publishing Company. *Solid State Physics*. HRW international editions. Holt, Rinehart and Winston, 1976.

[4] Roberta Sinatra, Pierre Deville, Michael Szell, Dashun Wang, and Albert-László Barabási. A century of physics. *Nature Physics*, 11(10):791–796, Oct 2015.

[5] W. L. McMillan. Transition temperature of strong-coupled superconductors. *Phys. Rev.*, 167:331–344, Mar 1968.

[6] A. Schilling, M. Cantoni, J. D. Guo, and H. R. Ott. Superconductivity above 130 K in the Hg–Ba–Ca–Cu–O system. *Nature*, 363(6424):56–58, May 1993.

[7] J. Bardeen, L. N. Cooper, and J. R. Schrieffer. Microscopic theory of superconductivity. *Phys. Rev.*, 106:162–164, Apr 1957.

[8] J. Bardeen, L. N. Cooper, and J. R. Schrieffer. Theory of superconductivity. *Phys. Rev.*, 108:1175–1204, Dec 1957.

[9] Leon N. Cooper. Bound electron pairs in a degenerate fermi gas. *Phys. Rev.*, 104:1189–1190, Nov 1956.

[10] John Bardeen and David Pines. Electron-phonon interaction in metals. *Phys. Rev.*, 99:1140–1150, Aug 1955.

[11] Herbert Fröhlich. Interaction of electrons with lattice vibrations. *Proceedings of the Royal Society of London. Series A. Mathematical and Physical Sciences*, 215(1122):291–298, 1952.

[12] Patrick A. Lee, Naoto Nagaosa, and Xiao-Gang Wen. Doping a mott insulator: Physics of high-temperature superconductivity. *Rev. Mod. Phys.*, 78:17–85, Jan 2006.

[13] Andrea Damascelli, Zahid Hussain, and Zhi-Xun Shen. Angle-resolved photoemission studies of the cuprate superconductors. *Rev. Mod. Phys.*, 75:473–541, Apr 2003.

[14] G. R. Stewart. Heavy-fermion systems. *Rev. Mod. Phys.*, 56:755–787, Oct 1984.

[15] G. R. Stewart. Superconductivity in iron compounds. *Rev. Mod. Phys.*, 83:1589–1652, Dec 2011.

[16] Danfeng Li, Kyuho Lee, Bai Yang Wang, Motoki Osada, Samuel Crossley, Hye Ryoung Lee, Yi Cui, Yasuyuki Hikita, and Harold Y. Hwang. Superconductivity in an infinite-layer nickelate. *Nature*, 572(7771):624–627, Aug 2019.

[17] Yoshiteru Maeno, T. Maurice Rice, and Manfred Sigrist. The intriguing superconductivity of strontium ruthenate. *Physics Today*, 54(1):42–47, 2001.

[18] Yuan Cao, Valla Fatemi, Shiang Fang, Kenji Watanabe, Takashi Taniguchi, Efthimios Kaxiras, and Pablo Jarillo-Herrero. Unconventional superconductivity in magic-angle graphene superlattices. *Nature*, 556(7699):43–50, Apr 2018.

[19] Leon Balents, Cory R. Dean, Dmitri K. Efetov, and Andrea F. Young. Superconductivity and strong correlations in moiré flat bands. *Nature Physics*, 16(7):725–733, Jul 2020.

[20] He Zhao, Zheng Ren, Bryan Rachmilowitz, John Schneeloch, Ruidan Zhong, Genda Gu, Ziqiang Wang, and Ilija Zeljkovic. Charge-stripe crystal phase in an insulating cuprate. *Nature Materials*, 18(2):103–107, Feb 2019.

[21] Bryan Rachmilowitz, He Zhao, Zheng Ren, Hong Li, Konrad H. Thomas, John Marangola, Shang Gao, John Schneeloch, Ruidan Zhong, Genda Gu, Christian Flindt, and Ilija Zeljkovic. Coulomb blockade effects in a topological insulator grown on a high-Tc cuprate superconductor. *npj Quantum Materials*, 5(1):72, Oct 2020.

[22] Zheng Ren, Hong Li, He Zhao, Shrinkhala Sharma, Ziqiang Wang, and Ilija Zeljkovic. Nanoscale decoupling of electronic nematicity and structural anisotropy in FeSe thin films. *Nature Communications*, 12(1):10, Jan 2021.

[23] He Zhao, Bryan Rachmilowitz, Zheng Ren, Ruobin Han, J. Schneeloch, Ruidan Zhong, Genda Gu, Ziqiang Wang, and Ilija Zeljkovic. Superconducting proximity effect in a topological insulator using Fe(Te, Se). *Phys. Rev. B*, 97:224504, Jun 2018.

[24] Wikimedia Commons. File:timeline of superconductivity from 1900 to 2015.svg — wikimedia commons, the free media repository, 2021. [Online; accessed 25-April-2022].

[25] Pia Jensen Ray. *Structural Investigation of La (2-x) Sr (x) CuO (4+ y): Following a Staging as a Function of Temperature*. Niels Bohr Institute, Copenhagen University, 2015.

[26] Wikimedia Commons. File:cuprates phasedigagram en.svg — wikimedia commons, the free media repository, 2020. [Online; accessed 25-April-2022].

[27] Ming Yi, Yan Zhang, Zhi-Xun Shen, and Donghui Lu. Role of the orbital degree of freedom in iron-based superconductors. *npj Quantum Materials*, 2(1):57, Oct 2017.

[28] Chen Fang, Hong Yao, Wei-Feng Tsai, JiangPing Hu, and Steven A. Kivelson. Theory of electron nematic order in LaFeAsO. *Phys. Rev. B*, 77:224509, Jun 2008.

[29] Cenke Xu, Markus Muller, and Subir Sachdev. Ising and spin orders in the iron-based superconductors. *Phys. Rev. B*, 78:020501, Jul 2008.

[30] Andrey V. Chubukov, M. Khodas, and Rafael M. Fernandes. Magnetism, superconductivity, and spontaneous orbital order in iron-based superconductors: Which comes first and why? *Phys. Rev. X*, 6:041045, Dec 2016.

[31] S. Lederer, Y. Schattner, E. Berg, and S. A. Kivelson. Enhancement of superconductivity near a nematic quantum critical point. *Phys. Rev. Lett.*, 114:097001, Mar 2015.

[32] Masahito Yoshizawa, Daichi Kimura, Taiji Chiba, Shalamujiang Simayi, Yoshiki Nakanishi, Kunihiro Kihou, Chul-Ho Lee, Akira Iyo, Hiroshi Eisaki, Masamichi Nakajima, and Shin-ichi Uchida. Structural Quantum Criticality and Superconductivity in Iron-Based Superconductor Ba(Fe1-xCox)2As2. *Journal of the Physical Society of Japan*, 81(2):024604, 2012.

[33] P. Walmsley, C. Putzke, L. Malone, I. Guillamón, D. Vignolles, C. Proust, S. Badoux, A. I. Coldea, M. D. Watson, S. Kasahara, Y. Mizukami, T. Shibauchi, Y. Matsuda, and A. Carrington. Quasiparticle mass enhancement close to the quantum critical point in $\mathrm{bafe}_2(\mathrm{as}_{1-x}\mathbf{p}_x)_2$. *Phys. Rev. Lett.*, 110:257002, Jun 2013.

[34] Hsueh-Hui Kuo, Jiun-Haw Chu, Johanna C. Palmstrom, Steven A. Kivelson, and Ian R. Fisher. Ubiquitous signatures of nematic quantum criticality in optimally doped Fe-based superconductors. *Science*, 352(6288):958–962, 2016.

[35] Amalia I. Coldea and Matthew D. Watson. The Key Ingredients of the Electronic Structure of FeSe. *Annual Review of Condensed Matter Physics*, 9(1):125–146, 2018.

[36] Anna E Böhmer and Andreas Kreisel. Nematicity, magnetism and superconductivity in FeSe. *Journal of Physics: Condensed Matter*, 30(2):023001, dec 2017.

[37] Andreas Kreisel, Peter J. Hirschfeld, and Brian M. Andersen. On the Remarkable Superconductivity of FeSe and Its Close Cousins. *Symmetry*, 12(9), 2020.

[38] S.-H. Baek, D. V. Efremov, J. M. Ok, J. S. Kim, Jeroen van den Brink, and B. Büchner. Orbital-driven nematicity in FeSe. *Nature Materials*, 14(2):210–214, Feb 2015.

[39] Pierre Massat, Donato Farina, Indranil Paul, Sandra Karlsson, Pierre Strobel, Pierre Toulemonde, Marie-Aude Méasson, Maximilien Cazayous, Alain Sacuto, Shigeru Kasahara, Takasada Shibauchi, Yuji Matsuda, and Yann Gallais. Charge-induced nematicity in FeSe. *Proceedings of the National Academy of Sciences*, 113(33):9177–9181, 2016.

[40] Naoyuki Katayama, Sungdae Ji, Despina Louca, Seunghun Lee, Masaki Fujita, Taku J. Sato, Jinsheng Wen, Zhijun Xu, Genda Gu, Guangyong Xu, Ziwei Lin, Masanori Enoki, Sung Chang, Kazuyoshi Yamada, and John M. Tranquada. Investigation of

the Spin-Glass Regime between the Antiferromagnetic and Superconducting Phases in Fe1+ySexTe1-x. *Journal of the Physical Society of Japan*, 79(11):113702, 2010.

[41] P. Reiss, M. D. Watson, T. K. Kim, A. A. Haghighirad, D. N. Woodruff, M. Bruma, S. J. Clarke, and A. I. Coldea. Suppression of electronic correlations by chemical pressure from FeSe to FeS. *Phys. Rev. B*, 96:121103, Sep 2017.

[42] K. Matsuura, Y. Mizukami, Y. Arai, Y. Sugimura, N. Maejima, A. Machida, T. Watanuki, T. Fukuda, T. Yajima, Z. Hiroi, K. Y. Yip, Y. C. Chan, Q. Niu, S. Hosoi, K. Ishida, K. Mukasa, S. Kasahara, J.-G. Cheng, S. K. Goh, Y. Matsuda, Y. Uwatoko, and T. Shibauchi. Maximizing Tc by tuning nematicity and magnetism in FeSe1-xSx superconductors. *Nature Communications*, 8(1):1143, Oct 2017.

[43] Yuki Sato, Shigeru Kasahara, Tomoya Taniguchi, Xiangzhuo Xing, Yuichi Kasahara, Yoshifumi Tokiwa, Youichi Yamakawa, Hiroshi Kontani, Takasada Shibauchi, and Yuji Matsuda. Abrupt change of the superconducting gap structure at the nematic critical point in FeSe1-xSx. *Proceedings of the National Academy of Sciences*, 115(6):1227–1231, 2018.

[44] Dongfei Wang, Lingyuan Kong, Peng Fan, Hui Chen, Shiyu Zhu, Wenyao Liu, Lu Cao, Yujie Sun, Shixuan Du, John Schneeloch, Ruidan Zhong, Genda Gu, Liang Fu, Hong Ding, and Hong-Jun Gao. Evidence for majorana bound states in an iron-based superconductor. *Science*, 362(6412):333–335, 2018.

[45] Shiyu Zhu, Lingyuan Kong, Lu Cao, Hui Chen, Michał Papaj, Shixuan Du, Yuqing Xing, Wenyao Liu, Dongfei Wang, Chengmin Shen, Fazhi Yang, John Schneeloch, Ruidan Zhong, Genda Gu, Liang Fu, Yu-Yang Zhang, Hong Ding, and Hong-Jun Gao. Nearly quantized conductance plateau of vortex zero mode in an iron-based superconductor. *Science*, 367(6474):189–192, 2020.

[46] Qing-Yan Wang, Zhi Li, Wen-Hao Zhang, Zuo-Cheng Zhang, Jin-Song Zhang, Wei Li, Hao Ding, Yun-Bo Ou, Peng Deng, Kai Chang, Jing Wen, Can-Li Song, Ke He, Jin-Feng Jia, Shuai-Hua Ji, Ya-Yu Wang, Li-Li Wang, Xi Chen, Xu-Cun Ma, and Qi-Kun Xue. Interface-induced high-temperature superconductivity in single unit-cell FeSe films on SrTiO 3. *Chinese Physics Letters*, 29(3):037402, mar 2012.

[47] Dennis Huang and Jennifer E. Hoffman. Monolayer FeSe on $SrTiO_3$. *Annual Review of Condensed Matter Physics*, 8(1):311–336, 2017.

[48] X. G. WEN. Topological orders in rigid states. *International Journal of Modern Physics B*, 04(02):239–271, 1990.

[49] K. v. Klitzing, G. Dorda, and M. Pepper. New method for high-accuracy determination of the fine-structure constant based on quantized hall resistance. *Phys. Rev. Lett.*, 45:494–497, Aug 1980.

[50] K. S. Novoselov, Z. Jiang, Y. Zhang, S. V. Morozov, H. L. Stormer, U. Zeitler, J. C. Maan, G. S. Boebinger, P. Kim, and A. K. Geim. Room-temperature quantum hall effect in graphene. *Science*, 315(5817):1379–1379, 2007.

[51] Wikimedia Commons. File:rhoxy.jpg — wikimedia commons, the free media repository, 2021. [Online; accessed 2-May-2022].

[52] R. B. Laughlin. Quantized hall conductivity in two dimensions. *Phys. Rev. B*, 23:5632–5633, May 1981.

[53] B. I. Halperin. Quantized hall conductance, current-carrying edge states, and the existence of extended states in a two-dimensional disordered potential. *Phys. Rev. B*, 25:2185–2190, Feb 1982.

[54] D. J. Thouless, M. Kohmoto, M. P. Nightingale, and M. den Nijs. Quantized hall conductance in a two-dimensional periodic potential. *Phys. Rev. Lett.*, 49:405–408, Aug 1982.

[55] F. D. M. Haldane. Model for a quantum hall effect without landau levels: Condensed-matter realization of the "parity anomaly". *Phys. Rev. Lett.*, 61:2015–2018, Oct 1988.

[56] C. L. Kane and E. J. Mele. Quantum spin hall effect in graphene. *Phys. Rev. Lett.*, 95:226801, Nov 2005.

[57] B. Andrei Bernevig, Taylor L. Hughes, and Shou-Cheng Zhang. Quantum Spin Hall Effect and Topological Phase Transition in HgTe Quantum Wells. *Science*, 314(5806):1757–1761, 2006.

[58] Markus König, Steffen Wiedmann, Christoph Brüne, Andreas Roth, Hartmut Buhmann, Laurens W. Molenkamp, Xiao-Liang Qi, and Shou-Cheng Zhang. Quantum Spin Hall Insulator State in HgTe Quantum Wells. *Science*, 318(5851):766–770, 2007.

[59] D. Hsieh, D. Qian, L. Wray, Y. Xia, Y. S. Hor, R. J. Cava, and M. Z. Hasan. A topological dirac insulator in a quantum spin hall phase. *Nature*, 452(7190):970–974, Apr 2008.

[60] Haijun Zhang, Chao-Xing Liu, Xiao-Liang Qi, Xi Dai, Zhong Fang, and Shou-Cheng Zhang. Topological insulators in Bi2Se3, Bi2Te3 and Sb2Te3 with a single Dirac cone on the surface. *Nature Physics*, 5(6):438–442, Jun 2009.

[61] Y. L. Chen, J. G. Analytis, J.-H. Chu, Z. K. Liu, S.-K. Mo, X. L. Qi, H. J. Zhang, D. H. Lu, X. Dai, Z. Fang, S. C. Zhang, I. R. Fisher, Z. Hussain, and Z.-X. Shen. Experimental Realization of a Three-Dimensional Topological Insulator, Bi2Te3. *Science*, 325(5937):178–181, 2009.

[62] Y. Xia, D. Qian, D. Hsieh, L. Wray, A. Pal, H. Lin, A. Bansil, D. Grauer, Y. S. Hor, R. J. Cava, and M. Z. Hasan. Observation of a large-gap topological-insulator class with a single dirac cone on the surface. *Nature Physics*, 5(6):398–402, Jun 2009.

[63] D. Hsieh, Y. Xia, D. Qian, L. Wray, F. Meier, J. H. Dil, J. Osterwalder, L. Patthey, A. V. Fedorov, H. Lin, A. Bansil, D. Grauer, Y. S. Hor, R. J. Cava, and M. Z. Hasan. Observation of time-reversal-protected single-dirac-cone topological-insulator states in bi_2te_3 and sb_2te_3. *Phys. Rev. Lett.*, 103:146401, Sep 2009.

[64] Wikimedia Commons. File:topological insulator band structure.svg — wikimedia commons, the free media repository, 2020. [Online; accessed 2-May-2022].

[65] Paul Adrien Maurice Dirac and Ralph Howard Fowler. The quantum theory of the electron. *Proceedings of the Royal Society of London. Series A, Containing Papers of a Mathematical and Physical Character*, 117(778):610–624, 1928.

[66] Hermann Weyl. Gravitation and the electron. *Proceedings of the National Academy of Sciences*, 15(4):323–334, 1929.

[67] Conyers Herring. Accidental degeneracy in the energy bands of crystals. *Phys. Rev.*, 52:365–373, Aug 1937.

[68] N. P. Armitage, E. J. Mele, and Ashvin Vishwanath. Weyl and dirac semimetals in three-dimensional solids. *Rev. Mod. Phys.*, 90:015001, Jan 2018.

[69] B. Q. Lv, H. M. Weng, B. B. Fu, X. P. Wang, H. Miao, J. Ma, P. Richard, X. C. Huang, L. X. Zhao, G. F. Chen, Z. Fang, X. Dai, T. Qian, and H. Ding. Experimental Discovery of Weyl Semimetal TaAs. *Phys. Rev. X*, 5:031013, Jul 2015.

[70] Su-Yang Xu, Ilya Belopolski, Nasser Alidoust, Madhab Neupane, Guang Bian, Chenglong Zhang, Raman Sankar, Guoqing Chang, Zhujun Yuan, Chi-Cheng Lee, Shin-Ming Huang, Hao Zheng, Jie Ma, Daniel S. Sanchez, BaoKai Wang, Arun Bansil, Fangcheng Chou, Pavel P. Shibayev, Hsin Lin, Shuang Jia, and M. Zahid Hasan. Discovery of a weyl fermion semimetal and topological fermi arcs. *Science*, 349(6248):613–617, 2015.

[71] L. X. Yang, Z. K. Liu, Y. Sun, H. Peng, H. F. Yang, T. Zhang, B. Zhou, Y. Zhang, Y. F. Guo, M. Rahn, D. Prabhakaran, Z. Hussain, S.-K. Mo, C. Felser, B. Yan, and Y. L. Chen. Weyl semimetal phase in the non-centrosymmetric compound TaAs. *Nature Physics*, 11(9):728–732, Sep 2015.

[72] Lunan Huang, Timothy M. McCormick, Masayuki Ochi, Zhiying Zhao, Michi-To Suzuki, Ryotaro Arita, Yun Wu, Daixiang Mou, Huibo Cao, Jiaqiang Yan, Nandini Trivedi, and Adam Kaminski. Spectroscopic evidence for a type II Weyl semimetallic state in MoTe2. *Nature Materials*, 15(11):1155–1160, Nov 2016.

[73] A. Tamai, Q. S. Wu, I. Cucchi, F. Y. Bruno, S. Riccò, T. K. Kim, M. Hoesch, C. Barreteau, E. Giannini, C. Besnard, A. A. Soluyanov, and F. Baumberger. Fermi Arcs and Their Topological Character in the Candidate Type-II Weyl Semimetal $MoTe_2$. *Phys. Rev. X*, 6:031021, Aug 2016.

[74] J. Jiang, Z. K. Liu, Y. Sun, H. F. Yang, C. R. Rajamathi, Y. P. Qi, L. X. Yang, C. Chen, H. Peng, C.-C. Hwang, S. Z. Sun, S.-K. Mo, I. Vobornik, J. Fujii, S. S. P. Parkin, C. Felser, B. H. Yan, and Y. L. Chen. Signature of type-II Weyl semimetal phase in MoTe2. *Nature Communications*, 8(1):13973, Jan 2017.

[75] D. F. Liu, A. J. Liang, E. K. Liu, Q. N. Xu, Y. W. Li, C. Chen, D. Pei, W. J. Shi, S. K. Mo, P. Dudin, T. Kim, C. Cacho, G. Li, Y. Sun, L. X. Yang, Z. K. Liu, S. S. P. Parkin, C. Felser, and Y. L. Chen. Magnetic weyl semimetal phase in a kagome crystal. *Science*, 365(6459):1282–1285, 2019.

[76] Enke Liu, Yan Sun, Nitesh Kumar, Lukas Muechler, Aili Sun, Lin Jiao, Shuo-Ying Yang, Defa Liu, Aiji Liang, Qiunan Xu, Johannes Kroder, Vicky Süß, Horst Borrmann, Chandra Shekhar, Zhaosheng Wang, Chuanying Xi, Wenhong Wang, Walter Schnelle, Steffen Wirth, Yulin Chen, Sebastian T. B. Goennenwein, and Claudia Felser. Giant anomalous hall effect in a ferromagnetic kagome-lattice semimetal. *Nature Physics*, 14(11):1125–1131, Nov 2018.

[77] Noam Morali, Rajib Batabyal, Pranab Kumar Nag, Enke Liu, Qiunan Xu, Yan Sun, Binghai Yan, Claudia Felser, Nurit Avraham, and Haim Beidenkopf. Fermi-arc diversity on surface terminations of the magnetic Weyl semimetal Co3Sn2S2. *Science*, 365(6459):1286–1291, 2019.

[78] K. Kuroda, T. Tomita, M.-T. Suzuki, C. Bareille, A. A. Nugroho, P. Goswami, M. Ochi, M. Ikhlas, M. Nakayama, S. Akebi, R. Noguchi, R. Ishii, N. Inami, K. Ono, H. Kumigashira, A. Varykhalov, T. Muro, T. Koretsune, R. Arita, S. Shin, Takeshi Kondo, and S. Nakatsuji. Evidence for magnetic weyl fermions in a correlated metal. *Nature Materials*, 16(11):1090–1095, Nov 2017.

[79] Sergey Borisenko, Daniil Evtushinsky, Quinn Gibson, Alexander Yaresko, Klaus Koepernik, Timur Kim, Mazhar Ali, Jeroen van den Brink, Moritz Hoesch, Alexander Fedorov, Erik Haubold, Yevhen Kushnirenko, Ivan Soldatov, Rudolf Schäfer, and Robert J. Cava. Time-reversal symmetry breaking type-II Weyl state in YbMnBi2. *Nature Communications*, 10(1):3424, Jul 2019.

[80] Zheng Ren, Hong Li, Shrinkhala Sharma, Dipak Bhattarai, He Zhao, Bryan Rachmilowitz, Faranak Bahrami, Fazel Tafti, Shiang Fang, Madhav Ghimire, Ziqiang Wang, and Ilija Zeljkovic. Plethora of tunable Weyl fermions in kagome magnet Fe3Sn2 thin films, 2022.

[81] Liang Fu and C. L. Kane. Superconducting proximity effect and majorana fermions at the surface of a topological insulator. *Phys. Rev. Lett.*, 100:096407, Mar 2008.

[82] Mei-Xiao Wang, Canhua Liu, Jin-Peng Xu, Fang Yang, Lin Miao, Meng-Yu Yao, C. L. Gao, Chenyi Shen, Xucun Ma, X. Chen, Zhu-An Xu, Ying Liu, Shou-Cheng Zhang, Dong Qian, Jin-Feng Jia, and Qi-Kun Xue. The Coexistence of Superconductivity and Topological Order in the Bi2Se3 Thin Films. *Science*, 336(6077):52–55, 2012.

[83] Jin-Peng Xu, Canhua Liu, Mei-Xiao Wang, Jianfeng Ge, Zhi-Long Liu, Xiaojun Yang, Yan Chen, Ying Liu, Zhu-An Xu, Chun-Lei Gao, Dong Qian, Fu-Chun Zhang, and Jin-Feng Jia. Artificial topological superconductor by the proximity effect. *Phys. Rev. Lett.*, 112:217001, May 2014.

[84] Su-Yang Xu, Nasser Alidoust, Ilya Belopolski, Anthony Richardella, Chang Liu, Madhab Neupane, Guang Bian, Song-Hsun Huang, Raman Sankar, Chen Fang, Brian Dellabetta, Wenqing Dai, Qi Li, Matthew J. Gilbert, Fangcheng Chou, Nitin Samarth, and M. Zahid Hasan. Momentum-space imaging of cooper pairing in a half-dirac-gas topological superconductor. *Nature Physics*, 10(12):943–950, Dec 2014.

[85] Jin-Peng Xu, Mei-Xiao Wang, Zhi Long Liu, Jian-Feng Ge, Xiaojun Yang, Canhua Liu, Zhu An Xu, Dandan Guan, Chun Lei Gao, Dong Qian, Ying Liu, Qiang-Hua Wang, Fu-Chun Zhang, Qi-Kun Xue, and Jin-Feng Jia. Experimental Detection of a Majorana Mode in the core of a Magnetic Vortex inside a Topological Insulator-Superconductor $Bi_2Te_3/NbSe_2$ Heterostructure. *Phys. Rev. Lett.*, 114:017001, Jan 2015.

[86] Hao-Hua Sun, Kai-Wen Zhang, Lun-Hui Hu, Chuang Li, Guan-Yong Wang, Hai-Yang Ma, Zhu-An Xu, Chun-Lei Gao, Dan-Dan Guan, Yao-Yi Li, Canhua Liu, Dong Qian, Yi Zhou, Liang Fu, Shao-Chun Li, Fu-Chun Zhang, and Jin-Feng Jia. Majorana zero mode detected with spin selective andreev reflection in the vortex of a topological superconductor. *Phys. Rev. Lett.*, 116:257003, Jun 2016.

[87] Fan Yang, Yue Ding, Fanming Qu, Jie Shen, Jun Chen, Zhongchao Wei, Zhongqing Ji, Guangtong Liu, Jie Fan, Changli Yang, Tao Xiang, and Li Lu. Proximity effect at superconducting Sn-Bi_2Se_3 interface. *Phys. Rev. B*, 85:104508, Mar 2012.

[88] Fanming Qu, Fan Yang, Jie Shen, Yue Ding, Jun Chen, Zhongqing Ji, Guangtong Liu, Jie Fan, Xiunian Jing, Changli Yang, and Li Lu. Strong Superconducting Proximity Effect in Pb-Bi2Te3 Hybrid Structures. *Scientific Reports*, 2(1):339, Mar 2012.

[89] T. Yilmaz, I. Pletikosić, A. P. Weber, J. T. Sadowski, G. D. Gu, A. N. Caruso, B. Sinkovic, and T. Valla. Absence of a Proximity Effect for a Thin-Films of a Bi_2Se_3 Topological Insulator Grown on Top of a $Bi_2Sr_2CaCu_2O_{8+\delta}$ Cuprate Superconductor. *Phys. Rev. Lett.*, 113:067003, Aug 2014.

[90] Su-Yang Xu, Chang Liu, Anthony Richardella, I. Belopolski, N. Alidoust, M. Neupane, G. Bian, Nitin Samarth, and M. Z. Hasan. Fermi-level electronic structure of a topological-insulator/cuprate-superconductor based heterostructure in the superconducting proximity effect regime. *Phys. Rev. B*, 90:085128, Aug 2014.

[91] Parisa Zareapour, Alex Hayat, Shu Yang F. Zhao, Michael Kreshchuk, Achint Jain, Daniel C. Kwok, Nara Lee, Sang-Wook Cheong, Zhijun Xu, Alina Yang, G. D. Gu, Shuang Jia, Robert J. Cava, and Kenneth S. Burch. Proximity-induced high-temperature superconductivity in the topological insulators Bi2Se3 and Bi2Te3. *Nature Communications*, 3(1):1056, Sep 2012.

[92] Eryin Wang, Hao Ding, Alexei V. Fedorov, Wei Yao, Zhi Li, Yan-Feng Lv, Kun Zhao, Li-Guo Zhang, Zhijun Xu, John Schneeloch, Ruidan Zhong, Shuai-Hua Ji, Lili Wang, Ke He, Xucun Ma, Genda Gu, Hong Yao, Qi-Kun Xue, Xi Chen, and Shuyun Zhou. Fully gapped topological surface states in Bi2Se3 films induced by a d-wave high-temperature superconductor. *Nature Physics*, 9(10):621–625, Oct 2013.

[93] A.Y. Cho and J.R. Arthur. Molecular beam epitaxy. *Progress in Solid State Chemistry*, 10:157–191, 1975.

[94] Qi-Kun Xue, T. Hashizume, and T. Sakurai. Scanning tunneling microscopy of III-V compound semiconductor (001) surfaces. *Progress in Surface Science*, 56(1):1–131, 1997.

[95] Marian A Herman and Helmut Sitter. *Molecular beam epitaxy: fundamentals and current status*, volume 7. Springer Science & Business Media, 2012.

[96] Jeffrey Y Tsao. *Materials fundamentals of molecular beam epitaxy.* Academic Press, 2012.

[97] W. Patrick McCray. Mbe deserves a place in the history books. *Nature Nanotechnology*, 2(5):259–261, May 2007.

[98] K. G. Günther. Aufdampfschidhten aus halbleitenden III-V-Verbindungen. *Zeitschrift für Naturforschung A*, 13(12):1081–1089, 1958.

[99] D. C. Tsui, H. L. Stormer, and A. C. Gossard. Two-dimensional magnetotransport in the extreme quantum limit. *Phys. Rev. Lett.*, 48:1559–1562, May 1982.

[100] Cui-Zu Chang, Jinsong Zhang, Xiao Feng, Jie Shen, Zuocheng Zhang, Minghua Guo, Kang Li, Yunbo Ou, Pang Wei, Li-Li Wang, Zhong-Qing Ji, Yang Feng, Shuaihua Ji, Xi Chen, Jinfeng Jia, Xi Dai, Zhong Fang, Shou-Cheng Zhang, Ke He, Yayu Wang, Li Lu, Xu-Cun Ma, and Qi-Kun Xue. Experimental observation of the quantum anomalous hall effect in a magnetic topological insulator. *Science*, 340(6129):167–170, 2013.

[101] Qing-Yan Wang, Zhi Li, Wen-Hao Zhang, Zuo-Cheng Zhang, Jin-Song Zhang, Wei Li, Hao Ding, Yun-Bo Ou, Peng Deng, Kai Chang, Jing Wen, Can-Li Song, Ke He, Jin-Feng Jia, Shuai-Hua Ji, Ya-Yu Wang, Li-Li Wang, Xi Chen, Xu-Cun Ma, and Qi-Kun Xue. Interface-Induced High-Temperature Superconductivity in Single Unit-Cell FeSe Films on $SrTiO_3$. *Chinese Physics Letters*, 29(3):037402, mar 2012.

[102] G. Binnig, H. Rohrer, Ch. Gerber, and E. Weibel. Surface studies by scanning tunneling microscopy. *Phys. Rev. Lett.*, 49:57–61, Jul 1982.

[103] J. Bardeen. Tunnelling from a many-particle point of view. *Phys. Rev. Lett.*, 6:57–59, Jan 1961.

[104] S. Kasahara, H. J. Shi, K. Hashimoto, S. Tonegawa, Y. Mizukami, T. Shibauchi, K. Sugimoto, T. Fukuda, T. Terashima, Andriy H. Nevidomskyy, and Y. Matsuda. Electronic nematicity above the structural and superconducting transition in BaFe2(As1-xPx)2. *Nature*, 486(7403):382–385, Jun 2012.

[105] Matthias Vojta. Lattice symmetry breaking in cuprate superconductors: stripes, nematics, and superconductivity. *Advances in Physics*, 58(6):699–820, 2009.

[106] Youichi Yamakawa, Seiichiro Onari, and Hiroshi Kontani. Nematicity and Magnetism in FeSe and Other Families of Fe-Based Superconductors. *Phys. Rev. X*, 6:021032, Jun 2016.

[107] Kun Jiang, Jiangping Hu, Hong Ding, and Ziqiang Wang. Interatomic Coulomb interaction and electron nematic bond order in FeSe. *Phys. Rev. B*, 93:115138, Mar 2016.

[108] Jiun-Haw Chu, James G. Analytis, Kristiaan De Greve, Peter L. McMahon, Zahirul Islam, Yoshihisa Yamamoto, and Ian R. Fisher. In-plane resistivity anisotropy in an underdoped iron arsenide superconductor. *Science*, 329(5993):824–826, 2010.

[109] Jiun-Haw Chu, Hsueh-Hui Kuo, James G. Analytis, and Ian R. Fisher. Divergent nematic susceptibility in an iron arsenide superconductor. *Science*, 337(6095):710–712, 2012.

[110] M. A. Tanatar, A. E. Böhmer, E. I. Timmons, M. Schütt, G. Drachuck, V. Taufour, K. Kothapalli, A. Kreyssig, S. L. Bud'ko, P. C. Canfield, R. M. Fernandes, and R. Prozorov. Origin of the Resistivity Anisotropy in the Nematic Phase of FeSe. *Phys. Rev. Lett.*, 117:127001, Sep 2016.

[111] T. Shimojima, Y. Suzuki, T. Sonobe, A. Nakamura, M. Sakano, J. Omachi, K. Yoshioka, M. Kuwata-Gonokami, K. Ono, H. Kumigashira, A. E. Böhmer, F. Hardy, T. Wolf, C. Meingast, H. v. Löhneysen, H. Ikeda, and K. Ishizaka. Lifting of xz/yz orbital degeneracy at the structural transition in detwinned FeSe. *Phys. Rev. B*, 90:121111, Sep 2014.

[112] K. Nakayama, Y. Miyata, G. N. Phan, T. Sato, Y. Tanabe, T. Urata, K. Tanigaki, and T. Takahashi. Reconstruction of Band Structure Induced by Electronic Nematicity in an FeSe Superconductor. *Phys. Rev. Lett.*, 113:237001, Dec 2014.

[113] P. Zhang, T. Qian, P. Richard, X. P. Wang, H. Miao, B. Q. Lv, B. B. Fu, T. Wolf, C. Meingast, X. X. Wu, Z. Q. Wang, J. P. Hu, and H. Ding. Observation of two distinct d_{xz}/d_{yz} band splittings in FeSe. *Phys. Rev. B*, 91:214503, Jun 2015.

[114] M. Yi, H. Pfau, Y. Zhang, Y. He, H. Wu, T. Chen, Z. R. Ye, M. Hashimoto, R. Yu, Q. Si, D.-H. Lee, Pengcheng Dai, Z.-X. Shen, D. H. Lu, and R. J. Birgeneau. Nematic Energy Scale and the Missing Electron Pocket in FeSe. *Phys. Rev. X*, 9:041049, Dec 2019.

[115] Ming Yi, Donghui Lu, Jiun-Haw Chu, James G. Analytis, Adam P. Sorini, Alexander F. Kemper, Brian Moritz, Sung-Kwan Mo, Rob G. Moore, Makoto Hashimoto, Wei-Sheng Lee, Zahid Hussain, Thomas P. Devereaux, Ian R. Fisher, and Zhi-Xun Shen. Symmetry-breaking orbital anisotropy observed for detwinned Ba(Fe1-xCox)2As2 above the spin density wave transition. *Proceedings of the National Academy of Sciences*, 108(17):6878–6883, 2011.

[116] E. P. Rosenthal, E. F. Andrade, C. J. Arguello, R. M. Fernandes, L. Y. Xing, X. C. Wang, C. Q. Jin, A. J. Millis, and A. N. Pasupathy. Visualization of electron nematicity and unidirectional antiferroic fluctuations at high temperatures in NaFeAs. *Nature Physics*, 10(3):225–232, Mar 2014.

[117] A. Kostin, P. O. Sprau, A. Kreisel, Yi Xue Chong, A. E. Bohmer, P. C. Canfield, P. J. Hirschfeld, B. M. Andersen, and J. C. Séamus Davis. Imaging orbital-selective quasiparticles in the Hund's metal state of FeSe. *Nature Materials*, 17(10):869–874, Oct 2018.

[118] Anna E Böhmer and Andreas Kreisel. Nematicity, magnetism and superconductivity in FeSe. *Journal of Physics: Condensed Matter*, 30(2):023001, dec 2017.

[119] Zheng Ren, Hong Li, He Zhao, Shrinkhala Sharma, Ziqiang Wang, and Ilija Zeljkovic. Nanoscale decoupling of electronic nematicity and structural anisotropy in FeSe thin films. *Nature Communications*, 12(1):10, Jan 2021.

[120] Dennis Huang, Can-Li Song, Tatiana A. Webb, Shiang Fang, Cui-Zu Chang, Jagadeesh S. Moodera, Efthimios Kaxiras, and Jennifer E. Hoffman. Revealing the Empty-State Electronic Structure of Single-Unit-Cell FeSe/$SrTiO_3$. *Phys. Rev. Lett.*, 115:017002, Jul 2015.

[121] Wen-Hao Zhang, Yi Sun, Jin-Song Zhang, Fang-Sen Li, Ming-Hua Guo, Yan-Fei Zhao, Hui-Min Zhang, Jun-Ping Peng, Ying Xing, Hui-Chao Wang, Takeshi Fujita, Akihiko Hirata, Zhi Li, Hao Ding, Chen-Jia Tang, Meng Wang, Qing-Yan Wang, Ke He, Shuai-Hua Ji, Xi Chen, Jun-Feng Wang, Zheng-Cai Xia, Liang Li, Ya-Yu Wang, Jian Wang, Li-Li Wang, Ming-Wei Chen, Qi-Kun Xue, and Xu-Cun Ma. Direct Observation of High-Temperature Superconductivity in One-Unit-Cell FeSe Films. *Chinese Physics Letters*, 31(1):017401, jan 2014.

[122] Ke Zou, Subhasish Mandal, Stephen D. Albright, Rui Peng, Yujia Pu, Divine Kumah, Claudia Lau, Georg H. Simon, Omur E. Dagdeviren, Xi He, Ivan Božović, Udo D. Schwarz, Eric I. Altman, Donglai Feng, Fred J. Walker, Sohrab Ismail-Beigi, and Charles H. Ahn. Role of double TiO_2 layers at the interface of FeSe/$SrTiO_3$ superconductors. *Phys. Rev. B*, 93:180506, May 2016.

[123] Shiyong Tan, Yan Zhang, Miao Xia, Zirong Ye, Fei Chen, Xin Xie, Rui Peng, Difei Xu, Qin Fan, Haichao Xu, Juan Jiang, Tong Zhang, Xinchun Lai, Tao Xiang, Jiangping Hu, Binping Xie, and Donglai Feng. Interface-induced superconductivity and

strain-dependent spin density waves in FeSe/$SrTiO_3$ thin films. *Nature Materials*, 12(7):634–640, Jul 2013.

[124] J. J. Lee, F. T. Schmitt, R. G. Moore, S. Johnston, Y.-T. Cui, W. Li, M. Yi, Z. K. Liu, M. Hashimoto, Y. Zhang, D. H. Lu, T. P. Devereaux, D.-H. Lee, and Z.-X. Shen. Interfacial mode coupling as the origin of the enhancement of Tc in FeSe films on $SrTiO_3$. *Nature*, 515(7526):245–248, Nov 2014.

[125] Q. Fan, W. H. Zhang, X. Liu, Y. J. Yan, M. Q. Ren, R. Peng, H. C. Xu, B. P. Xie, J. P. Hu, T. Zhang, and D. L. Feng. Plain s-wave superconductivity in single-layer FeSe on $SrTiO_3$ probed by scanning tunnelling microscopy. *Nature Physics*, 11(11):946–952, Nov 2015.

[126] Junhyeok Bang, Zhi Li, Y. Y. Sun, Amit Samanta, Y. Y. Zhang, Wenhao Zhang, Lili Wang, X. Chen, Xucun Ma, Q.-K. Xue, and S. B. Zhang. Atomic and electronic structures of single-layer FeSe on $SrTiO_3$(001): The role of oxygen deficiency. *Phys. Rev. B*, 87:220503, Jun 2013.

[127] Rui Peng, Ke Zou, M. G. Han, Stephen D. Albright, Hawoong Hong, Claudia Lau, H. C. Xu, Yimei Zhu, F. J. Walker, and C. H. Ahn. Picoscale structural insight into superconductivity of monolayer FeSe/$SrTiO_3$. *Science Advances*, 6(15), 2020.

[128] Zheng Ren and Ilija Zeljkovic. https://doi.org/10.5281/zenodo.4725825, April 2021.

[129] Xu Liu, Defa Liu, Wenhao Zhang, Junfeng He, Lin Zhao, Shaolong He, Daixiang Mou, Fangsen Li, Chenjia Tang, Zhi Li, Lili Wang, Yingying Peng, Yan Liu, Chaoyu Chen, Li Yu, Guodong Liu, Xiaoli Dong, Jun Zhang, Chuangtian Chen, Zuyan Xu, Xi Chen, Xucun Ma, Qikun Xue, and X. J. Zhou. Dichotomy of the electronic structure and superconductivity between single-layer and double-layer FeSe/$SrTiO_3$ films. *Nature Communications*, 5(1):5047, Sep 2014.

[130] M. J. Lawler, K. Fujita, Jhinhwan Lee, A. R. Schmidt, Y. Kohsaka, Chung Koo Kim, H. Eisaki, S. Uchida, J. C. Davis, J. P. Sethna, and Eun-Ah Kim. Intra-unit-cell electronic nematicity of the high-Tc copper-oxide pseudogap states. *Nature*, 466(7304):347–351, Jul 2010.

[131] Ilija Zeljkovic, Jouko Nieminen, Dennis Huang, Tay-Rong Chang, Yang He, Horng-Tay Jeng, Zhijun Xu, Jinsheng Wen, Genda Gu, Hsin Lin, Robert S. Markiewicz, Arun Bansil, and Jennifer E. Hoffman. Nanoscale Interplay of Strain and Doping in a High-Temperature Superconductor. *Nano Letters*, 14(12):6749–6753, Dec 2014.

[132] Ilija Zeljkovic, Daniel Walkup, Badih A. Assaf, Kane L. Scipioni, R. Sankar, Fangcheng Chou, and Vidya Madhavan. Strain engineering Dirac surface states in heteroepitaxial topological crystalline insulator thin films. *Nature Nanotechnology*, 10(10):849–853, Oct 2015.

[133] Shang Gao, Felix Flicker, Raman Sankar, He Zhao, Zheng Ren, Bryan Rachmilowitz, Sidhika Balachandar, Fangcheng Chou, Kenneth S. Burch, Ziqiang Wang, Jasper van Wezel, and Ilija Zeljkovic. Atomic-scale strain manipulation of a charge density wave. *Proceedings of the National Academy of Sciences*, 115(27):6986–6990, 2018.

[134] Daniel Walkup, Badih A. Assaf, Kane L. Scipioni, R. Sankar, Fangcheng Chou, Guoqing Chang, Hsin Lin, Ilija Zeljkovic, and Vidya Madhavan. Interplay of orbital effects and nanoscale strain in topological crystalline insulators. *Nature Communications*, 9(1):1550, Apr 2018.

[135] G. Springholz and K. Wiesauer. Nanoscale Dislocation Patterning in PbTe/PbSe(001) Lattice-Mismatched Heteroepitaxy. *Phys. Rev. Lett.*, 88:015507, Dec 2001.

[136] Robert Hull and John C. Bean. Misfit dislocations in lattice-mismatched epitaxial films. *Critical Reviews in Solid State and Materials Sciences*, 17(6):507–546, 1992.

[137] John Price Hirth and Jens Lothe. *Theory of Dislocations*. Krieger Publishing Company, 1992.

[138] G. Springholz. Strain contrast in scanning tunneling microscopy imaging of subsurface dislocations in lattice-mismatched heteroepitaxy. *Applied Surface Science*, 112:12–22, 1997.

[139] Zheng Ren, Hong Li, He Zhao, Shrinkhala Sharma, Ziqiang Wang, and Ilija Zeljkovic. http://doi.org/10.5281/zenodo.4273119, November 2020.

[140] T.-M. Chuang, M. P. Allan, Jinho Lee, Yang Xie, Ni Ni, S. L. Bud'ko, G. S. Boebinger, P. C. Canfield, and J. C. Davis. Nematic Electronic Structure in the "Parent" State of the Iron-Based Superconductor $Ca(Fe_{1-x}Co_x)_2As_2$. *Science*, 327(5962):181–184, 2010.

[141] E. P. Rosenthal, E. F. Andrade, C. J. Arguello, R. M. Fernandes, L. Y. Xing, X. C. Wang, C. Q. Jin, A. J. Millis, and A. N. Pasupathy. Visualization of electron nematicity and unidirectional antiferroic fluctuations at high temperatures in NaFeAs. *Nature Physics*, 10(3):225–232, Mar 2014.

[142] Erick F. Andrade, Ayelet Notis Berger, Ethan P. Rosenthal, Xiaoyu Wang, Lingyi Xing, Xiancheng Wang, Changqing Jin, Rafael M. Fernandes, Andrew J. Millis, and Abhay N. Pasupathy. Visualizing the Nonlinear Coupling between Strain and Electronic Nematicity in the Iron Pnictides by Elasto-Scanning Tunneling Spectroscopy, 2018.

[143] A. Kostin, P. O. Sprau, A. Kreisel, Yi Xue Chong, A. E. Böhmer, P. C. Canfield, P. J. Hirschfeld, B. M. Andersen, and J. C. Séamus Davis. Imaging orbital-selective quasiparticles in the Hund's metal state of FeSe. *Nature Materials*, 17(10):869–874, Oct 2018.

[144] P. O. Sprau, A. Kostin, A. Kreisel, A. E. Böhmer, V. Taufour, P. C. Canfield, S. Mukherjee, P. J. Hirschfeld, B. M. Andersen, and J. C. Séamus Davis. Discovery of orbital-selective Cooper pairing in FeSe. *Science*, 357(6346):75–80, 2017.

[145] He Zhao, Hong Li, Lianyang Dong, Binjie Xu, John Schneeloch, Ruidan Zhong, Minghu Fang, Genda Gu, John Harter, Stephen D. Wilson, Ziqiang Wang, and Ilija Zeljkovic. Nematic transition and nanoscale suppression of superconductivity in Fe(Te,Se). *Nature Physics*, Jun 2021.

[146] Wei Li, Yan Zhang, Peng Deng, Zhilin Xu, S.-K. Mo, Ming Yi, Hao Ding, M. Hashimoto, R. G. Moore, D.-H. Lu, Xi Chen, Z.-X. Shen, and Qi-Kun Xue. Stripes developed at the strong limit of nematicity in FeSe film. *Nature Physics*, 13(10):957–961, Oct 2017.

[147] Yonghao Yuan, Wei Li, Bin Liu, Peng Deng, Zhilin Xu, Xi Chen, Canli Song, Lili Wang, Ke He, Gang Xu, Xucun Ma, and Qi-Kun Xue. Edge States at Nematic Domain Walls in FeSe Films. *Nano Letters*, 18(11):7176–7180, Nov 2018.

[148] R. Prozorov, M. A. Tanatar, N. Ni, A. Kreyssig, S. Nandi, S. L. Bud'ko, A. I. Goldman, and P. C. Canfield. Intrinsic pinning on structural domains in underdoped single crystals of $Ba(Fe_{1-x}Co_x)_2As_2$. *Phys. Rev. B*, 80:174517, Nov 2009.

[149] Jiun-Haw Chu, Hsueh-Hui Kuo, James G. Analytis, and Ian R. Fisher. Divergent Nematic Susceptibility in an Iron Arsenide Superconductor. *Science*, 337(6095):710–712, 2012.

[150] J. W. Matthews. Defects associated with the accommodation of misfit between crystals. *Journal of Vacuum Science and Technology*, 12(1):126–133, 1975.

[151] S. Chandra and A.K.M.A. Islam. Elastic properties of mono- and poly-crystalline PbO-type $FeSe_{1\text{-}x}Te_x$ (x=0–1.0): A first-principles study. *Physica C: Superconductivity*, 470(22):2072–2075, 2010.

[152] P. O. Sprau, A. Kostin, A. Kreisel, A. E. Böhmer, V. Taufour, P. C. Canfield, S. Mukherjee, P. J. Hirschfeld, B. M. Andersen, and J. C. Séamus Davis. Discovery of orbital-selective Cooper pairing in FeSe. *Science*, 357(6346):75–80, 2017.

[153] M. D. Watson, T. K. Kim, A. A. Haghighirad, N. R. Davies, A. McCollam, A. Narayanan, S. F. Blake, Y. L. Chen, S. Ghannadzadeh, A. J. Schofield, M. Hoesch, C. Meingast, T. Wolf, and A. I. Coldea. Emergence of the nematic electronic state in FeSe. *Phys. Rev. B*, 91:155106, Apr 2015.

[154] Suguru Hosoi, Kohei Matsuura, Kousuke Ishida, Hao Wang, Yuta Mizukami, Tatsuya Watashige, Shigeru Kasahara, Yuji Matsuda, and Takasada Shibauchi. Nematic quantum critical point without magnetism in FeSe1-xSx superconductors. *Proceedings of the National Academy of Sciences*, 113(29):8139–8143, 2016.

[155] Fong-Chi Hsu, Jiu-Yong Luo, Kuo-Wei Yeh, Ta-Kun Chen, Tzu-Wen Huang, Phillip M. Wu, Yong-Chi Lee, Yi-Lin Huang, Yan-Yi Chu, Der-Chung Yan, and Maw-Kuen Wu. Superconductivity in the PbO-type structure α-FeSe. *Proceedings of the National Academy of Sciences*, 105(38):14262–14264, 2008.

[156] R. M. Fernandes, A. V. Chubukov, and J. Schmalian. What drives nematic order in iron-based superconductors? *Nature Physics*, 10(2):97–104, Feb 2014.

[157] M. Z. Hasan and C. L. Kane. Colloquium: Topological insulators. *Rev. Mod. Phys.*, 82:3045–3067, Nov 2010.

[158] Xiao-Liang Qi and Shou-Cheng Zhang. Topological insulators and superconductors. *Rev. Mod. Phys.*, 83:1057–1110, Oct 2011.

[159] Haijun Zhang, Chao-Xing Liu, Xiao-Liang Qi, Xi Dai, Zhong Fang, and Shou-Cheng Zhang. Topological insulators in Bi2Se3, Bi2Te3 and Sb2Te3 with a single Dirac cone on the surface. *Nature Physics*, 5(6):438–442, Jun 2009.

[160] Xiao-Liang Qi, Taylor L. Hughes, and Shou-Cheng Zhang. Topological field theory of time-reversal invariant insulators. *Phys. Rev. B*, 78:195424, Nov 2008.

[161] Y. L. Chen, J.-H. Chu, J. G. Analytis, Z. K. Liu, K. Igarashi, H.-H. Kuo, X. L. Qi, S. K. Mo, R. G. Moore, D. H. Lu, M. Hashimoto, T. Sasagawa, S. C. Zhang, I. R. Fisher, Z. Hussain, and Z. X. Shen. Massive dirac fermion on the surface of a magnetically doped topological insulator. *Science*, 329(5992):659–662, 2010.

[162] Rui Yu, Wei Zhang, Hai-Jun Zhang, Shou-Cheng Zhang, Xi Dai, and Zhong Fang. Quantized anomalous hall effect in magnetic topological insulators. *Science*, 329(5987):61–64, 2010.

[163] Yujun Deng, Yijun Yu, Meng Zhu Shi, Zhongxun Guo, Zihan Xu, Jing Wang, Xian Hui Chen, and Yuanbo Zhang. Quantum anomalous Hall effect in intrinsic magnetic topological insulator MnBi2Te4. *Science*, 367(6480):895–900, 2020.

[164] M. Serlin, C. L. Tschirhart, H. Polshyn, Y. Zhang, J. Zhu, K. Watanabe, T. Taniguchi, L. Balents, and A. F. Young. Intrinsic quantized anomalous hall effect in a moire heterostructure. *Science*, 367(6480):900–903, 2020.

[165] Guanhua Zhang, Huajun Qin, Jing Teng, Jiandong Guo, Qinlin Guo, Xi Dai, Zhong Fang, and Kehui Wu. Quintuple-layer epitaxy of thin films of topological insulator Bi2Se3. *Applied Physics Letters*, 95(5):053114, 2009.

[166] Can-Li Song, Yi-Lin Wang, Ye-Ping Jiang, Yi Zhang, Cui-Zu Chang, Lili Wang, Ke He, Xi Chen, Jin-Feng Jia, Yayu Wang, Zhong Fang, Xi Dai, Xin-Cheng Xie, Xiao-Liang Qi, Shou-Cheng Zhang, Qi-Kun Xue, and Xucun Ma. Topological insulator Bi2Se3 thin films grown on double-layer graphene by molecular beam epitaxy. *Applied Physics Letters*, 97(14):143118, 2010.

[167] Yi Zhang, Ke He, Cui-Zu Chang, Can-Li Song, Li-Li Wang, Xi Chen, Jin-Feng Jia, Zhong Fang, Xi Dai, Wen-Yu Shan, Shun-Qing Shen, Qian Niu, Xiao-Liang Qi, Shou-Cheng Zhang, Xu-Cun Ma, and Qi-Kun Xue. Crossover of the three-dimensional topological insulator Bi2Se3 to the two-dimensional limit. *Nature Physics*, 6(8):584–588, Aug 2010.

[168] Guanhua Zhang, Huajun Qin, Jun Chen, Xiaoyue He, Li Lu, Yongqing Li, and Kehui Wu. Growth of Topological Insulator Bi2Se3 Thin Films on SrTiO3 with Large Tunability in Chemical Potential. *Advanced Functional Materials*, 21(12):2351–2355, 2011.

[169] S. E. Harrison, S. Li, Y. Huo, B. Zhou, Y. L. Chen, and J. S. Harris. Two-step growth of high quality Bi2Te3 thin films on Al2O3 (0001) by molecular beam epitaxy. *Applied Physics Letters*, 102(17):171906, 2013.

[170] Phuoc Huu Le, Kaung Hsiung Wu, Chih Wei Luo, and Jihperng Leu. Growth and characterization of topological insulator Bi2Se3 thin films on SrTiO3 using pulsed laser deposition. *Thin Solid Films*, 534:659–665, 2013.

[171] Polychronis Tsipas, Evangelia Xenogiannopoulou, Spyridon Kassavetis, Dimitra Tsoutsou, Evangelos Golias, Calliope Bazioti, George P. Dimitrakopulos, Philomela Komninou, Hu Liang, Matty Caymax, and Athanasios Dimoulas. Observation of Surface Dirac Cone in High-Quality Ultrathin Epitaxial Bi2Se3 Topological Insulator on AlN(0001) Dielectric. *ACS Nano*, 8(7):6614–6619, Jul 2014.

[172] C. Bigi, P. Orgiani, A. Nardi, A. Troglia, J. Fujii, G. Panaccione, I. Vobornik, and G. Rossi. Robustness of topological states in Bi2Se3 thin film grown by Pulsed Laser Deposition on (001)-oriented SrTiO3 perovskite. *Applied Surface Science*, 473:190–193, 2019.

[173] Yao-Yi Li, Guang Wang, Xie-Gang Zhu, Min-Hao Liu, Cun Ye, Xi Chen, Ya-Yu Wang, Ke He, Li-Li Wang, Xu-Cun Ma, Hai-Jun Zhang, Xi Dai, Zhong Fang, Xin-Cheng Xie, Ying Liu, Xiao-Liang Qi, Jin-Feng Jia, Shou-Cheng Zhang, and Qi-Kun Xue. Intrinsic Topological Insulator Bi2Te3 Thin Films on Si and Their Thickness Limit. *Advanced Materials*, 22(36):4002–4007, 2010.

[174] Michael M. Yee, Z.-H. Zhu, Anjan Soumyanarayanan, Yang He, Can-Li Song, Ekaterina Pomjakushina, Zaher Salman, Amit Kanigel, Kouji Segawa, Yoichi Ando, and Jennifer E. Hoffman. Spin-polarized quantum well states on $Bi_{2-x}Fe_xSe_3$. *Phys. Rev. B*, 91:161306, Apr 2015.

[175] Evelyn Tang, Jia-Wei Mei, and Xiao-Gang Wen. High-temperature fractional quantum hall states. *Phys. Rev. Lett.*, 106:236802, Jun 2011.

[176] Tomonari Mizoguchi and Masafumi Udagawa. Flat-band engineering in tight-binding models: Beyond the nearest-neighbor hopping. *Phys. Rev. B*, 99:235118, Jun 2019.

[177] H.-M. Guo and M. Franz. Topological insulator on the kagome lattice. *Phys. Rev. B*, 80:113102, Sep 2009.

[178] I. I. Mazin, Harald O. Jeschke, Frank Lechermann, Hunpyo Lee, Mario Fink, Ronny Thomale, and Roser Valentí. Theoretical prediction of a strongly correlated dirac metal. *Nature Communications*, 5(1):4261, Jul 2014.

[179] Aaron L. Sharpe, Eli J. Fox, Arthur W. Barnard, Joe Finney, Kenji Watanabe, Takashi Taniguchi, M. A. Kastner, and David Goldhaber-Gordon. Emergent ferromagnetism near three-quarters filling in twisted bilayer graphene. *Science*, 365(6453):605–608, 2019.

[180] Linda Ye, Shiang Fang, Min Gu Kang, Josef Kaufmann, Yonghun Lee, Jonathan Denlinger, Chris Jozwiak, Aaron Bostwick, Eli Rotenberg, Efthimios Kaxiras, David C. Bell, Oleg Janson, Riccardo Comin, and Joseph G. Checkelsky. A flat band-induced correlated kagome metal, 2021.

[181] He Zhao, Hong Li, Brenden R. Ortiz, Samuel M. L. Teicher, Takamori Park, Mengxing Ye, Ziqiang Wang, Leon Balents, Stephen D. Wilson, and Ilija Zeljkovic. Cascade of correlated electron states in the kagome superconductor CsV3Sb5. *Nature*, 599(7884):216–221, Nov 2021.

[182] Yu-Xiao Jiang, Jia-Xin Yin, M. Michael Denner, Nana Shumiya, Brenden R. Ortiz, Gang Xu, Zurab Guguchia, Junyi He, Md Shafayat Hossain, Xiaoxiong Liu, Jacob Ruff, Linus Kautzsch, Songtian S. Zhang, Guoqing Chang, Ilya Belopolski, Qi Zhang, Tyler A. Cochran, Daniel Multer, Maksim Litskevich, Zi-Jia Cheng, Xian P. Yang, Ziqiang Wang, Ronny Thomale, Titus Neupert, Stephen D. Wilson, and M. Zahid Hasan. Unconventional chiral charge order in kagome superconductor KV3Sb5. *Nature Materials*, 20(10):1353–1357, Oct 2021.

[183] Hong Li, He Zhao, Brenden R. Ortiz, Takamori Park, Mengxing Ye, Leon Balents, Ziqiang Wang, Stephen D. Wilson, and Ilija Zeljkovic. Rotation symmetry breaking in the normal state of a kagome superconductor KV3Sb5. *Nature Physics*, 18(3):265–270, Mar 2022.

[184] Linpeng Nie, Kuanglv Sun, Wanru Ma, Dianwu Song, Lixuan Zheng, Zuowei Liang, Ping Wu, Fanghang Yu, Jian Li, Min Shan, Dan Zhao, Shunjiao Li, Baolei Kang, Zhimian Wu, Yanbing Zhou, Kai Liu, Ziji Xiang, Jianjun Ying, Zhenyu Wang, Tao Wu, and Xianhui Chen. Charge-density-wave-driven electronic nematicity in a kagome superconductor. *Nature*, 604(7904):59–64, Apr 2022.

[185] C. Mielke, D. Das, J.-X. Yin, H. Liu, R. Gupta, Y.-X. Jiang, M. Medarde, X. Wu, H. C. Lei, J. Chang, Pengcheng Dai, Q. Si, H. Miao, R. Thomale, T. Neupert, Y. Shi, R. Khasanov, M. Z. Hasan, H. Luetkens, and Z. Guguchia. Time-reversal symmetry-breaking charge order in a kagome superconductor. *Nature*, 602(7896):245–250, Feb 2022.

[186] Han-Shu Xu, Ya-Jun Yan, Ruotong Yin, Wei Xia, Shijie Fang, Ziyuan Chen, Yuanji Li, Wenqi Yang, Yanfeng Guo, and Dong-Lai Feng. Multiband Superconductivity with Sign-Preserving Order Parameter in Kagome Superconductor CsV_3Sb_5. *Phys. Rev. Lett.*, 127:187004, Oct 2021.

[187] Hui Chen, Haitao Yang, Bin Hu, Zhen Zhao, Jie Yuan, Yuqing Xing, Guojian Qian, Zihao Huang, Geng Li, Yuhan Ye, Sheng Ma, Shunli Ni, Hua Zhang, Qiangwei Yin, Chunsheng Gong, Zhijun Tu, Hechang Lei, Hengxin Tan, Sen Zhou, Chengmin Shen, Xiaoli Dong, Binghai Yan, Ziqiang Wang, and Hong-Jun Gao. Roton pair density wave in a strong-coupling kagome superconductor. *Nature*, 599(7884):222–228, Nov 2021.

[188] Zuowei Liang, Xingyuan Hou, Fan Zhang, Wanru Ma, Ping Wu, Zongyuan Zhang, Fanghang Yu, J.-J. Ying, Kun Jiang, Lei Shan, Zhenyu Wang, and X.-H. Chen. Three-Dimensional Charge Density Wave and Surface-Dependent Vortex-Core States in a Kagome Superconductor CsV_3Sb_5. *Phys. Rev. X*, 11:031026, Aug 2021.

[189] Shuo-Ying Yang, Yaojia Wang, Brenden R. Ortiz, Defa Liu, Jacob Gayles, Elena Derunova, Rafael Gonzalez-Hernandez, Libor Šmejkal, Yulin Chen, Stuart S. P. Parkin, Stephen D. Wilson, Eric S. Toberer, Tyrel McQueen, and Mazhar N. Ali. Giant, unconventional anomalous Hall effect in the metallic frustrated magnet candidate, KV3Sb5. *Science Advances*, 6(31):eabb6003, 2020.

[190] Ying Xiang, Qing Li, Yongkai Li, Wei Xie, Huan Yang, Zhiwei Wang, Yugui Yao, and Hai-Hu Wen. Twofold symmetry of c-axis resistivity in topological kagome superconductor CsV3Sb5 with in-plane rotating magnetic field. *Nature Communications*, 12(1):6727, Nov 2021.

[191] Hailan Luo, Qiang Gao, Hongxiong Liu, Yuhao Gu, Dingsong Wu, Changjiang Yi, Junjie Jia, Shilong Wu, Xiangyu Luo, Yu Xu, Lin Zhao, Qingyan Wang, Hanqing Mao, Guodong Liu, Zhihai Zhu, Youguo Shi, Kun Jiang, Jiangping Hu, Zuyan Xu, and X. J. Zhou. Electronic nature of charge density wave and electron-phonon coupling in kagome superconductor KV3Sb5. *Nature Communications*, 13(1):273, Jan 2022.

[192] Mingu Kang, Shiang Fang, Jeong-Kyu Kim, Brenden R. Ortiz, Sae Hee Ryu, Jimin Kim, Jonggyu Yoo, Giorgio Sangiovanni, Domenico Di Sante, Byeong-Gyu Park, Chris Jozwiak, Aaron Bostwick, Eli Rotenberg, Efthimios Kaxiras, Stephen D. Wilson, Jae-Hoon Park, and Riccardo Comin. Twofold van Hove singularity and origin of charge order in topological kagome superconductor CsV3Sb5. *Nature Physics*, 18(3):301–308, Mar 2022.

[193] Mingu Kang, Linda Ye, Shiang Fang, Jhih-Shih You, Abe Levitan, Minyong Han, Jorge I. Facio, Chris Jozwiak, Aaron Bostwick, Eli Rotenberg, Mun K. Chan, Ross D. McDonald, David Graf, Konstantine Kaznatcheev, Elio Vescovo, David C. Bell, Efthimios Kaxiras, Jeroen van den Brink, Manuel Richter, Madhav Prasad Ghimire, Joseph G. Checkelsky, and Riccardo Comin. Dirac fermions and flat bands in the ideal kagome metal FeSn. *Nature Materials*, 19(2):163–169, Feb 2020.

[194] Linda Ye, Mingu Kang, Junwei Liu, Felix von Cube, Christina R. Wicker, Takehito Suzuki, Chris Jozwiak, Aaron Bostwick, Eli Rotenberg, David C. Bell, Liang Fu, Riccardo Comin, and Joseph G. Checkelsky. Massive dirac fermions in a ferromagnetic kagome metal. *Nature*, 555(7698):638–642, Mar 2018.

[195] Mingu Kang, Shiang Fang, Linda Ye, Hoi Chun Po, Jonathan Denlinger, Chris Jozwiak, Aaron Bostwick, Eli Rotenberg, Efthimios Kaxiras, Joseph G. Checkelsky, and Riccardo Comin. Topological flat bands in frustrated kagome lattice CoSn. *Nature Communications*, 11(1):4004, Aug 2020.

[196] Gang Xu, Biao Lian, and Shou-Cheng Zhang. Intrinsic Quantum Anomalous Hall Effect in the Kagome Lattice $Cs_2LiMn_3F_{12}$. *Phys. Rev. Lett.*, 115:186802, Oct 2015.

[197] Jia-Xin Yin, Wenlong Ma, Tyler A. Cochran, Xitong Xu, Songtian S. Zhang, Hung-Ju Tien, Nana Shumiya, Guangming Cheng, Kun Jiang, Biao Lian, Zhida Song, Guoqing Chang, Ilya Belopolski, Daniel Multer, Maksim Litskevich, Zi-Jia Cheng, Xian P. Yang, Bianca Swidler, Huibin Zhou, Hsin Lin, Titus Neupert, Ziqiang Wang, Nan Yao, Tay-Rong Chang, Shuang Jia, and M. Zahid Hasan. Quantum-limit Chern topological magnetism in TbMn6Sn6. *Nature*, 583(7817):533–536, Jul 2020.

[198] Yonglong Xie, Andrew T. Pierce, Jeong Min Park, Daniel E. Parker, Eslam Khalaf, Patrick Ledwith, Yuan Cao, Seung Hwan Lee, Shaowen Chen, Patrick R. Forrester, Kenji Watanabe, Takashi Taniguchi, Ashvin Vishwanath, Pablo Jarillo-Herrero, and Amir Yacoby. Fractional chern insulators in magic-angle twisted bilayer graphene. *Nature*, 600(7889):439–443, Dec 2021.

[199] Hong Li, He Zhao, Qiangwei Yin, Qi Wang, Zheng Ren, Shrinkhala Sharma, Hechang Lei, Ziqiang Wang, and Ilija Zeljkovic. Spin-polarized imaging of the antiferromagnetic structure and field-tunable bound states in kagome magnet FeSn, 2022.

[200] Subir Sachdev. Kagome´- and triangular-lattice heisenberg antiferromagnets: Ordering from quantum fluctuations and quantum-disordered ground states with unconfined bosonic spinons. *Phys. Rev. B*, 45:12377–12396, Jun 1992.

[201] Thomas Bilitewski and Roderich Moessner. Disordered flat bands on the kagome lattice. *Phys. Rev. B*, 98:235109, Dec 2018.

[202] Titus Neupert, Luiz Santos, Claudio Chamon, and Christopher Mudry. Fractional quantum hall states at zero magnetic field. *Phys. Rev. Lett.*, 106:236804, Jun 2011.

[203] Kai Sun, Zhengcheng Gu, Hosho Katsura, and S. Das Sarma. Nearly flatbands with nontrivial topology. *Phys. Rev. Lett.*, 106:236803, Jun 2011.

[204] L. Balents, M. P. A. Fisher, and S. M. Girvin. Fractionalization in an easy-axis kagome antiferromagnet. *Phys. Rev. B*, 65:224412, May 2002.

[205] Simeng Yan, David A. Huse, and Steven R. White. Spin-Liquid Ground State of the S = 1/2 Kagome Heisenberg Antiferromagnet. *Science*, 332(6034):1173–1176, 2011.

[206] Leon Balents. Spin liquids in frustrated magnets. *Nature*, 464(7286):199–208, Mar 2010.

[207] Jia-Xin Yin, Songtian S. Zhang, Guoqing Chang, Qi Wang, Stepan S. Tsirkin, Zurab Guguchia, Biao Lian, Huibin Zhou, Kun Jiang, Ilya Belopolski, Nana Shumiya, Daniel Multer, Maksim Litskevich, Tyler A. Cochran, Hsin Lin, Ziqiang Wang, Titus Neupert, Shuang Jia, Hechang Lei, and M. Zahid Hasan. Negative flat band magnetism in a spin–orbit-coupled correlated kagome magnet. *Nature Physics*, 15(5):443–448, May 2019.

[208] Qi Wang, Shanshan Sun, Xiao Zhang, Fei Pang, and Hechang Lei. Anomalous hall effect in a ferromagnetic fe_3sn_2 single crystal with a geometrically frustrated fe bilayer kagome lattice. *Phys. Rev. B*, 94:075135, Aug 2016.

[209] Zhiyong Lin, Jin-Ho Choi, Qiang Zhang, Wei Qin, Seho Yi, Pengdong Wang, Lin Li, Yifan Wang, Hui Zhang, Zhe Sun, Laiming Wei, Shengbai Zhang, Tengfei Guo, Qingyou Lu, Jun-Hyung Cho, Changgan Zeng, and Zhenyu Zhang. Flatbands and emergent ferromagnetic ordering in fe_3sn_2 kagome lattices. *Phys. Rev. Lett.*, 121:096401, Aug 2018.

[210] Jia-Xin Yin, Songtian S. Zhang, Hang Li, Kun Jiang, Guoqing Chang, Bingjing Zhang, Biao Lian, Cheng Xiang, Ilya Belopolski, Hao Zheng, Tyler A. Cochran, Su-Yang Xu, Guang Bian, Kai Liu, Tay-Rong Chang, Hsin Lin, Zhong-Yi Lu, Ziqiang Wang, Shuang Jia, Wenhong Wang, and M. Zahid Hasan. Giant and anisotropic many-body spin–orbit tunability in a strongly correlated kagome magnet. *Nature*, 562(7725):91–95, Oct 2018.

[211] Linda Ye, Mun K. Chan, Ross D. McDonald, David Graf, Mingu Kang, Junwei Liu, Takehito Suzuki, Riccardo Comin, Liang Fu, and Joseph G. Checkelsky. de Haas-van Alphen effect of correlated Dirac states in kagome metal Fe3Sn2. *Nature Communications*, 10(1):4870, Oct 2019.

[212] Zhiyong Lin, Chongze Wang, Pengdong Wang, Seho Yi, Lin Li, Qiang Zhang, Yifan Wang, Zhongyi Wang, Hao Huang, Yan Sun, Yaobo Huang, Dawei Shen, Donglai Feng, Zhe Sun, Jun-Hyung Cho, Changgan Zeng, and Zhenyu Zhang. Dirac fermions in antiferromagnetic FeSn kagome lattices with combined space inversion and time-reversal symmetry. *Phys. Rev. B*, 102:155103, Oct 2020.

[213] Yaofeng Xie, Lebing Chen, Tong Chen, Qi Wang, Qiangwei Yin, J. Ross Stewart, Matthew B. Stone, Luke L. Daemen, Erxi Feng, Huibo Cao, Hechang Lei, Zhiping Yin, Allan H. MacDonald, and Pengcheng Dai. Spin excitations in metallic kagome lattice FeSn and CoSn. *Communications Physics*, 4(1):240, Nov 2021.

[214] L A Fenner, A A Dee, and A S Wills. Non-collinearity and spin frustration in the itinerant kagome ferromagnet Fe3Sn2. *Journal of Physics: Condensed Matter*, 21(45):452202, oct 2009.

[215] Hisao Yamamoto. Mössbauer Effect Measurement of Intermetallic Compounds in Iron-Tin System : Fe5Sn3 and FeSn. *Journal of the Physical Society of Japan*, 21(6):1058–1062, 1966.

[216] Hubertus Giefers and Malcolm Nicol. High pressure X-ray diffraction study of all Fe–Sn intermetallic compounds and one Fe–Sn solid solution. *Journal of Alloys and Compounds*, 422(1):132–144, 2006.

[217] Shiang Fang, Linda Ye, Madhav Prasad Ghimire, Mingu Kang, Junwei Liu, Minyong Han, Liang Fu, Manuel Richter, Jeroen van den Brink, Efthimios Kaxiras, Riccardo Comin, and Joseph G. Checkelsky. Ferromagnetic helical nodal line and kane-mele spin-orbit coupling in kagome metal fe_3sn_2. *Phys. Rev. B*, 105:035107, Jan 2022.

[218] Hisashi Inoue, Minyong Han, Linda Ye, Takehito Suzuki, and Joseph G. Checkelsky. Molecular beam epitaxy growth of antiferromagnetic Kagome metal FeSn. *Applied Physics Letters*, 115(7):072403, 2019.

[219] Deshun Hong, Changjiang Liu, Haw-Wen Hsiao, Dafei Jin, John E. Pearson, Jian-Min Zuo, and Anand Bhattacharya. Molecular beam epitaxy of the magnetic Kagome metal FeSn on LaAlO3 (111). *AIP Advances*, 10(10):105017, 2020.

[220] Durga Khadka, T. R. Thapaliya, Jiajia Wen, Ryan F. Need, and S. X. Huang. High quality epitaxial thin films and exchange bias of antiferromagnetic dirac semimetal fesn. *Applied Physics Letters*, 117(3):032403, 2020.

[221] Xiang Zhang, Guojun Ma, Mengke Liu, and Zhi Li. Removal of residual element tin in the ferrous metallurgy process: A review. *Metals*, 9(8), 2019.

[222] Brian C. Sales, Jiaqiang Yan, William R. Meier, Andrew D. Christianson, Satoshi Okamoto, and Michael A. McGuire. Electronic, magnetic, and thermodynamic properties of the kagome layer compound FeSn. *Phys. Rev. Materials*, 3:114203, Nov 2019.

[223] Durga Khadka, T. R. Thapaliya, Sebastian Hurtado Parra, Jiajia Wen, Ryan Need, James M. Kikkawa, and S. X. Huang. Anomalous Hall and Nernst effects in epitaxial films of topological kagome magnet Fe_3Sn_2. *Phys. Rev. Materials*, 4:084203, Aug 2020.

[224] Hong Li, He Zhao, Kun Jiang, Qi Wang, Qiangwei Yin, Ning-Ning Zhao, Kai Liu, Ziqiang Wang, Hechang Lei, and Ilija Zeljkovic. Manipulation of dirac band curvature and momentum-dependent g factor in a kagome magnet. *Nature Physics*, Mar 2022.

[225] Guohong Li and Eva Y. Andrei. Observation of landau levels of dirac fermions in graphite. *Nature Physics*, 3(9):623–627, Sep 2007.

[226] T. Hanaguri, K. Igarashi, M. Kawamura, H. Takagi, and T. Sasagawa. Momentum-resolved landau-level spectroscopy of dirac surface state in bi_2se_3. *Phys. Rev. B*, 82:081305, Aug 2010.

[227] Ilija Zeljkovic, Yoshinori Okada, Maksym Serbyn, R. Sankar, Daniel Walkup, Wenwen Zhou, Junwei Liu, Guoqing Chang, Yung Jui Wang, M. Zahid Hasan, Fangcheng Chou, Hsin Lin, Arun Bansil, Liang Fu, and Vidya Madhavan. Dirac mass generation from crystal symmetry breaking on the surfaces of topological crystalline insulators. *Nature Materials*, 14(3):318–324, Mar 2015.

[228] Lin Jiao, Qiunan Xu, Yeryun Cheon, Yan Sun, Claudia Felser, Enke Liu, and Steffen Wirth. Signatures for half-metallicity and nontrivial surface states in the kagome lattice Weyl semimetal $Co_3Sn_2S_2$. *Phys. Rev. B*, 99:245158, Jun 2019.

[229] Qian-Qian Yuan, Liqin Zhou, Zhi-Cheng Rao, Shangjie Tian, Wei-Min Zhao, Cheng-Long Xue, Yixuan Liu, Tiantian Zhang, Cen-Yao Tang, Zhi-Qiang Shi, Zhen-Yu Jia, Hongming Weng, Hong Ding, Yu-Jie Sun, Hechang Lei, and Shao-Chun Li. Quasiparticle interference evidence of the topological Fermi arc states in chiral fermionic semimetal CoSi. *Science Advances*, 5(12):eaaw9485, 2019.

[230] Madhav Prasad Ghimire, Jorge I. Facio, Jhih-Shih You, Linda Ye, Joseph G. Checkelsky, Shiang Fang, Efthimios Kaxiras, Manuel Richter, and Jeroen van den Brink. Creating weyl nodes and controlling their energy by magnetization rotation. *Phys. Rev. Research*, 1:032044, Dec 2019.

[231] M. Yao, H. Lee, N. Xu, Y. Wang, J. Ma, O. V. Yazyev, Y. Xiong, M. Shi, G. Aeppli, and Y. Soh. Switchable Weyl nodes in topological Kagome ferromagnet Fe3Sn2, 2018.